分类号_____ 密级_____

UDC _____ 编号_____

华中师范大学

博士学位论文

ALICE 实验中非直接 D^0 介子在重离子对撞中的产率测量

学位申请人姓名: 蔡孟珂

申请学位学生类别: 博 士

申请学位学科专业: 物理学

指导教师姓名: 周代翠 张晓明

Andrea Dainese Andrea Rossi

博士学位论文

ALICE 实验中非直接 D^0 介子在重离子对撞中的产率测量

论文作者： 蔡孟珂

指导教师： 周代翠 教授

张晓明 副教授

Andrea Dainese 资深研究员

Andrea Rossi 副教授

学科专业： 物理学

研究方向： 粒子物理与原子核物理

华中师范大学物理学院（系）

2023年3月

Dissertation

Non-prompt D^0 production in heavy-ion collisions with ALICE

By

Mengke Cai

Supervisor: Prof. Daicui Zhou

Assoc. Prof. Xiaoming Zhang

Dr. Andrea Dainese

Dr. Andrea Rossi

Specialty: Physics

Research Area: Particle Physics and Nuclear Physics

Institute of Particle Physics

Central China Normal University

March 2023

华中师范大学学位论文原创性声明和使用授权说明

原创性声明

本人郑重声明：所呈交的学位论文，是本人在导师指导下，独立进行研究工作所取得的研究成果。除文中已经标明引用的内容外，本论文不包含任何其他个人或集体已经发表或撰写过的研究成果。对本文的研究做出贡献的个人和集体，均已在文中以明确方式标明。本声明的法律结果由本人承担。

作者签名：蔡玉婷　　日期：2023年 6 月 1 日

学位论文版权使用授权书

学位论文作者完全了解华中师范大学有关保留、使用学位论文的规定，即：研究生在校攻读学位期间论文工作的知识产权单位属华中师范大学。学校有权保留并向国家有关部门或机构送交论文的复印件和电子版，允许学位论文被查阅和借阅；学校可以公布学位论文的全部或部分内容，可以允许采用影印、缩印或其它复制手段保存、汇编学位论文。（保密的学位论文在解密后遵守此规定）

保密论文严格按照《华中师范大学涉密研究生与涉密学位论文管理办法》进行管理。非保密论文不属于保密范围，适用本授权书。

因特殊情况需延期发布的论文，同意论文提交后延期□半年；□一年；□二年发布。到期后适用本授权书。

作者签名：蔡玉婷　　导师签名：

日期：2023年 6 月 1 日　　日期：2023年 6 月 1 日

摘要

夸克–胶子–等离子体（QGP）是一种极端高温、高能量密度下由呈现出渐进自由性质的夸克与胶子形成的新物质相。针对这种由标准模型中量子色动力学预言存在的物质形态，对其性质和相变过程的研究在检验和发展量子色动力学中有重要意义。在实验室环境下，可由高能重离子对撞实验产生并定量研究这种新物质形态的产生及演化性质。建在瑞士–法国交界处的欧洲核子中心（CERN）的大型强子对撞机（LHC），其产生的实验数据为研究QGP中发生的譬如喷注淬火、集体运动等现象创造了独特条件。其中喷注淬火现象是指高动量部分子在穿越QGP时与其发生相互作用，通过弹性过程以及非弹性碰撞产生胶子辐射两类过程将能量传递给QGP介质。而集体运动是指QGP内解禁闭的组分部分子在内部压力梯度的作用下表现出集体性的运动模式，通常表现为各向同性的向外扩张或者呈现各向异性的模式。对于这些现象，采用重味夸克探针能够高效准确的进行探测和分析。重夸克通常产生于高能质子–质子（pp）和核–核碰撞初始的硬散射过程，相比QGP其形成得更早，因此能够在时空中完整经历QGP的演化过程。

本论文将介绍ALICE实验中对于非直接D^0介子在pp以及铅核–铅核（Pb–Pb）碰撞系统中，碰撞质心能量均为5.02 TeV下的产率测量。非直接D^0介子是底夸克强子的衰变产物，因而能够提供底夸克相关的信息。通过对pp对撞实验中的产率进行测量，所得测量结果对于检验微扰量子色动力学（pQCD）的预言提供了重要的实验依据，同时此测量数据能够为Pb–Pb对撞实验中的测量提供参考值。在Pb–Pb实验中非直接D^0的测量则能够研究底夸克与介质的相互作用。其中在高横动量区间，底夸克（bottom: b）–介质间的能量交换起到主导作用。通过与粲夸克（charm: c）强子化产生的直接D介子以及轻夸克粒子进行对比分析，能够研究该过程中部分子能量损失的质量依赖性以及色依赖性。另一方面在低横动量区间，系统的集体性运动占主导地位。此时可对b夸克在参与系统集体运动的过程以及该过程中的散射进行研究。由于QGP的温度远小于b夸克产生所需的条件，其在QGP中的产生概率可忽略，因此对pp系统和重离子对撞系统中总产生截面的差异主要体现为初态冷核效应对部分子分布函数的核修正（nPDF），而b夸克较大的质量则对小Bjorken–x区间的nPDF更加敏感。由于nPDF不满足pQCD的微扰条

件，其通常无法以第一性原理通过pQCD进行计算获得。因此通过实验测量的pp系统和重离子对撞系统中总产生截面的对比，将有助于对小Bjorken–x区间的nPDF进行限定，提升重离子对撞实验中QGP产生的初始条件的认识，同时还能对核结构和光–核反应等领域的研究提供重要帮助。

对非直接D^0在pp对撞实验中的测量，其主要的物理量是中心快度区间（$|y| < 0.5$）的微分产生截面。该研究首先对D^0的衰变进行重建，其主要用到了强子衰变道$D^0 \to K^-\pi^+$。重建得到的信号经过了基于衰变拓扑学变量分布的筛选以提高信号–背景比与非直接D^0在信号中的占比。我们在ALICE实验中首次基于机器学习中的增强决策树（BDT）进行了该筛选，通过使用蒙特–卡洛（Monte-Carlo）方法产生的模拟数据对BDT进行训练。训练所得的两组BDT模型分别能够减少重建信号中的组合背景，以及增强信号中的非直接占比。筛选后的信号将通过不变质量分析，提取出信号净值。同时，本实验中首次采用并改进了基于数据的最小χ^2方法来提取信号中的非直接占比，该占比由约20%首次提高至最高约90%，显著提高了测量精度。最终所测量得到的p_{T}–微分产生截面涵盖了$1 < p_{\mathrm{T}} < 24$ GeV/c的横动量区间。通过外延的方法，本论文同时计算了全横动量区间下的积分产生截面。测量所得的结果同时与不同的pQCD模型进行了对比，发现实验数据与FONLL的预测结果符合得较好，预测的中心值和测量值在误差允许范围内相吻合；另外GM–VFNS模型的预测值相比测量值偏低。另外，本课题对$b\bar{b}$总产生截面进行了计算，最终采用了通过非直接D^0、D^+、D_s^+计算的平均值。该计算结果与此前在双电子对撞实验中测量的结果相符合，同时与pQCD计算模型比如FONLL，NNLO所预测的结果相符合。这些结论验证了pQCD在TeV能量区间中b夸克的微分产生截面计算的有效性，同时这些测量结果为重离子碰撞实验中b夸克在QGP中的输运现象研究提供了参考基准。

重夸克与QGP组分相互作用可通过重离子对撞实验中D介子的核修正因子（R_{AA}）的测量进行研究。本论文工作首次对非直接D^0在Pb–Pb对撞中的R_{AA}在不同碰撞中心度类别（0–10%和30–50%）分别进行了测量，并且包括了低横动量区间（$1 < p_{\mathrm{T}} < 2$ GeV/c）。中心碰撞中（对应中心度0–10%），测量所得R_{AA}在中等横动量区（$5 < p_{\mathrm{T}} < 8$ GeV/c）的压低系数在3左右。在低横动量区间，R_{AA}随横动量减小而增加，直到约等于1（对应$1 < p_{\mathrm{T}} < 3$ GeV/c）。另外，本工作对非直接D^0的R_{AA}与直接D^0 R_{AA}的比

值进行了分析研究。对于中心碰撞（0–10%）的中等横动量区间，该比值明显大于1。测量结果与不同的模型预测进行了对比，这些模型在计算b夸克与介质相互作用时的能量损失时同时包含了弹性过程和非弹性过程，以及夸克重组的强子化机制。通过与模型的对比分析可发现，弹性过程导致的夸克能量损失在中、低横动量区间有显著占比，而非弹性过程导致的胶子辐射产生的能量损失在高横动量区间占主导地位；不同夸克组合对b夸克的强子过程具有影响，这意味着不仅是c夸克，质量更重的b夸克也存在热化自由度。这些结论有助于提升重夸克在夸克物质中输运性质的认识，同时也有助于完善检验夸克物质中的能量损失的质量依赖性—QCD中的重要基础特性之一。

本论文的主要结构如下：第一章对量子色动力学和重离子碰撞进行简介，引入夸克–胶子等离子体的性质以及重夸克探针；第二章是对ALICE实验的装置和性能进行简介；第三至五章分别介绍本论文涉及课题所需的方法、实验分析与测量结果，以及对所得结果的物理讨论；最后给出总结和展望。

关键词：大型强子对撞机（LHC）；大型重离子对撞实验（ALICE）；质子–质子（pp）对撞；铅核–铅核（Pb–Pb）对撞；非直接D介子；重夸克；核修正因子（R_{AA}）；夸克–胶子等离子体（QGP）；增强决策树（BDT）。

Abstract

The Quark–Gluon Plasma (QGP) is a new matter state composited by deconfined quarks and gluons which exist at extremely high temperature and energy density. This formation of matter, predicted by Quantum Chromodynamics (QCD) in the Standard Model, shows great importance as a phenomenon to test QCD theories with its phase transitions, where the properties of matter can be investigated in ultra–relativistic heavy–ion collision experiments. At the Large Hadron Collider (LHC), the produced experiments data of heavy ion collisions create possibility for QGP researches, with phenomena such as jet quenching, where high transverse momentum partons undergo energy loss interacting with de–confined medium via elastic processes or induced gluon radiations, and collective motions, where the expansion of bulk matter exhibits different patterns such as isotropic and anisotropic components which are physically driven by pressure gradients. Heavy quarks, are powerful probes of QGP due to their shorter formation timescale, and they are to mostly go through the full evolution of the collision system in space–time.

In this thesis, the measurements of non–prompt D^0 production in pp collisions at $\sqrt{s} = 5.02$ TeV and in Pb–Pb collisions at $\sqrt{s_{\mathrm{NN}}} = 5.02$ TeV with ALICE detectors are reported. The measurements of non–prompt D^0, which are produced in beauty–hadron decays, can provide valuable information in beauty sector. The measurement of production in pp collisions is important to test perturbative QCD calculations, and provide a reference for Pb–Pb collisions. While in latter, the non–prompt D^0 measurement can help to study the microscopic beauty–medium interactions. At high p_{T}, it allows to investigate the colour charge and mass dependence of in–medium energy loss. At low p_{T}, the participation of system collective expansion and diffusion process for beauty quarks can be investigated.

In pp collisions, the p_{T}–differential production cross section of non–prompt D^0 is measured at midrapidity ($|y| < 0.5$). The D^0 meson candidates are reconstructed via the hadronic decay channel $\mathrm{D}^0 \to \mathrm{K}^-\pi^+$. Then specific selections

based on Boosted Decision Trees (BDT), a machine learning model trained with pseudo–data from Monte Carlo simulations and background sample in data, are applied to the candidates. The application of BDT reduces the combinatorial background, and also to enhance the non–prompt fraction of D^0 from around 30% to 90% in signals. Afterwards, the signals are extracted via the invariant–mass analysis, and the non–prompt fractions are estimated with a data–driven minimizing–χ^2 approach. The measured p_{T}–differential cross section is within the transverse momentum range $1 < p_{\mathrm{T}} < 24$ GeV/c. With an extrapolating method, the p_{T}–integrated cross section is estimated at high precision. The results are well described by perturbative QCD (pQCD) calculations. The results are in good agreement with central prediction with FONLL calculated beauty hadron cross section and PYTHIA8 decay kinematics, while another prediction with GM–VFNS with two different transition approaches from beauty to non–prompt meson underestimated the measurement. Moreover, the total $\mathrm{b\bar{b}}$ production cross section is also determined from the measurements together with non–prompt D^0, D^+, and D_s^+ mesons, which is compatible with previous measurements of di–electron production at the same centre–of–mass energy as well as the cross section predicted by pQCD calculations such as FONLL and NNLO. The measured production in pp collisions also provide a reference for the same measurement in heavy–ion collisions.

While in Pb–Pb collisions, a similar measurement is performed at same per–nucleon–pair centre–of–mass energy. The nuclear modification factor (R_{AA}) of non–prompt D^0 was measured for the first time down to $p_{\mathrm{T}} = 1$ GeV/c in 0–10% and 30–50% centrality classes. A suppression in R_{AA} of factor about 3(2) is observed for $p_{\mathrm{T}} > 5$ GeV/c in 0–10%(30–50%) centrality, while at lower p_{T}, R_{AA} increases with decreasing p_{T}, and compatible with unity in $1 < p_{\mathrm{T}} < 3$ GeV/c. The data are described by models that include both collisional and radiative processes in calculating beauty–quark energy loss in QGP, and quark recombination in addition to fragmentation as hadronization mechanism. The R_{AA} ratios of non–prompt to prompt D^0–meson are reported significantly larger than unity at intermediate p_{T} in 0–10% centrality, as pre-

dicted by transportation models in which the energy loss for beauty quarks are less than charm quarks due to their larger mass.

Keywords: Large Hadron Collider (LHC), A Large Ion Collider Experiment (ALICE), pp collisions, Pb–Pb collisions, non–prompt D mesons, heavy quark production, nuclear modification factor (R_{AA}), Quark–Gluon Plasma (QGP), Boosted Decision Trees (BDT).

Contents

List of Figures

List of Tables

Chapter 1

Introduction

1.1 QCD theory and strong interaction

1.1.1 Standard Model

The Standard Model is one of the most successful theories developed in the 70s of twenty century, which brings remarkable understanding to the fundamental particles and interactions.

In Standard Model, everything in universe was found to be made from few basic building blocks – the fundamental particles. And the three out of four very fundamental interactions involved among the fundamental particles are introduced in a natural and self–consistent way. Since its development, Standard Model has successfully explained almost all experimental results and precisely predicted a wide variety of phenomena, and become a well–tested physics theory.

The fundamental interactions described by Standard Model, namely the electromagnetic, weak, and strong interactions, result from the exchange of force carrier particles among particles of matter. The latter group of matter particles occurs in two basic types called quarks and leptons, while the former force–carrier particles are bosons. In Standard Model, the gauge symmetry of $\mathrm{SU}(3) \otimes \mathrm{SU}(2) \otimes \mathrm{U}(1)$ group automatically leads to three basic interactions with their force carrier gauge bosons, and the multilets form of the matter particles. The electro–weak interaction involves all quarks and leptons in three

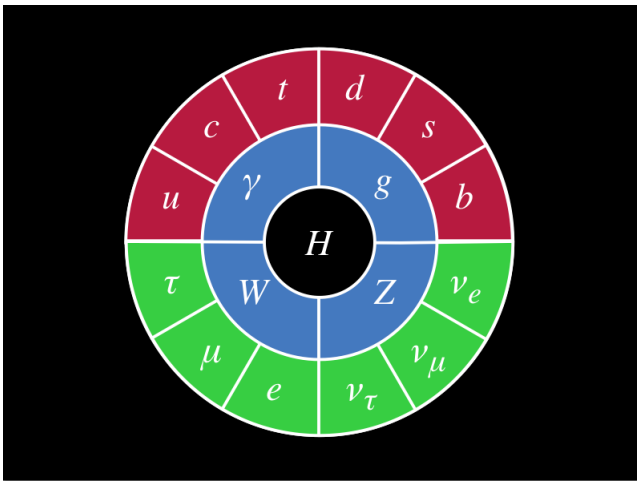

Figure 1.1: Fundamental elementary particles in the Standard Models, including quarks (red), leptons (green), gauge bosons (blue), and Higgs boson (black).

generations: $(\nu_{\mathrm{e}}, \mathrm{e}, \mathrm{u}, \mathrm{d})$, $(\nu_\mu, \mu, \mathrm{c}, \mathrm{s})$, and $(\nu_\tau, \tau, \mathrm{t}, \mathrm{b})$, with the gauge bosons of $\mathrm{SU}(2) \otimes \mathrm{U}(1)$: γ, W, and Z. Meanwhile, the strong interaction could be deduced from the gauge symmetry of non–Abelian SU(3) group that all 3 generations of quark were involved, along with the gauge boson g referred as "gluon" and leading to the Quantum Chromodynamics. The mass of all matter particles and gauge bosons were included in a spontaneous symmetry breaking mechanism, which introduces a type of scalar boson – Higgs boson for the interpretation of masses.

Even though the Standard Model is currently the best description of the subatomic world, there are still missing pieces of the puzzle. Only three of the four fundamental interactions were incorporated, where the most common interaction for everyday life – gravity, is unfitted to the whole picture. And what is beyond the Standard Model is also intriguing, such as the nature of dark matter and dark energy, the asymmetry between matter and anti–matter, the neutrino oscillations.

1.1.2 QCD and Quark gluon plasma

Quantum ChromoDynamics (QCD) is the gauge field theory that describe the strong interactions of quarks and gluons. As the quarks and leptons with electric charge interacts were described with Quantum Electrodynamics (QED), which is a part of the SU(2) $\otimes$ U(1) gauge symmetry, the symmetry of SU(3) gauge group demonstrates a similar way of interaction for the strong force. The Lagrangian density for the quarks and gluons is written in:

$$\mathcal{L} = \bar{q}_i(i\gamma^\mu D_\mu - m_q)q_i - \frac{1}{4}F^A_{\mu\nu}F^{A\mu\nu} \tag{1.1}$$

The six flavours of quark q_i are summed, with their mass m_q respectively. With SU(3) gauge–invariance, the covariant derivative is applied $D_\mu = \partial_\mu - ig_3\frac{\lambda^\alpha}{2}G^\alpha_\mu$ and the interacting field G^α_μ is the gluon fields mentioned before. They are combined in product with the Gell–Mann matrices λ_α to form the generator matrices of SU(3) group, where an independent coupling constant g_3 is extracted. The latter term contains the gluon field tensors $F^A_{\mu\nu} = \partial_\mu G^A_\nu - \partial_\nu G^A_\mu - g_3 f_{ABC}G^B_\mu G^C_\nu$, in which f_{ABC} come from the commutation of λ_α: $[\lambda_\alpha, \lambda_\beta] = 2if_{ABC}\lambda_C$.

$$q = \left(q^r, q^g, q^b\right)^T \tag{1.2}$$

The quarks in this representation are triplets as in Eq. 1.2. As electrons, for example, carry the electric charge in Quantum Electrodynamics, quarks carry the "colour" charge of the strong interaction. The index r, g, b refer to colour of red, green, and blue, as three basic colours in natural light. While for gluon fields G^α_μ, they presented as colour octuplet ($\alpha = 1, 2, ..., 8$) in strong interaction. And the presented coupling terms in $F^A_{\mu\nu}$ indicate that the possibility for gluons to interacts directly with themselves, which leads to quite different properties from the situation with QED only.

Considering the colour potential of a static quark–antiquark pair:

$$V(r) = -\frac{3}{4}\frac{\alpha_s}{r} + \kappa r \tag{1.3}$$

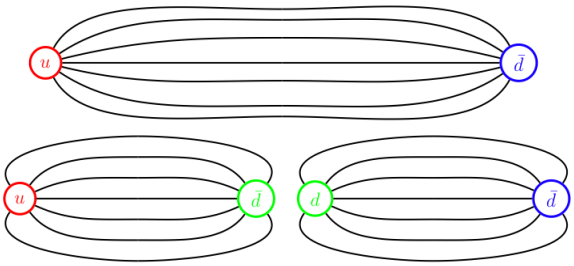

Figure 1.2: Left: Bounded quark–antiquark pair, with strong interaction field lines in the flux tubes where gluon exchanges is responsible for the binding. Right: By pulling apart the quarks, the energy increases until the flux tubes break up in a new quark–antiquark pair.

which consists a Coulomb–like term and linear term increases with the distance r. The colour field is illustrated as the flux tube between quark and antiquark, which stretches as the distance r increases but the density remain constant, since the colour charge do not change in the stretching process. As the field energy grows, the supplied energy goes into a new quark–antiquark pair and the colour field flux tubes breaks up then connects to the new quarks at each end. It would take infinity energy to separate off a quark or antiquark which carries net colour charge, as if they are confined in the colour–singlet state. This confinement implies that coloured particles (quarks and gluons) appears as jets, in which the large fraction of energy transferred from the collisions dissipates and create pairs of physical mesons ($q\bar{q}'$ pairs) that energetically favorable fragments into mesons.

Another difference from the QED is in the coupling constants. In field theory of QED, the coupling strength α is corrected considering the high–order loop terms, which suggested that the dependence of transferred momentum Q^2 for coupling strength[1], with the assumption $Q^2 \gg M^2$:

$$\alpha(Q^2) = \frac{\alpha(\mu^2)}{1 + \frac{\alpha(\mu^2)}{3\pi}\beta \ln(\frac{\mu^2}{Q^2})} \tag{1.4}$$

where the constant β is determined by the types of particles may participate the loop. e.g. $\beta = n_l + 3(\frac{2}{3})^2 n_{2/3} + 3(\frac{1}{3})^2 n_{-1/3}$, in which n_l, $n_{2/3}$, $n_{-1/3}$

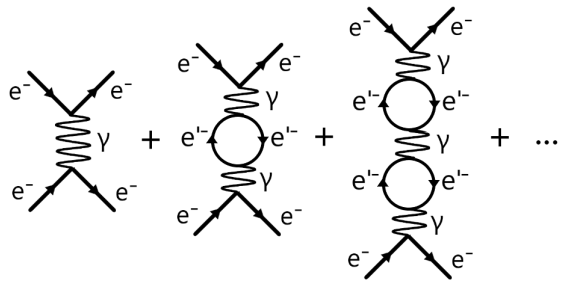

Figure 1.3: Running coupling constant perturbative loops

are the possible number of leptons, +2/3 charged quarks, and -1/3 charged quarks, and the constant three stands for the colour charge. The term "running" coupling referred in Eq.[1.4], since the strength of electric interaction is under the effect of the energy scale. The measured coupling strength constant at $q^2 = \mu^2$ is applied for the prediction of coupling strength at any energy. The understanding for the running coupling in QED could start from the virtual charged particles in the perturbative loops, where the polarized $f\bar{f}$ pair create a screening effect to reduce the effective strength. With higher energy scale, the screening becomes weaker thus a stronger coupling is observed.

Meanwhile in QCD, a similar effect was found but with significantly new features. The virtual gluons are also possible candidates to enter the perturbative loop apart from colour charged quarks, because gluon interact with themselves. In QCD, the coupling strength has similar running form as in Eq.[1.4], which is:

$$\alpha_s(Q^2) = \frac{\alpha_s(\mu^2)}{1 - \frac{\alpha_s(\mu^2)}{12\pi}\beta_s \ln(\frac{\mu^2}{Q^2})} \tag{1.5}$$

where the constant $\beta_s = 33 - 2 \cdot n_f$, and n_f is the number of possible flavour of quarks. As only six flavours of quarks were found so far, the constant β_s is always positive, which leads a different trend from QED. The QCD coupling strength become weaker with higher energy scale due to the anti–screening

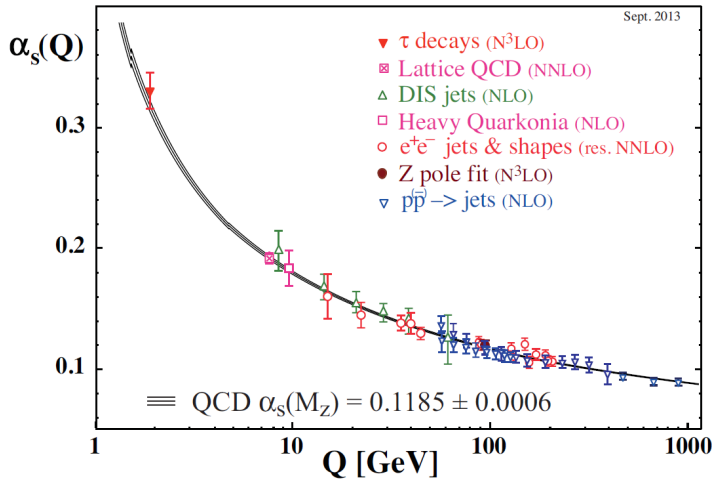

Figure 1.4: Measurements of strong interaction constant as a function of energy scale Q until september 2013. The degree of perturbation for QCD theory used in the α_s is indicated in brackets[7].

effect of colour charge. As the Q^2 gets larger, the possibility for gluon radiation gets larger, and the original quark becomes more like free particle, which is referred as "asymptotic freedom" discovered in the last century[2]–[6].

At the other end, for small Q^2 the denominator of Eq. 1.5 can vanish which will lead to divergence for the coupling strength α_s. With $\alpha_s(\mu^2 = M_{Z^0}^2) = 0.12$, α_s exceeds unity for $Q^2 \leq \mathcal{O}(0.1 - 1\ \mathrm{GeV}/c)$, where the assumption for perturbative expansions start to fail, and the confinement of strong interaction takes over.

In some experimental conditions such as ultra–relativistic heavy ion collisions, the momentum transfer is large enough for partons (quarks and gluons) to show significant asymptotic freedom. The quarks behave like free particles at short distances, due to the screening effect by the free colour charges. It anticipates that with the increasing energy scale, the QCD matter at high energy densities undergoes a phase transition from a state with confined hadrons into a new state of matter with deconfined quarks and gluons, the Quark–Gluon Plasma (QGP)[8]–[17].

An illustration of the QCD matter phase diagram is shown in Fig. [1.5],

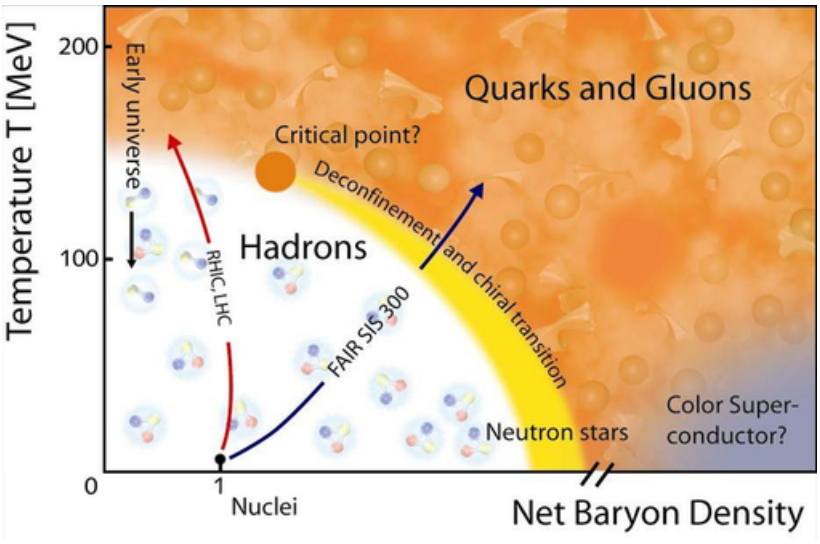

Figure 1.5: An illustration of QCD phase diagram as a function of temperature and net baryon density ρ_B.

which is based on thermodynamical consideration and lattice QCD calculations. The phase transition of strong–interaction matter is drawn with the temperature T and the baryonic chemical potential μ_B, in which the latter is defined as the energy needed to increase one baryon ($\mu_B = \partial E/\partial N_B$). The interpretation to the phase structure of QCD is in Fig. [1.5], in different areas. At low temperature and for $\mu_B \sim 1$ GeV/c, the QCD matter is confined in its standard form as in atomic nuclei. Increasing the energy density of the system, as the temperature or the baryon–chemical potential increase, a hadronic gas phase is reached. If the energy density is further increased, it transform into a deconfined QGP phase where the partons are still interacting but not confined within hadrons anymore. This transition to the QGP is predicted by lattice QCD calculations to occur at a critical temperature $T_c \sim 155$ MeV for 3 flavours ($T_c \sim 170$ MeV for 2 flavours), corresponding to an energy density $\epsilon_c \sim 1$ GeV/fm^3. If μ_B is large enough ($\mu_B \gg 1$ GeV/c), the ground state of QCD matter at low temperature will form Cooper pairs leading to colour superconductivity[18].

The nature of the QCD phase transition such as its order and the critical

behaviour are controlled by the global symmetry, which only exist in the limits of either infinite or vanishing quark masses. For any non–zero, finite value of quark masses the global symmetries are explicitly broken. In the limit of infinite–heavy quarks, the free energy of heavy quark $F_{q\bar{q}}$ provides a unique distinction between confinement and deconfinement below or above the critical temperature T_c. In lattice QCD, The free energy of heavy quark can be calculated from the expectation value of the Polyakov loop correlation function $|\langle L\rangle|^2$[19], which is an order parameter under the large separation assumption:

$$|\langle L\rangle|^2 \propto \exp\left(-\frac{F_{q\bar{q}}}{T}\right) \tag{1.6}$$

$$\langle L\rangle \quad \begin{cases} = 0 & \Leftrightarrow \quad \text{confined phase}, \quad T < T_c \\ > 0 & \Leftrightarrow \quad \text{deconfined phase}, \quad T > T_c \end{cases} \tag{1.7}$$

where the phase transition is suggested to be of the first order. While in the vanishing mass limit, the QCD Lagrangian is invariant under chiral transformations. For n_f massless quark flavours, the gauge symmetry of $\mathrm{U(1)}\times \mathrm{SU_L}(n_f) \times \mathrm{SU_R}(n_f)$ is only partially envolved with spontaneous symmetry breaking in vacuum for $\mathrm{SU}(n_f)$ part, which give rise to $(n_f^2 - 1)$ Goldstone particles, the pions. The chiral condensate in this phase shows as:

$$\langle \bar{q}q\rangle = \langle \bar{q}_R q_L + \bar{q}_L q_R\rangle \tag{1.8}$$

$$\langle \bar{q}q\rangle \quad \begin{cases} > 0 & \Leftrightarrow \quad \text{symmetry broken phase}, \quad T < T_c \\ = 0 & \Leftrightarrow \quad \text{symmetric phase}, \quad T > T_c \end{cases} \tag{1.9}$$

where colour and flavour indices are to be summed. In the limit of vanishing quark masses the condensate stays non–zero as long as the chrial symmetry is spontaneously broken. While at the critical boundary, a sudden change in the long distance behaviours of the heavy–quark potential or the chiral condensate as a function of coupling strength can be observed through the susceptibilities: the Polyakov loop suspectibility χ_L and the chiral suspectibility χ_m, which is shown in Fig. 1.6. The region of most rapid changes for $\langle L\rangle$ and

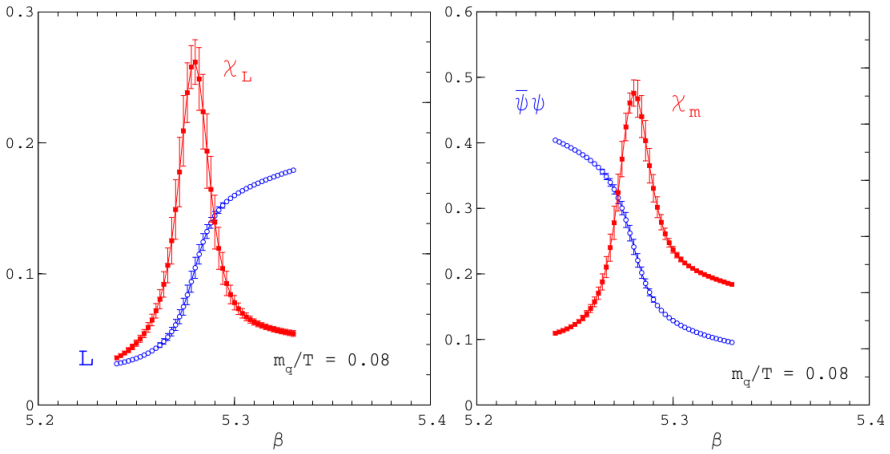

Figure 1.6: Deconfinement and chiral symmetry restoration in 2–flavour QCD. Left: the order parameter of deconfinement $\langle L \rangle$ in the limit of $m_q \to \infty$, and its susceptibility. Right: the order parameter for chiral symmetry breaking $\overline{\psi}\psi$ in the chiral limit ($m_q \to \infty$) and its susceptibility. The horizontal axis represents the coupling $\beta = 6/g^2$[19].

$\langle q\bar{q} \rangle$ coincide, which indicates the fact that the restoration of chiral symmetry and the deconfinement occur at the same condition.

The other effect due to the deconfinement in QCD is the increasing number of degrees of freedom which get liberated at the phase transition temperature. At low temperature ($T < T_c$), the quarks and gluons are confined in colour singlet hadrons which do not contribute to the thermodynamics. Due to the asymptotic freedom, the QCD energy density and pressure will become alike as ideal gas at infinite temperature. Assuming for massless partons in this state, the equation of state is:

$$p = \frac{\pi^2}{90} n_{\rm dof} T^4 \tag{1.10}$$

where $\epsilon = 3p$, and n_{dof} is the number of degrees of freedom. In Fig. 1.7, the sudden increase of ϵ/T^4 near the critical temperature T_c can be interpreted as due to the change of $n_{\rm dof}$ from 3 in the pion gas phase to the deconfined phase with additional degrees of freedom from the free colour charges and quark flavours.

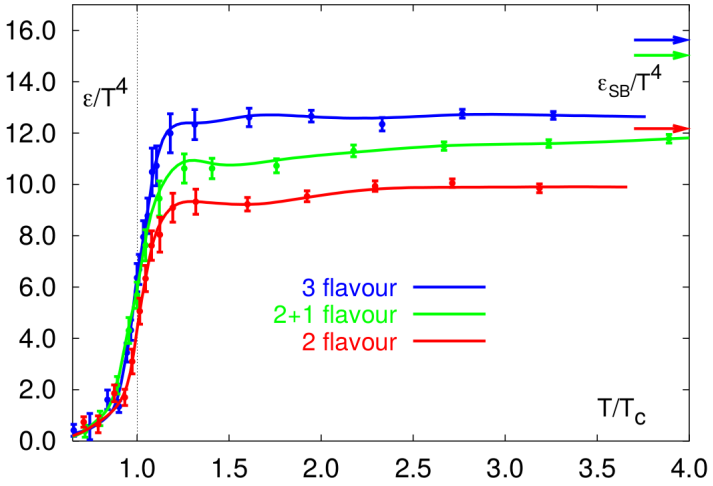

Figure 1.7: The energy density ϵ/T^4 in lattice QCD with different number of degrees of freedom as a function of temperature[20].

1.2 Heavy ion collisions

As discussed in the last section, the phase transition from hadronic gas to the QGP happens at extremely high temperature and energy density, which is expected to exist in the environments such as the primordial universe few microseconds after the Big Bang[21]. In laboratory, such extreme condition can be reached in ultra–relativistic heavy–ion collisions, where the energy density reaches far above that of normal nuclear matter and the transition to QGP becomes possible for investigation on their properties. Over past decades from twenty century, many accelerator and collider experiments conducted at varies of center–of–mass energies have brought valuable experiences. The Alternating Gradient Synchrotron (AGS, $\sqrt{s_{\rm NN}} = 4.6$ GeV), Super Proton Synchrotron (SPS, $\sqrt{s_{\rm NN}} = 17.2$ GeV), Relativistic Heavy–Ion Collider (RHIC, up to $\sqrt{s_{\rm NN}} = 200$ GeV), and Large Hadron Collider (LHC, up to $\sqrt{s_{\rm NN}} = 5.02$ TeV) produced high–quality experiment data which led to the discovery of the QGP.

The heavy–ion collisions are expected to cause the formation of "glasma", a dense and non–thermal QCD plasma with highly occupied gauge fields modes.

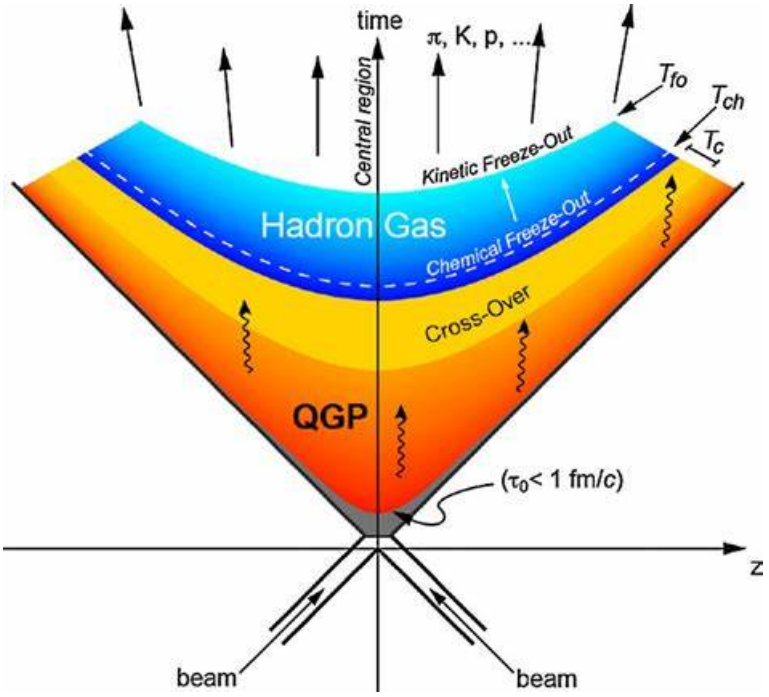

Figure 1.8: A schematic diagram of the space–time evolution of a ultra–relativistic heavy–ion collision.

Then the system thermalizes rapidly and evolves through a series of stages in space–time as illustrated in Fig. 1.8:

Initial stage : The two nuclei approach each other with the relativistic velocities in the laboratory frame, where they look like two "thin pancakes" due to the Lorentz contraction, as presented in Fig. 1.9. The collision of the nuclei is regarded as multiple nucleon–nucleon collisions happen at the same time.

Pre–equilibrium : High energy partons are produced in hard scattering process. They interacts with each other in the expanding hot QCD matter. The lasting time scale of this stage is at $\tau \sim 0.6 - 1\text{fm}/c$, and high transverse momentum particles (jets, heavy quarks, and photons) are generated at this stage.

QGP phase : The temperature of this stage is likely to exceed the critical boundary T_c, where the QCD matter become deconfined and thermalize nearly to form QGP. At this stage, the evolution can be described in terms of relativistic viscous hydrodynamics because of its small shear viscosity. Then the system expands and cools down rapidly.

Hadronisation : The temperature of medium drops below T_c, and the QGP phase–transform to hadron gas. A phase between QGP and hadron gas is expected to exist at this stage.

Freeze–out : At this stage, the hadrons are formed and their species are fixed. Elastic processes between produced hadrons and the medium are still possible for momentum transfer.

Different observables in the final state are sensitive to the various stages of system evolution created in heavy–ion collisions. The bulk of the emitted particles are soft (low momentum) hadrons, which decouple from the collision region in the late freeze–out stage. The research on the distributions of physics quantities for the final stage thus constrains the dynamic evolution

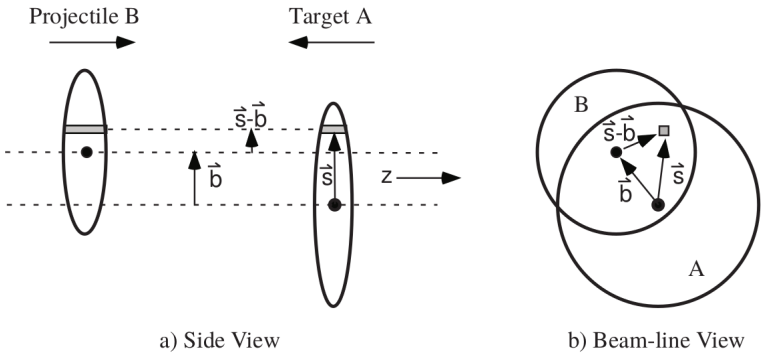

Figure 1.9: A schematic representation of two colliding nucleus in their longitudinal view (left) and in transverse view (right), with the optical Glauber model geometry[22].

and provides the indirect information about the early stage of the collision. Such as the freeze–out temperature, chemical potential, radial expansion velocity, hydrodynamical properties of the medium, size parameters. The study of jets originating from hard partons and heavy–flavour hadrons also provides insights into the interaction mechanism inside the QGP. Photons, on the other hand, do not interact with strong force thus they probe the state of the matter at the time of their production, as the thermal photons radiated off the quarks which undergo collisions with other quarks and gluons in the thermal medium can be used to measure the temperature of the medium.

The heavy–ion collisions at the LHC are one of the most important experiments conducted on site with currently the highest center–of–mass energy per nucleon pairs (up to $\sqrt{s_{\mathrm{NN}}} = 5.02$ TeV). In particular, the heavy–ion collision programme at the LHC has the aim for precise measurement of QGP parameters. The detail collision geometry and the global collision properties will be presented in the following sections, as well as an example of hard probe with heavy flavour particles.

1.2.1 Collision geometry

The geometry of the collision plays an important role in the study of nuclear matter effects and QGP formation, as the size of nuclei are un–negligible to the

scales of interest in high energy physics. In the center–of–mass frame, the two colliding nuclei are "squeezed" to pancake–shape with transverse diameter $2R_A \sim 2A^{1/3}$, as shown in Fig. 1.9. The directions of the momentum for each nucleon are parallel to the z–axis, while the most interesting area in the cross section is the almond–shape overlapped region. The quantities to define collision geometry are:

- The impact parameter b is defined as the distance between the centres of two colliding nuclei at the closest approach. It is a straightforwards since the area of overlapping depends only on the scale of the nuclei and the impact parameter b, and the centrality of the collision is defined with the b in percentiles, where a head–on collision corresponds to near 0% and a peripheral one corresponds to $\sim 100\%$.

- Two numbers are defined to characterize a collision, $N_{\rm part}$ and $N_{\rm coll}$. The first one $N_{\rm part}$ refers to the total number of participant nucleons within the colliding nuclei, where the participants undergo at least one inelastic collision. The latter one $N_{\rm coll}$ stands for the number of binary nucleon–nucleon collisions.

Instead of direct measurement, these quantities can be derived from a Glauber model[22], where the collision of two nuclei was viewed as individual interactions of the constituent nucleons. It was assumed that at sufficiently high energies, these nucleons will carry sufficient momentum so that the nuclei essentially pass through each other undeflected. The size of nucleus is also assumed to be large enough compared to the range of nucleon–nucleon force, and the nucleons move independently in the nucleus. Then the probability per unit transverse area of the nucleon being located in the flux tubes illustrated in Fig. 1.9 is $T_A(\boldsymbol{s})$ and $T_B(\boldsymbol{s}-\boldsymbol{b})$ respectively. The product of T_A and T_B then gives the probability for finding two nucleon located in two flux tubes which overlaps in cross sections in the projectile and the target. And the overall nuclear overlap function $T_{AB}(\boldsymbol{b})$ is defined as:

$$T_{AB}(b) = \int T_A(\boldsymbol{s}) T_B(\boldsymbol{s} - \boldsymbol{b}) \mathrm{d}^2 s \tag{1.11}$$

which depends on the magnitude of impact parameter b. The T_{AB} has the unit of inverse area, which can be interpreted as the effective overlap area for two nucleons each in A and B to interact. Then the probability of an interaction occurring is $T_{AB}(b) \cdot \sigma_{inel.}^{\mathrm{NN}}$, where only inelastic cross section for nucleon–nucleon is considered, and the energy loss due to the elastic processes is negligible. The probability of having n interactions between nucleus A and B is given by a binomial distribution:

$$P(n, b) = \mathcal{C}_{A \cdot B}^{n} [T_{AB}(b) \sigma_{inel.}^{\mathrm{NN}}]^n [1 - T_{AB}(b) \sigma_{inel.}^{\mathrm{NN}}]^{A \cdot B - n} \tag{1.12}$$

where $\mathcal{C}_{A \cdot B}^{n}$ is the combinations for finding n collisions out of $A \cdot B$ possible nucleon–nucleon interactions. Based on the probability distribution, the relevant geometry quantities of the collision can be determined as:

$$N_{\mathrm{coll}}(b) = \sum_{n=1}^{AB} n P(n, b) = A \cdot B \cdot T_{AB}(b) \sigma_{inel.}^{\mathrm{NN}} \tag{1.13}$$

$$\begin{aligned} N_{\mathrm{part}}(b) = \; & A \int T_A(\boldsymbol{s}) [1 - (1 - T_B(\boldsymbol{s} - \boldsymbol{b}) \sigma_{inel.}^{\mathrm{NN}})^B] \mathrm{d}^2 s + \\ & B \int T_B(\boldsymbol{s} - \boldsymbol{b}) (1 - T_A(\boldsymbol{s}) \sigma_{inel.}^{\mathrm{NN}})^A \mathrm{d}^2 s \end{aligned} \tag{1.14}$$

This formulation of the Glauber model is at optical limit where the nucleon density distributions are continuous, and each nucleon in the projectile sees the oncoming target with smooth density. Also the geometry parameters N_{coll} and N_{part} are measured indirectly in experiments, where the mean value of such quantities are extracted for classes of measured events via a mapping procedure. The measured distributions in experiment are mapped to the corresponding distribution obtained from phenomenological analytic or Monte Carlo Glauber calculations. The calculated and measured distributions are

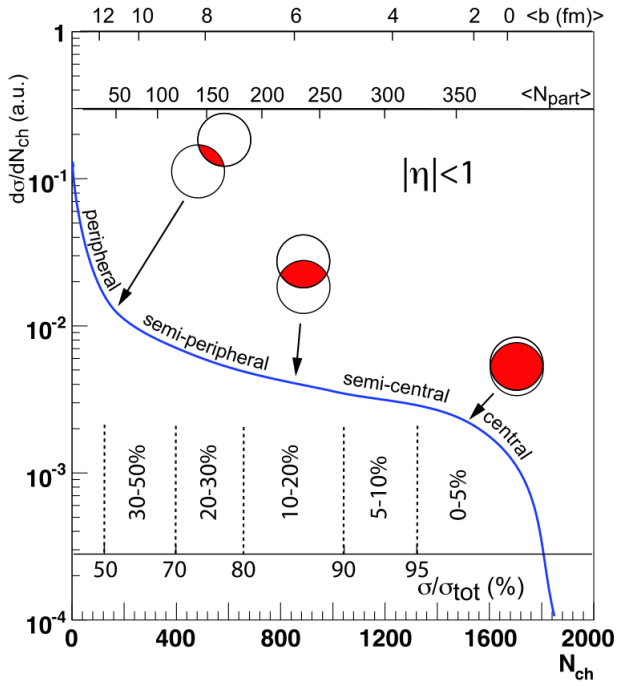

Figure 1.10: The correlation between the final state observable $N_{\rm ch}$ and Glauber calculated quantities $(b, N_{\rm part})$[22].

classified by centrality percentiles, and the mean values are connected for the same centrality classes, which is demonstrated in Fig. 1.10.

The experimentally measured observable distributions mentioned above are the charged particle multiplicity N_{ch} and the energy carried by spectators. The latter can be measured by the energy deposited in the detector which is installed close to the beam direction (e.g. Zero–degree Calorimeter at ALICE). The deposited energy is directly related to the number of spectator nucleons, which constitute the part of the nuclear volume not involved in the interaction. And the multiplicity is monotonically related to the impact parameter b, for which the distribution $\mathrm{d}\sigma/\mathrm{d}N_{\mathrm{ch}}$ are measured. To define the centrality classes, the differential distribution of N_{ch} are binned by the fraction of the total integral. The centrality classes are then obtained defining shape cuts on the distribution, which correspond to well defined percentile intervals of the hadronic cross section σ_{tot} ($0-5\%$,$5-10\%$, etc.). The same procedure is then applied on a calculated distribution for each centrality class, to extract the mean value of Glauber model predictions for geometry quantities $\langle N_{\mathrm{part}}\rangle$ and $\langle N_{\mathrm{coll}}\rangle$.

1.2.2 Particle Multiplicity

The bulk of matter created in heavy–ion collision mainly evolves to soft particles – the majority of produced particles, where the state and the dynamics are described by global event properties of the system such as the multiplicity– the yield distributions of identifies particles, determined by the state of system shortly after hadronization.

Multiplicity is the system produced particle numbers, which characterize the geometry of collision and the initial energy density. The multiplicity distribution in momentum space is proportional to the initial energy density and the effective overlap area of two colliding nuclei, as proposed by J. D. Bjorken[23]:

$$\varepsilon_{\mathrm{Bjorken}} = \langle E_{\mathrm{T}}/N\rangle \, \frac{\mathrm{d}N_{\mathrm{ch}}/\mathrm{d}\eta}{\tau_0 A} \tag{1.15}$$

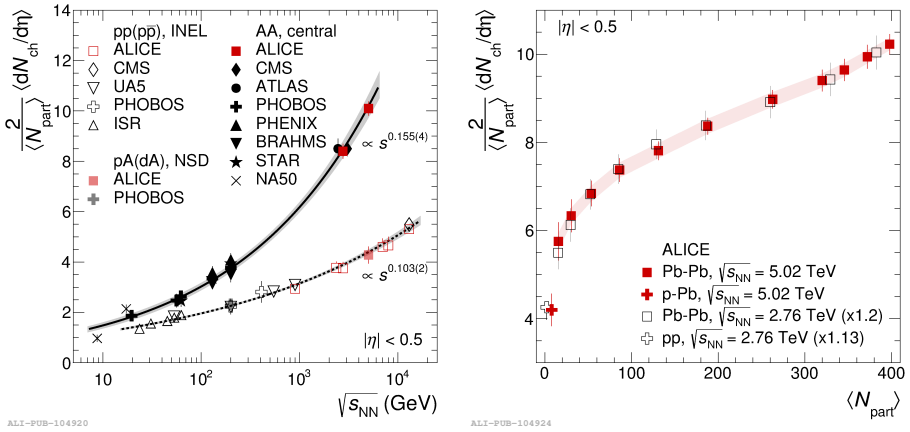

Figure 1.11: The multiplicity distribution with respect to pseudo–rapidity uniformed by $\langle N_{\rm part}\rangle$ measured by ALICE. In the left panel, the multiplicity distributions are compared as a function of the centre–of–mass energy per nucleon–nucleon collision in different systems, while in the right figure, the centrality dependence are shown in different collisions and energies with ALICE[24].

where τ_0 is the thermalization timescale, A is the effective overlap area of two colliding nuclei, and $\langle E_{\rm T}/N\rangle$ is the averaged transverse energy per emitted particle (~ 1 GeV). The charged particle multiplicity is usually scaled by the number of participating nucleons in the collision $\langle N_{\rm part}\rangle$ for the comparison in different collision systems and energies. As shown in Fig. 1.11, the charged particle densities over pseudo–rapidity for proton–proton, proton–nucleus, and central nucleus–nucleus collisions are compared as a function of $\sqrt{s_{\rm NN}}$. The scaled multiplicities in heavy ion collisions increase faster than that in small systems. The comparison is also made for different centrality and collision systems, which are shown in the right panel, from which an increasing trend in multiplicity distribution is find with $\langle N_{\rm ch}\rangle$.

1.2.3 Azimuthal anisotropy

The bulk matter created in nucleus–nucleus collisions expands in collective motion which reflects the hydrodynamic properties of the medium. The underlying physics is pictured in terms of pressure gradients, driving the expan-

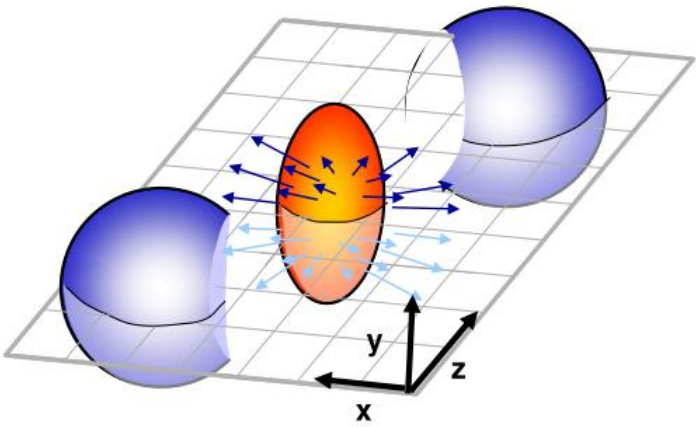

Figure 1.12: A sketch of the semi–central collision, where the almond–shaped collided constituents expand annisotropically under the pressure gradient.

sion of the medium, also referred as flow. It signals the presence of multiple interactions between in–medium particles and shape the overall pattern of the bulk expansion.

In the most central collisions, the initial state after the collision is symmetric azimuthally, which implies that the azimuthal distribution of the final state products are symmetric as well. The pressure gradient in this state will generate a symmetric expansion pattern of the outgoing particles–the radial flow. While in non–central nucleus–nucleus collisions, the pressure gradient is larger in the reaction plane than perpendicular direction, as shown in Fig.1.12. As a result, the developing collective flow, which is proportional to the pressure gradient, leading to an anisotropical distribution in the azimuthal plane of particles. Such distribution is usually quantified via the Fourier expansion as:

$$\frac{\mathrm{d}^2N}{\mathrm{d}\phi\mathrm{d}p_\mathrm{T}} = \frac{\mathrm{d}N}{\mathrm{d}p_\mathrm{T}}\frac{1}{2\pi}\left[1 + 2\sum_{n=1}^{\infty} v_n(p_\mathrm{T})\mathrm{cos}n(\phi - \Psi_n)\right] \tag{1.16}$$

.

The flow mentioned before is represented with the Fourier coefficients $v_n(p_\mathrm{T}) = \langle\cos[n(\varphi - \Psi_n)]\rangle$, where the brackets of average are from all particles in a given p_T interval and centrality class. n is the harmonic order, and

ϕ is the azimuthal angle of the particle momentum. Ψ_n is the angle of the spatial symmetry plane of n–harmonic.

As the first order coefficient v_1 is related to the overall shift of the particle azimuthal distribution, the second coefficient v_2, referred as elliptic flow, has directly connection to the overlap region and the hydrodynamic properties of the QGP[25], such as the equation of state, the transport coefficient, and kinematic viscosity. In low p_{T} region where the soft process dominates, the mass of particles decide the magnitude of v_2 as described by the hydrodynamics[25], which are supported by several measurements performed down to low p_{T}[26]–[34] for charm mesons. At intermediate p_{T}, the hadrons are formed via quark coalescence[35], which indicate higher v_2 for baryons than mesons. In high p_{T} region, the path–length dependent energy loss in the medium is found to contribute the non–zero v_2, as shown in Fig. 1.13.

The kinematic viscosity η/s also reveals the hydrodynamic properties of the QGP. A weakly–interacting bulk matter develop low collective behaviour, as the mean free path of particles in the medium is large and the viscosity as well. This means the QGP behave as gas which could be argued on the basis of asymptotic freedom or Debye screening. Instead, a large flow, theoretically predicted by relativistic viscous hydrodynamic models[36], is built assuming the system reaches the equilibrium rapidly and form a strongly–coupled quark–gluon liquid, which has low viscosity.

1.3 Heavy Flavours

The heavy flavour (charm and beauty) are powerful probes for Quark–Gluon Plasma (QGP) which are formed in ultra–relativistic heavy–ion collisions. Their typical production timescales (0.1 fm/c for charm and 0.02 fm/c for beauty) are relatively shorter than QGP formation time (0.3-1.5 fm/c at LHC energy) and the long lifetime allows them to experience the whole system evolution interacting with the medium constituents. In proton–proton collisions, they are also effective to test the Perturbative QCD (pQCD) predictions due

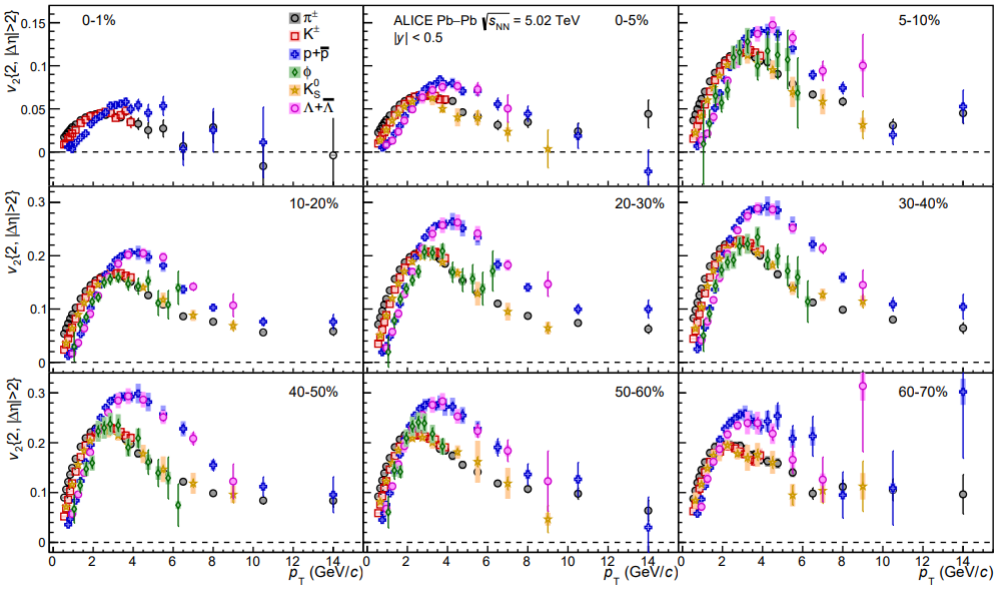

Figure 1.13: The p_{T}–differential elliptic flow v_2 of light particles, in different centrality classes[37]. The elliptic flow is extracted with the scalar product method.

to their large masses, which validates the pQCD calculations at low p_{T}.

1.3.1 Open heavy flavour production in pp collisions

In proton-proton collisions, the production cross section of a high-p_{T} hadron is represented with factorization in QCD terms as:

$$\sigma^{\mathrm{hard}}_{AB\to h} = f_{\mathrm{a/A}}(x_1, Q^2) \otimes f_{\mathrm{b/B}}(x_2, Q^2) \otimes \sigma^{\mathrm{hard}}_{ab\to q}(x_1, x_2, Q^2) \otimes D_{\mathrm{q\to h}}(z, Q^2) \tag{1.17}$$

where $f_{\mathrm{a/A}}(x_1, Q^2)$ is the Parton Distribution Function (PDF), which is a non-perturbative dynamic parameter of the colliding protons structure, represents the possibility of generating a parton flavour a with certain momentum fraction x_1 (Bjorken x) at given transfer momentum Q^2. The last term $D_{\mathrm{q\to h}}(z, Q^2)$ is the fragmentation function which gives the possibility for the parton q fragments into a hadron h with fraction z momentum of the ini-

tial parton. And $\sigma^{\rm hard}_{ab\to q}(x_1, x_2, Q^2)$ is the partonic cross section, calculated as perturbative series in pQCD. In heavy–quark production, there are two processes are involved at the leading order: $q\bar{q} \to Q\bar{Q}$ and $g\bar{g} \to Q\bar{Q}$. At next-to-leading order (NLO) more complicated topologies are included such as GM–VFNS[38]–[40], or at the Fixed Order with Next–to–Leading–Logarithm (FONLL) resummation[41]–[43]. The energy scale dependence of strong coupling constant $\alpha_{\rm s}$ and the momentum transfer Q^2 are uniformed to the same scale for the factorisation μ_f or for the renormalisation $\mu_R \sim \mu_F \sim \sqrt{m_q^2 + p_{\rm T}^2}$.

General–Mass Variable–Flavour–Number Scheme (GM–VFNS) is applicable in wide transverse momentum region, by unifying Fixed Flavour Number (FFN) scheme and Zero–Mass Variable–Flavour–Number scheme (ZM–VFNS). At low $p_{\rm T}$, FFN is applied assuming only light flavour quarks are active in the initial state, while heavy quarks are only considered in the final state. In high–$p_{\rm T}$ region, by applying ZM–VFNS, conventional quarks are regarded as massless parton, where heavy quarks are treated as additional sources as PDF and fragmentation function.

Another pQCD model is Fixed–Order Next–to–Leading–Logarithm (FONLL), which combines Next–Leading–Order (NLO) calculation for low $p_{\rm T}$ and Next–to–Leading–Logarithm(NLL) method at high $p_{\rm T}$. The calculation of cross section is expressed as:

$$\text{FONLL} = \text{FO} + (\text{RS} - \text{FOM0}) \times G(m_{\rm Q}, p_{\rm T}) \tag{1.18}$$

In Eq. 1.18, FO (fix–order) is the NLO calculation at low $p_{\rm T}$ where heavy quarks are considered massive, and FOM0 (massless limit in fix–order) is subtracted from RS (resummed) in the second part to avoid duplication. The function $G(m_{\rm Q}, p_{\rm T})$ is the matching function.

The measurement of heavy quark production at different center–of–mass therefore provides tests of pQCD predictions. The masses of heavy quark ($m_{\rm c} \approx 1.5$ GeV/c, $m_{\rm b} \approx 4.5$ GeV/c) are larger than $\Lambda_{\rm QCD}$, which ensures the validness of perturbative approach at very low transverse momentum region.

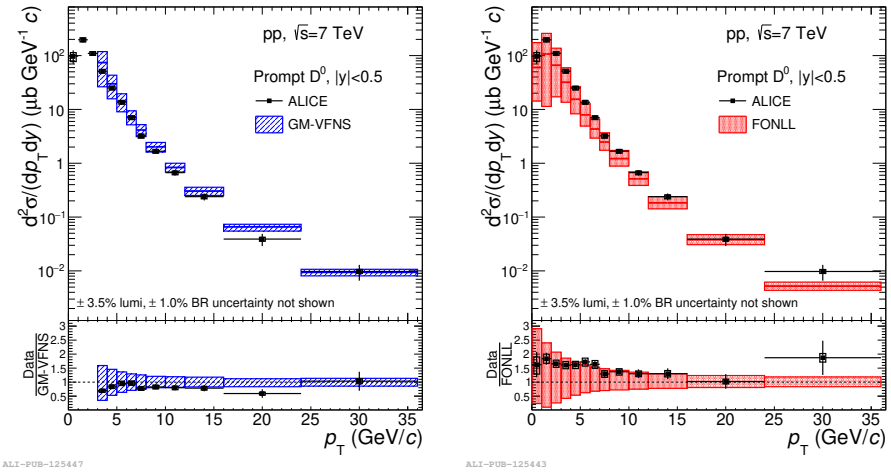

Figure 1.14: Measurements of p_{T}–differential cross section of prompt D^0 mesons at mid–rapidity in pp collisions at $\sqrt{s} = 7$ TeV by ALICE[44], compared with theoritical predictions from GM–VFNS and FONLL.

In this region, the measurement also probes the parton distribution function of proton at small Bjorken x ($\sim 10^{-4}$) and momentum transfer Q^2. The perturbative approaches up to NLO such as GM–VFNS and FONLL were tested and consistent with charm meson measurements in pp collisions at $= 7$ TeV as shown in Fig. 1.14.

1.3.2 Open heavy flavour production in p–Pb and Pb–Pb collisions

In the absence of nuclear and medium effects, the heavy–flavour production in p–Pb (pA) and Pb–Pb (AA) collisions would behave as a superposition of independent nucleon–nucleon (NN) collisions. The yields of charm and beauty in pA or AA then scale from yields in pp collisions proportionally to the average number of binary inelastic NN collisions $\langle N_{\mathrm{coll}} \rangle$ mentioned in the previous section. This ratio, also known as the Nuclear Modification Factor, is expressed as:

$$R_{\mathrm{AA(pA)}} = \frac{1}{\langle N_{\mathrm{coll}} \rangle} \times \frac{\mathrm{d}^2 N_{\mathrm{AA(pA)}}/\mathrm{d}p_{\mathrm{T}}\mathrm{d}y}{\mathrm{d}^2 N_{\mathrm{pp}}/\mathrm{d}p_{\mathrm{T}}\mathrm{d}y} \tag{1.19}$$

which deviate from unity and used to quantify the modifications. The effects can be simply divided into:

- **Initial–state effects** such as the modification of the parton distribution functions in the nucleus. The multiple soft scattering and the radiation in the initial state are also possible to modify the spectra. The initial state effects can be addressed by the measurements in p–Pb collisions.

- **Final–state effects** The final state effects are mainly concern to the interaction of produced hard partons with the hot dense medium formed in the AA collisions, e.g. the partonic energy loss in the medium. The energy loss of heavy quarks were predicted different to that of light quarks due to the mass dependence. And the relative researches allow to investigate the quenching effects in the deconfined medium. Moreover, the heavy partons with low momentum can reach the thermal equilibrium with the medium, where they participate in the collective expansion of the system.

1.3.3 In–medium Energy Loss

Intensive researches have been made about the parton QCD energy loss, which differs from QED due to its non–Abelian nature i.e. the fact that gluons can interact with themselves. The QCD coupling strength $\alpha_{\rm s}$ runs faster than $\alpha_{\rm EM}$ in QED, and the energy scale Q^2 at which $\alpha_s(Q^2)$ is evaluated needs to be explicitly considered in all energy loss calculations. The different coupling of quarks and gluons with medium are also crucial. The relative strengths of the interaction are determined by the Casmir factors, the structure tensor elements of the SU(3) group. These factors are $C_A = 3$ for gluons, and $C_F = 4/3$ for quarks.

Depending on the kinematic region, a colour charged parton interacts with medium with temperature T which leads to transferring energy. There are mainly two mechanisms: elastic processes with the in–medium partons, and the induced radiation of gluons.

Radiative energy loss

The radiative gluon emission by a fast parton in a QCD medium carries away energy from the parton, where the energy loss $\Delta E_{\rm rad}$ can be determined from the corresponding differential gluon Bremsstrahlung spectrum:

$$\langle \Delta E_{\rm rad} \rangle = \int^{E} \int^{k_{\rm T},max} \omega \frac{{\rm d}^2 I_{\rm rad}}{{\rm d}\omega {\rm d}k_{\rm T}^2} {\rm d}\omega {\rm d}k_{\rm T}^2 \tag{1.20}$$

.

As high energy parton produced in hard collisions go through dense QCD medium, it involves a multi–scattering process along its path in the medium. For example in BDMPS[45], [46], it assumes that the medium as static scattering centres. The virtual gluons in the parton pick up transverse momentum $k_{\rm T}$ and can be radiated in the multi–scattering. The characteristic frequency of the radiated gluon that travel a path length L in medium is:

$$\omega_c \sim \hat{q} L^2/2 \tag{1.21}$$

where $\hat{q}$ is the transportation coefficient of the medium, a parameter describes transverse momentum transfer between projectile and medium per path length λ: $\hat{q} = \langle k_{\rm T}^2 \rangle_{\rm med}/\lambda$. For $\omega \ll \omega_c$, the energy spectrum for the radiated gluons has the form:

$$\omega \frac{{\rm d}I}{{\rm d}\omega} \simeq \frac{2\alpha_s C_R}{\pi} \sqrt{\frac{\omega_c}{2\omega}} \tag{1.22}$$

where C_R is the QCD coupling factor (Casmir factor), and $\alpha_s C_R$ for gluon–gluon coupling are 9/4 of that for quark-gluon coupling. The average energy loss of the initial parton then estimated as:

$$\langle \Delta E_{\rm rad} \rangle = \int^{\omega_c} \omega \frac{{\rm d}I_{\rm rad}}{{\rm d}\omega} {\rm d}\omega \propto \alpha_s C_R \omega_c \propto \alpha_s C_R \hat{q} L^2 \tag{1.23}$$

As it suggested, the average radiative energy loss is proportional to the medium transportation coefficient and the square of travel path length. Moreover, it implies significant difference between heavy and light quarks. For heavy quarks with moderate energy, i.e. $m_Q/E \gg 0$, the gluon radiation

is subject to dead–cone effect[47], where the amplitude for gluon–emission within the angle $\Theta < \Theta_0 = m_Q/E$ is suppressed. The dead–cone effect is assumed also for in–medium gluon radiation, where the energy distribution of the radiated gluons for heavy quarks is suppressed by a factor:

$$\omega\frac{\mathrm{d}I}{\mathrm{d}\omega}|_{\mathrm{heavy}}/\omega\frac{\mathrm{d}I}{\mathrm{d}\omega}|_{\mathrm{light}} = \left[1+\frac{\Theta_0^2}{\Theta^2}\right]^{-2} = \left[1+(\frac{m_Q}{E})^2\sqrt{\frac{\omega^3}{\hat{q}}}\right]^{-2} \equiv F_{\mathrm{H/L}}(m_Q/E,\hat{q},\omega) \tag{1.24}$$

.

The dead–cone suppression becomes less as the factor $F_{\mathrm{H/L}}$ increases with higher heavy–quark energy, where the quark mass become negligible. The high–energy part of the gluon radiation spectrum is drastically suppressed as $F_{\mathrm{H/L}}$ decreases at large ω.

Collisional energy loss

The energy transfer between parton and medium constituents is also possible via elastic scatterings which dominates at low particle momentum. The average energy loss in one scattering in QCD medium at temperature T is:

$$\langle\Delta E_{\mathrm{coll}}\rangle \approx \frac{1}{\sigma T}\int_{m_{\mathrm{D}}^2}^{t_{max}} t\frac{\mathrm{d}\sigma}{\mathrm{d}t}\mathrm{d}t \tag{1.25}$$

,

where $t = Q^2$ is the squared momentum transfer, σ is the integrated quark–medium interaction cross section, m_{D} is the Debye mass of medium, which is related to the medium temperature ($m_{\mathrm{D}}(T) \sim gT$). Consider the integral from $m_{\mathrm{D}}^2(T) \sim 4\pi\alpha_s T^2(1+n_f/6)$ to $t_{\mathrm{max}} = s \sim ET$, and the parton–parton differential cross section $\mathrm{d}\sigma/\mathrm{d}t \approx 4\pi C_i\alpha_s^2(t)/t^2$, where $C_i = 9/4, 1, 4/9$ are color factors for gluon–gluon, quark–gluon, and quark–quark scatterings respectively, the parton energy loss inside the medium for light and heavy quarks are[48]:

$$-\frac{\mathrm{d}E_{coll}}{\mathrm{d}l}|_{\mathrm{light,gluon}} = \frac{1}{4}C_R\alpha_s(ET)m_D^2\ln(\frac{ET}{m_D^2}) \tag{1.26}$$

,

$$-\frac{\mathrm{d}E_{coll}}{\mathrm{d}l}|_{\mathrm{heavy}} = -\frac{\mathrm{d}E_{coll}}{\mathrm{d}l}|_{\mathrm{light}} - \frac{2}{9}C_R\pi T^2\left[\alpha_s(m_Q^2)\alpha_s(ET)\ln(\frac{ET}{m_Q^2})\right] \tag{1.27}$$

.

$C_R = 4/3, 3$ for quark–gluon and gluon–gluon couplings. The collisional energy loss ΔE_{coll} is proportional to the thickness of medium and has a logarithmic dependence on the initial parton energy.

For heavy quarks with mass above the typical temperature of the system, a statistical treatment is available for their elastic interaction with medium as diffusion, which can be parametrized in terms of Brownian motion in light particle fluid by Langevin equation[49]:

$$\frac{\mathrm{d}p}{\mathrm{d}t} = -\eta_D(p)p + \xi \tag{1.28}$$

,

where ξ is the momentum–dependent noise term. The diffusion coefficient D_s can be calculated via:

$$D_s = \frac{T}{M\eta_D} = \frac{2T^2}{\kappa} \tag{1.29}$$

.

The combination of energy loss flavour–dependent hierarchy is concluded from discussion above, where the medium effects are expected to be larger for gluons and light quarks than heavy quarks: $\Delta\mathrm{E}_{\mathrm{gluon}} > \Delta\mathrm{E}_{\mathrm{light}} > \Delta\mathrm{E}_{\mathrm{charm}} > \Delta\mathrm{E}_{\mathrm{beauty}}$, as shown in Fig. 1.15 from theoretical predictions[50].

In charm sector, the measurements on prompt D mesons have already given essential insights into the partonic in–medium energy loss and the transport properties. A comparison for measured R_{AA} of prompt D mesons with ALICE

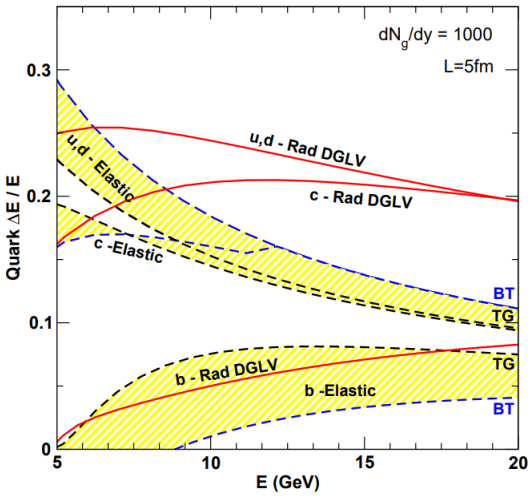

Figure 1.15: Average relative energy loss for light quarks, charm and beauty quarks as a function of the energy. The medium is a longitudianlly expanding QGP with fixed path length $L = 5$ fm, initial gluon density $\mathrm{d}N_g/\mathrm{d}y = 1000$ and fixed $\alpha_s = 0.3$. The radiative energy loss is shown in solid lines while collisional energy loss is presented with dashed bands[50].

to light–flavoured hadrons and J/ψ is shown in Fig. 1.16, where the R_{AA} of prompt D mesons is larger than that of pions for $p_{\mathrm{T}} < 8$ GeV/c. In this region of low and intermediate p_{T}, the difference in p_{T}–differential R_{AA} could originate from mass and colour dependence of in–medium energy loss, as well as several other effects such as soft productions due to the radial flow, and difference in the hadronization. At high p_{T} (≥ 8 GeV/c), similar R_{AA} values are expected[51] for D mesons and pions due to the competitive contributions between radiative energy loss and the different p_{T}–distribution and fragmentation functions of charm and light quarks.

The QGP transport properties could be constrained by the measurement of collective motion of charm–quarks in the medium. The comparison of the R_{AA} and v_2 of prompt D mesons to the models implementing charm transport in a hydrodynamically expanding QGP is presented in Fig. 1.17, where the constraints to the spatial diffusion coefficient D_s are derived from their accuracy in simultaneously describing R_{AA} and v_2. The models that describe both

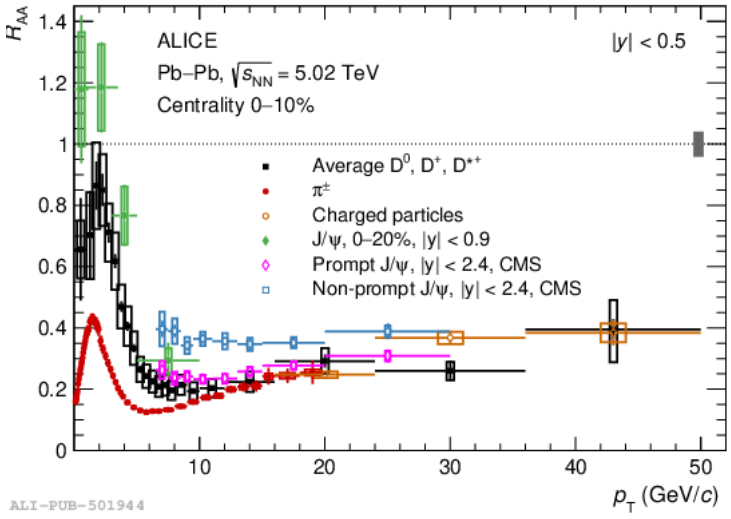

Figure 1.16: R_{AA} of prompt D mesons in the 0–10% centrality measured in Pb–Pb collisions at $\sqrt{s_{\mathrm{NN}}} = 5.02$ TeV with ALICE[52], compared to charged particles[53], [54] and J/ψ[55], [56].

observable well use a value of heavy–quark spatial diffusion coefficient in the range $1.5 < 2\pi D_s T_c < 4.5$ at $T_{pc} = 155$ MeV.

A first look into the different R_{AA} of particles originating from charm and beauty quarks is in the comparison of non-prompt and prompt J/ψ, and prompt D mesons. In Fig. 1.16, the R_{AA} of prompt D in the 0–10% centrality class in lower than that of non-prompt J/ψ, which comes from beauty hadron decays. This difference indicates the predicted quark–mass dependence of in–medium energy loss. However a full modelling of the initial partonic p_{T} spectrum, the fragmentation, and the beauty–hadron decay kinematics are needed to acquire further interpretation. Also, the measurement of different non-prompt mesons can provide the crucial but missing information especially at low p_{T}.

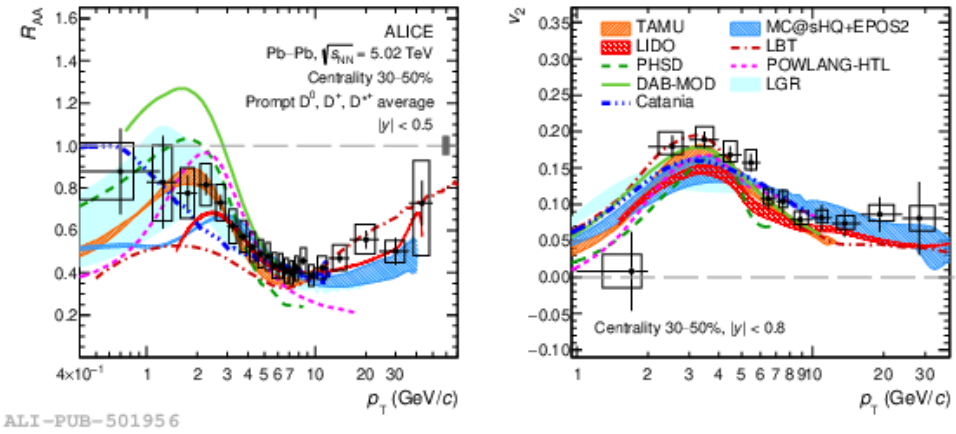

Figure 1.17: R_{AA} and v_2 of prompt D mesons in the 30–50% centrality measured in Pb–Pb collisions at $\sqrt{s_{\mathrm{NN}}} = 5.02$ TeV with ALICE[52], [57], compared to model predictions implementing the charm transport in a hydrodynamically expanding QGP[34], [58]–[76].

Chapter 2

The ALICE Experiment at the LHC

In this section, the ALICE experiment at the LHC will be introduced. Firstly, a brief overlook to the LHC at CERN will be given. Then an overview of ALICE setup and parameters will be shown, and the most related detector will be discussed further in this part, such as the trigger systems, the central barrel detectors, especially the techniques of detectors concerning the reconstruction of the vertices and tracks.

2.1 The Large Hadron Collider

The Large Hadron Collider (LHC), built underground about 100 meter with a circumference around 27 kilometer, is located near Geneva, Switzerland, which is the largest and most powerful particle accelerator. It was built from 1998 to 2008 by the European Organisation for Nuclear Research (CERN), and was designed for the discovery of the Higgs boson, to explore its properties, and for searching the physics beyond the Standard Model. It was also designed for working at the luminosity of 10^{34} $\mathrm{cm}^{-2}\mathrm{s}^{-1}$ for proton collisions or 10^{27} $\mathrm{cm}^{-2}\mathrm{s}^{-1}$ for lead ion collisions, with the centre–of–mass energy at 14TeV for pp and 5.5TeV for Pb–Pb collisions[77].

The overview of the CERN accelerator complex is shown in Fig. 2.1. The LHC at the upper part was built and installed inside the tunnel used to

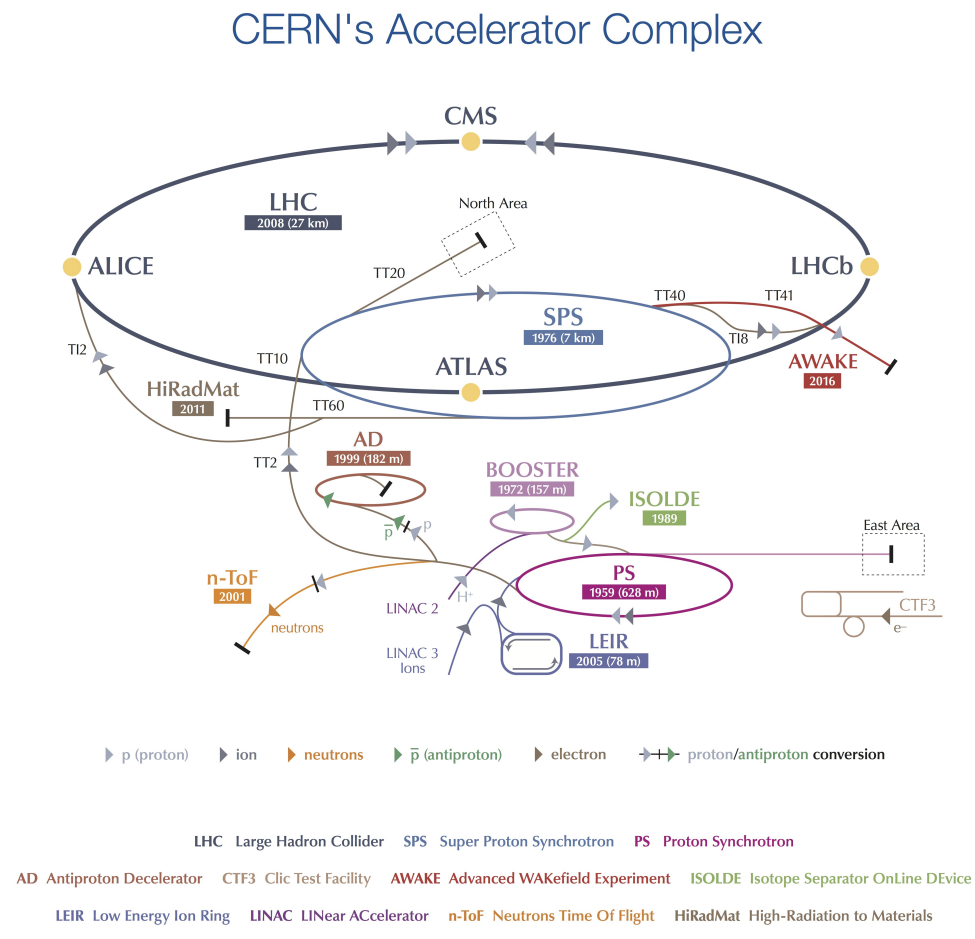

Figure 2.1: The overview of CERN accelerator complex

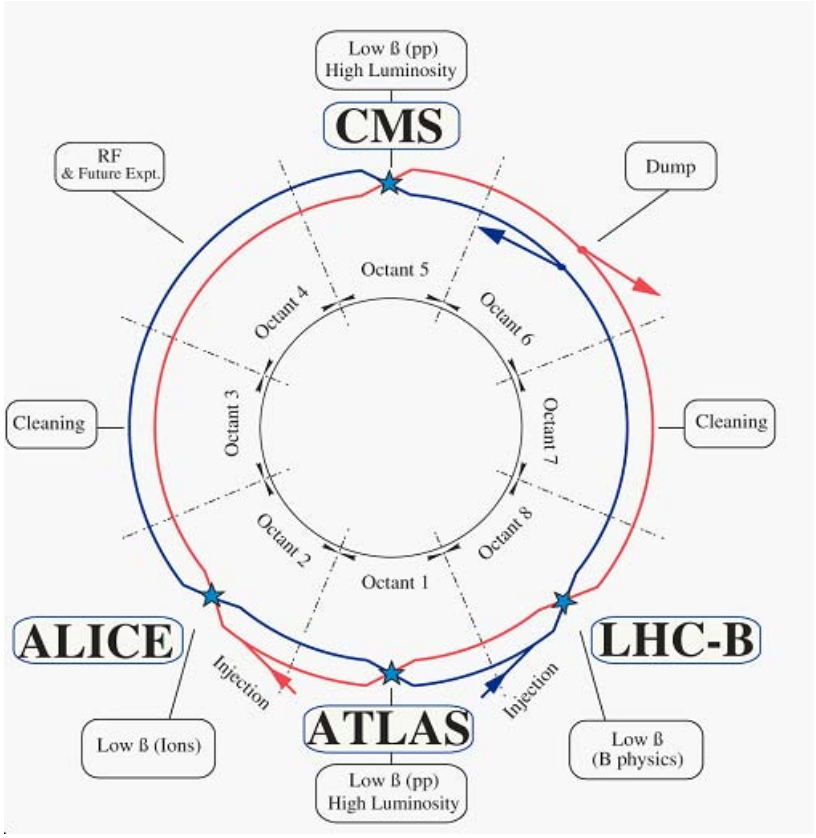

Figure 2.2: A schematic layout of the LHC, where clockwise (red) and anti-clockwise (blue) beam pipes are divided into 8 octants.

contain the LEP accelerator and collider. The tunnel was divided into eight straight sections and eight arc sections, and the design of the LHC follows the same geometry. Two transfer tunnels were bulit between the LHC and the injector chain facilities which are at CERN complex and mainly in the lower part of the Fig. 2.1. The protons or the heavy ions were injected and transferred into a chain of accelerators: Proton Synchrotron Booster (PSB) $\rightarrow$ Proton Synchrotron (PS) $\rightarrow$ Super Proton Synchrotron (SPS), which had been upgraded to meet the needs for many high intensity proton bunches of the LHC.

The LHC is made of two rings of counter–rotated beam pipe, where the vacuumed pipes were magnetically–confined by the superconducting magnets

that operates at field above 8 T. The temperature of the magnets were kept below 2K with the cryogenic system supplied with superfluid helium, which provides both effective thermal conductivity and powerful stabilizing action against the thermal disturbances. From the schematic layout in Fig. 2.2, the arcs of two LHC rings were divided into 8 octant sections, and each straight section can serve as experimental or utility insertion. At point 1 and 5, two high luminosity experimental insertions are located at diametrically opposite straight sections, where the ATLAS[78] and the CMS[79] experiments were installed. While at point 2 and 8, the experimental insertion for heavy ions and beauty physics, for the ALICE and LHCb experiments, were located with different injection systems.

In 2009, the LHC started its first proton–proton collision at $\sqrt{s} = 0.9$ TeV. In the first run period (2009–2013) of the LHC, 3 dedicated heavy–ion programs were processed, produced Pb–Pb collisions data at $\sqrt{s_{\rm NN}} = 2.76$ TeV in 2010 and 2011. After the first long shutdown (LS1), LHC restarted in 2015 for Run 2, ramping up to the designed centre–of–mass energy of pp collision at $\sqrt{s} = 13$ TeV. The heavy–ion collision data was collected at 2015 and 2018 for Pb–Pb collisions at $\sqrt{s_{\rm NN}} = 5.02$ TeV, and for Xe–Xe collisions. Now the LHC is at its second long shutdown (LS2) and upgrading the 4 experiments. The data–taking in Run 3 is expected to begin in 2022–2023.

2.2 The ALICE Apparatus

ALICE (A Large Ion Collider Experiment)[80], [81], is a general–purpose heavy–ion detector at the LHC, which focused on the QGP at extreme energy density and temperature, produced in ultra–relativistic nucleon–nucleon collisions. It is designed to address the physics of the strong interaction matter and the quark–gluon plasma, and allows a comprehensive study of hadrons, electrons, muons, and photons produced in the collision of heavy–nuclei, up to the highest multiplicities anticipated at the LHC.

The overall layout of ALICE is presented in Fig. 2.3, with the dimensions

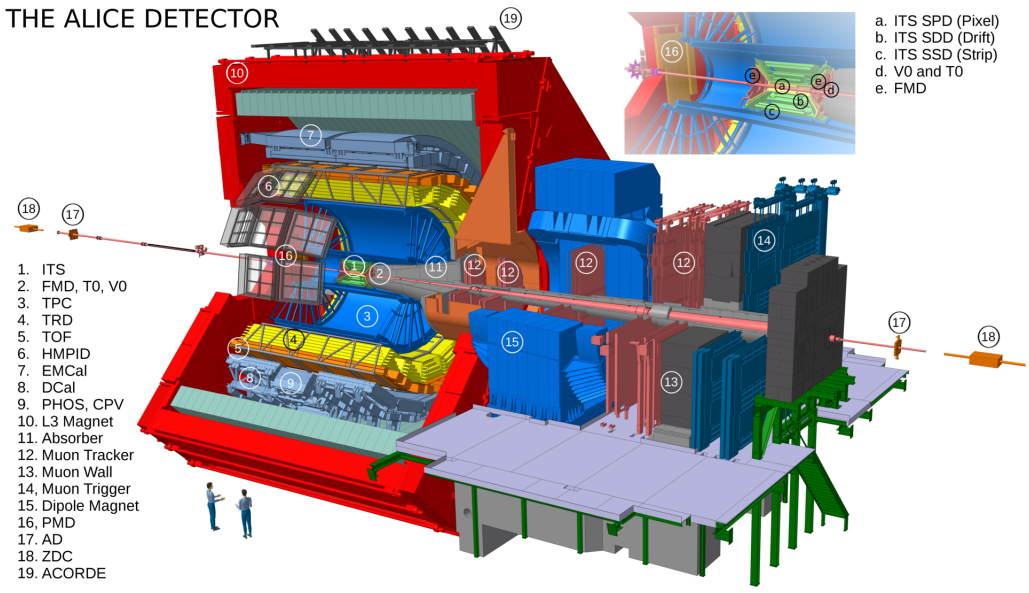

Figure 2.3: The overview of ALICE detectors, where the name of detector components are labeled.

at $16 \times 16 \times 26$ m^3 and the total weight of about 10000 t. It is mainly consists of a central barrel, which measures hadrons, electrons, and photons, and a forward muon spectrometer. Several smaller detectors (ZDC, PMD, FMD, T0, V0) are also assembled, for global event characterization and triggering. An array of scintillators (ACORDE) on top of the L3 magnet is used to trigger on cosmic rays.

The central barrel detectors, which provide the most of information for this work, is consists of several of detectors. From inside out, the barrel contains an inner tracking system (ITS), a cylindrical Time–Projection Chamber (TPC), three particle identification arrays of Time–of–Flight, Ring Imaging Cherenkov (HMPID) and Transition Radiation detectors (TRD), and two electromagnetic calorimeters (PHOS and EMCal). All central barrel detectors except HMPID, PHOS, and EMCal cover the full azimuth as sketched in Fig. 2.4. The central barrel in assembled and embedded inside a large magnet solenoid reused from the L3 experiment at LEP. A summary table for the spatial parameters of each detector was shown in Tab. 2.1.

Detector	Acceptance (η, ϕ)	Position (m)	Dimension (m^2)	Channels
ITS layer 1,2 (SPD)	$\pm 2, \pm 1.4$	$0.039, 0.076$	0.21	9.8M
ITS layer 3,4 (SDD)	$\pm 0.9, \pm 0.9$	$0.150, 0.239$	1.31	133 000
ITS layer 5,6 (SSD)	$\pm 0.97, \pm 0.97$	$0.380, 0.430$	5.0	2.6M
TPC	± 0.9 at r = 2.8 m	$0.848, 2.466$	readout 32.5 m^2	557 568
	± 1.5 at r = 1.4 m		Vol. 90 m^3	
TRD	± 0.84	$2.90, 3.68$	716	1.2M
TOF	± 0.9	3.78	141	157 248
HMPID	$\pm 0.6,\ 1.2° < \phi < 58.8°$	5.0	11	161 280
PHOS	$\pm 0.12,\ 220° < \phi < 320°$	4.6	8.6	17 920
EMCal	$\pm 0.7,\ 80° < \phi < 187°$	4.36	44	12 672
ACORDE	$\pm 1.3,\ -60° < \phi < 60°$	8.5	43	120
Muon Spectrometer				
Tracking station 1	$-4.0 < \eta < -2.5$	-5.36	4.7	1.08 M
Tracking station 2		-6.86	7.9	
Tracking station 3		-9.83	14.4	
Tracking station 4		-12.92	26.5	
Tracking station 5		-14.22	41.8	
Trigger station 1	$-4.0 < \eta < -2.5$	-16.12	64.6	21 000
Trigger station 2		-17.12	73.1	
ZDC:ZN	$\lvert\eta\rvert < 8.8$	± 116	2×0.0049	10
ZDC:ZP	$6.5 < \lvert\eta\rvert < 7.5$	± 116	2×0.027	10
	$-9.7° < \lvert\eta\rvert < 9.7°$			
ZDC:ZEM	$4.8 < \eta < 5.7$	7.25	2×0.0049	2
	$-16° < \phi < 16°$ and			
	$164° < \phi < 196°$ and			
PMD	$2.3 < \eta < 3.7$	3.64	2.59	2 221 184
FMD disc 1	$3.62 < \eta < 5.03$	inner : 3.2		
FMD disc 2	$1.7 < \eta < 3.68$	inner : 0.834	0.266	51200
		outer : 0.752		
FMD disc 3	$-3.4 < \eta < -1.7$	inner : -0.628		
		outer : -0.752		
V0A	$2.8 < \eta < 5.1$	3.4	0.548	32
V0C	$-3.7 < \eta < -1.7$	-0.897	0.315	32
T0A	$4.61 < \eta < 4.92$	3.75	0.0038	12
T0C	$-3.28 < \eta < -2.97$	-0.727	0.0038	12

Table 2.1: Summary of the ALICE detector subsystems. The acceptance in η is calculated from the nominal interaction point and is 360° in azimuth, unless noted otherwise. The position is the approximate distance from the interaction point to the face of the detector and correspond to the radius for barrel detectors (inner and outer radius for the TPC and TRD) or the position along the beam ($z$coordinate) for the others. The dimension corresponds to the total area covered by active dector elements. 'Channel' is the total number of independent electronic readout channels. In case a detector is subdivided, the numbers refer to the individual components (e.g. pixel layers 1 and 2, muon tracking station 1–5).

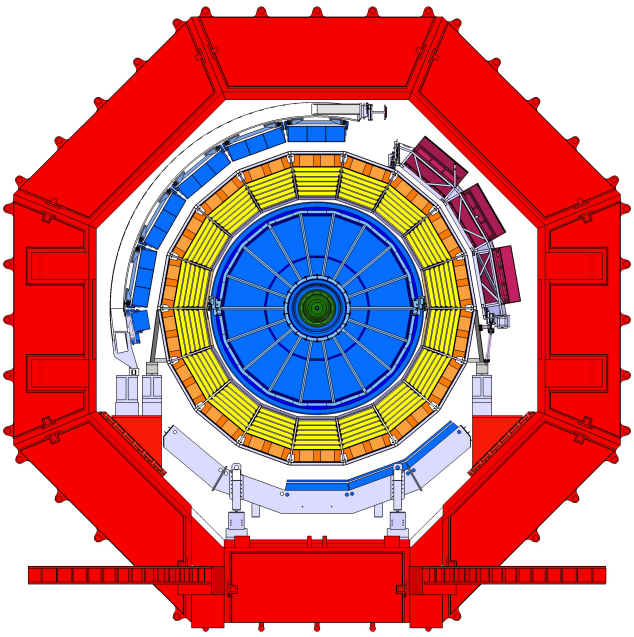

Figure 2.4: The ALICE detectors in cross section view.

2.2.1 Inner Tracking System

The Inner Tracking System (ITS)[80], [82] was installed the inner most of the central barrel, which surrounds the beam pipe with the radius from 3.9 to 43.0 cm (the outer diameter of the beam pipe is 6 cm). It also covers the pseudo–rapidity range of $|\eta| < 0.9$ for all vertices within the interaction diamond (1σ, i.e. 5.3 cm along the beam direction).

The ITS consists of six layers of silicon semi-conductor detectors, where from inside out are the Silicon Pixel Detectors (SPD) for two innermost layers, the Silicon Drift Detectors (SDD) for two intermediate layers, and Silicon micro–Strip Detectors (SSD) as the outer two.

As the two inner most layers, the SPD is the fundamental element for the determination of vertex positions and the impact parameter of secondary tracks originated from the weak decays of strange, charm, and beauty particles. The detector is consisted of hybrid silicon pixels as basic unit which is formed with a two–dimensional matrix of silicon detector chips. And the silicon pixels

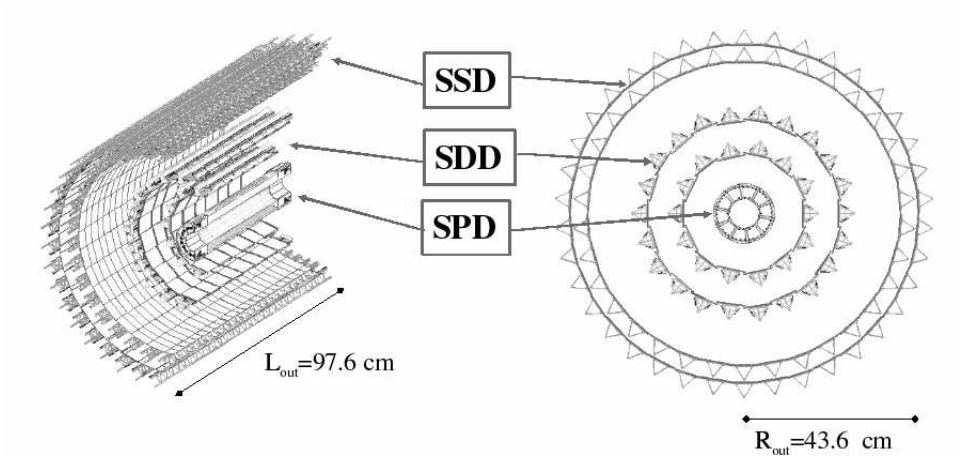

Figure 2.5: The layout of ITS[80]. From inside out the ITS barrel consists of 6 layers of silicon conductor detectors and each two layers form up to the subdetectors SPD, SDD and SSD.

were installed onto the half–stave shaped detector module, along with the reading unit for Multi–Chip module and one high density aluminum/polyimide multilayer interconnect. The sensor matrix includes 256×160 cells, and in boundary region the cells are longer to ensure the coverage between readout chips. Each cell will give a binary readout whenever the preset signal threshold level is triggered. The half–stave shaped detector modules are attached by two and head–to–head along the z direction to a carbon–fibre support sector, with the Multi–Chip modules at two ends to form full staves. Each sector supports six staves: two on the inner layer and four on the outer layer. And in total ten sectors (60 staves) are mounted around the beam pipe to close the full barrel, to provide 9.8×10^6 reading cells and sustain the track density as high as 50 tracks/cm^2.

The Silicon Drift Detectors (SDD), two intermediate layers of the ITS are mainly made of high homogeneous high–resistivity (30 k$\Omega \cdot$ cm) 300 μm thick Neutron Transmutation Doped silicon, where each unit of the SDD has a sensitive area of 70.17(rϕ) $\times$ 75.26(z) mm^2. The area is split into two drift regions by the central cathode strip with high voltage bias of $-2.4\ kV$ applied. And in each drift region, on both surfaces of the detector, a stable drift field was gen-

erated parallel to the surface by the cathode strips, and the degrading of the high voltage to the zero potential of the detector boundary was implemented by two insensitive guard regions. When a track pass through, the dE/dx information of the is encoded into the signal amplitude. A SDD detector module consists of one SDD unit and two front–end hybrids, each connected to the corresponding low–voltage board. And a specially designed micro–cable carrying the HV is connecting the detector to the HV board. The modules are assembled and mounted on a linear–structured ladder with V–shape cross section. There are 14 ladders and with six modules each on layer 3, and 22 ladders with eight modules on layer 4. The ladders were then assembled on a Carbon Fibre Reinforced Polymer (CFRP) cylindrical structure with two cones and 4 support rings, and prepared to be installed coaxial to the beam pipe.

As two outer layer of the ITS, the Silicon Strip Detectors (SSD) are crucial for the matching of tracks from the TPC to the ITS. Additionally, it provides two–dimensional position of the tracks, and measures dE/dx information to assist the particle identification for low–momentum particles. Both two layers uses double sided strip detectors for the sensors, which have 768 strips on each side with a pitch of 95μm and thickness of 300μm. The sensor are mounted to the ladders of same design as SDD, and assembled to the linear Carbon Fibre Composite (CFC) material support structure, nearly parallel to the magnetic field in order to optimize the resolution in the bending direction. Each ladder carries up to 25 modules along the beam direction, and 72 ladders carrying up to 1698 modules.

2.2.2 Time Projection Chamber

The Time Projection Chamber (TPC)[83] is the main tracking of the central barrel, designed to provide measurement of charged tracks within wide transverse momentum range from 0.1 to 100 GeV/c together with other central barrel detectors, performed well in separation of two–tracks, PID and vertex determination. It is made of a large cylindrical field cage with inner (outer) radius of about 85 (250)cm, 500 cm of length, filled with $Ne/CO_2/N_2(90/10/5)$ gas, in

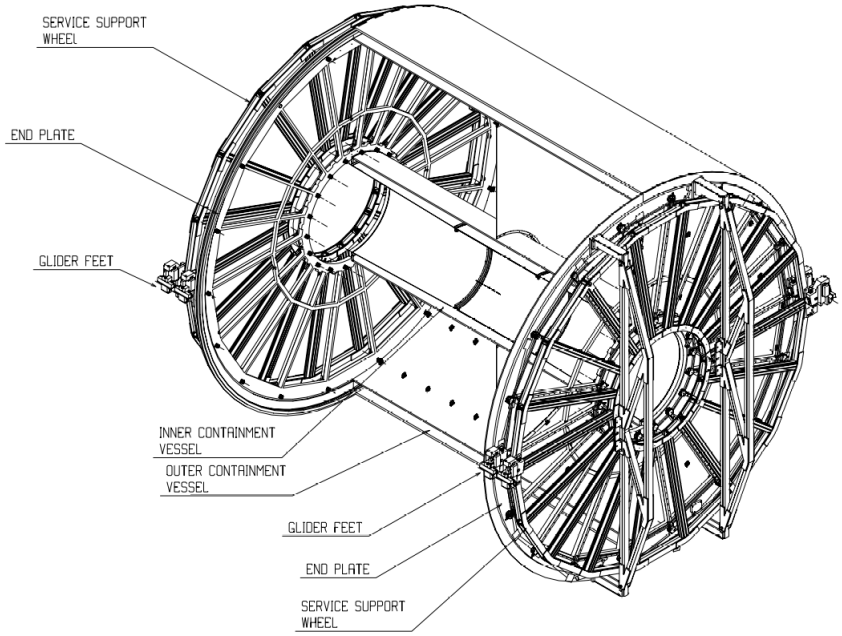

Figure 2.6: 3D schematic layout of TPC[83]. The field cage and support wheel are displayed, and the reading chambers are to be installed at the end plate.

which the primary electrons created by charged tracks are transported over a distance of up to 2.5m on either side of the central electrode to the end plates. At the end plates, the Multi–Wire Proportional Chambers (MWPC) with cathode readout are mounted into the 18 trapezoidal sectors. The coverage in phase space includes the full azimuth and the $|\eta| < 0.9$ of pseudo–rapidity, which matches ITS, TRD, and TOF detectors. With the size of field cage and the number of readout chambers, the ALICE TPC provides good dE/dx resolution of 5% for isolated tracks, and 6.8% at high multiplicity dN/dy = 8000.

2.2.3 The Time–Of–Flight detector

The Time–Of–Flight (TOF)[84] detector is an large area array of Multi–gap Resistive–Plate Chambers (MRPC), which covers the pseudo–rapidity range $|\eta| < 0.9$ for Particle IDentification (PID) in the intermediate momentum

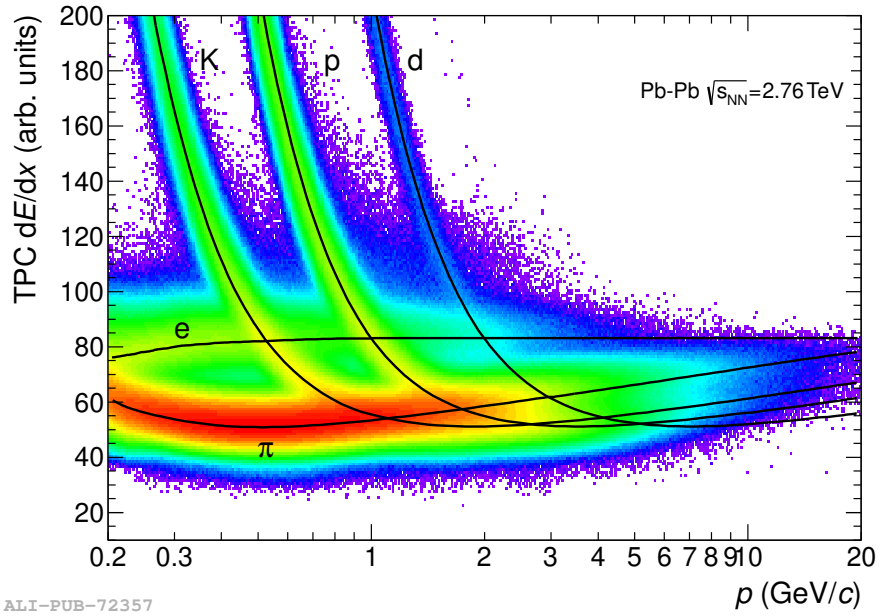

Figure 2.7: Energy loss ($\mathrm{d}E/\mathrm{d}x$) in the TPC versus particle momentum in Pb–Pb collisions at $\sqrt{s_{\mathrm{NN}}} = 2.76$ TeV. The curves of parametrization show the expectation for a specific type of particle[81].

range, below 2.5 GeV/c for pions and kaons, up to 4 GeV/c for protons, with a π/K and K/p separation better than 3σ. In coupled with the ITS and TPC for track and vertex reconstruction and for dE/dx measurements in the low–momentum range (up to about 1 GeV/c), the TOF will provide event–by–event PID of large samples of pions, kaons, and protons. The MRPCs[84] has better response speed and time resolution than other parallel–plate chambers, ensure a low overall occupancy rate (14% for $\mathrm{dN}/\mathrm{d}\eta = 8000$, and 10^{-4} for pp) with more than 10^5 independent TOF channels. The basic unit of the TOF is a 122 cm long and 13 cm wide 10–gap double–stack MRPC strip, subdivided into two rows of 48 pads. The strips are placed inside gas–tight modules, and positioned transversely to the beam direction. Five modules in three different types, where the central modules have 15 strips, 19 for the two intermediate and two external modules, closed inside a box that defines and seals the gas volume and supports the external front–end electronics and devices. Then this five modules in a row are located inside a supermodule

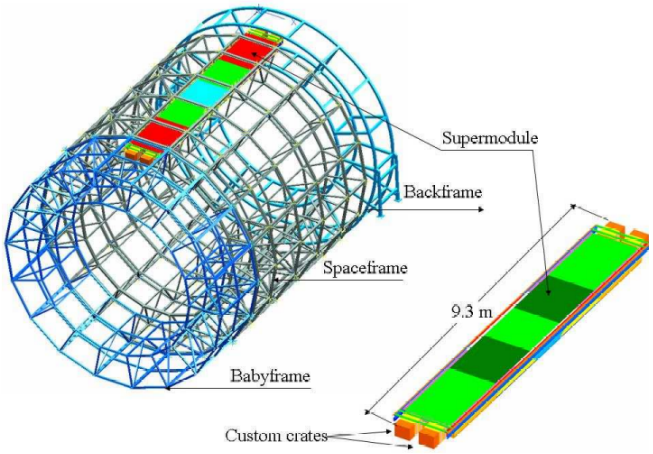

Figure 2.8: A schematic drawing of the TOF detector[84] and one supermodule installed, where each super module consists of 5 MRPC modules.

framework of longitudinal and transverse aluminium beams for each of 18 sectors. A complete TOF system consists 90 modules.

2.2.4 V0 detector

The V0 detector consists of two arrays of scintillator counters, V0A and V0C, located 340 cm from the vertex on side opposite to the muon spectrometer, while the V0C is located 90 cm from the vertex on the other side. Both V0A and VOC are covering small angles with $2.8 < \eta < 5.1$ and $-3.7 < \eta < -1.7$, to provide the minimum–bias triggers for the central barrel detectors in pp or heavy–ion collisions. These triggers are given by particles originating from initial collisions and from secondary interactions in the vacuum chamber elements. The V0 also functions as an indicator of the centrality via the multiplicity recorded in the event, as the number registered particles on the V0 array is monotone to the number of primary emitted particles. Three types of triggers were used, the multiplicity, semi–central, and central trigger, and the centrality of the heavy–ion collisions was determined with V0A and V0C with NBD–Glauber fit.

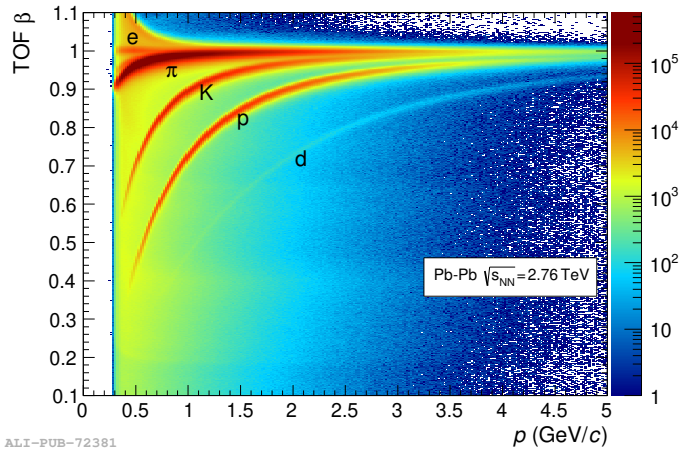

Figure 2.9: TOF detector measured β distribution versus particle momentum in Pb–Pb collisions.

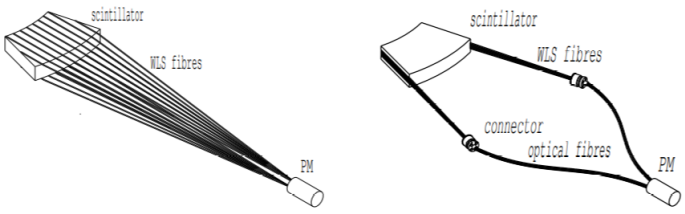

Figure 2.10: Schematic design of the V0A (left) and V0C (right) detectors[80].

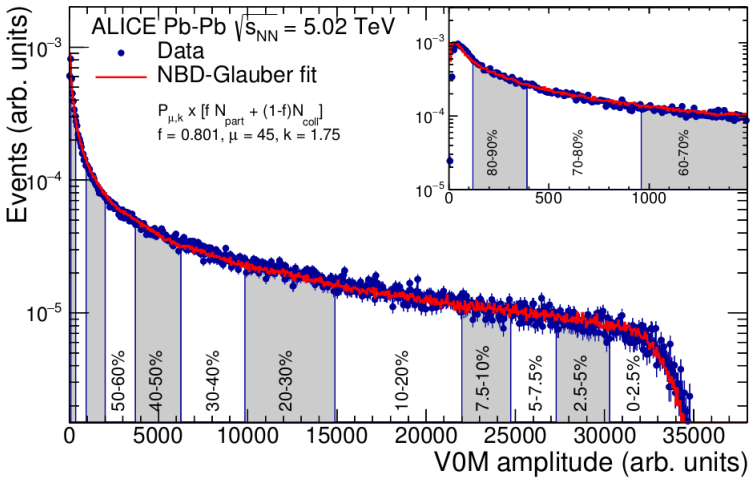

Figure 2.11: A distribution of the V0 amplitudes where the readings from V0A and V0C are summed. With the NBD–Glauber fit, the distribution is divided into percentile categories as indicated in the figure[85].

2.3 Trigger system

The trigger system applied in ALICE data–taking is designed to select collision events of interest and control the data–generate rate down to suit the physics requirements and the bandwidth restriction. the triggers were controlled by the ALICE Central Trigger Processor (CTP) which makes use of various component detectors with widely different periods and intrinsic response time, and is optimized to cope with several running modes such as ion(heavy–ion), pA, and pp, where the counting rate varies by almost two orders of magnitude.

The fast part of the trigger was designed to be able to respond the high multiplicity event in Pb–Pb collisions (interaction rate 8 kHz at $\mathcal{L} = 10^{30}$ cm^{-2}s^{-1}), which is split into a Level 0 (L0) signal ($\tau = 1.2$ μs), and a Level 1 (L1) signal ($\tau = 6.5$ μs). The 24 inputs for L0 trigger include mainly MTR, ACORDE, T0, V0, and some partial readouts, which arrive too fast to receive all trigger inputs. And the 24 inputs for L1 trigger are mainly from PHOS, TOF, TRD, ZDC, and EMCal, which pick up all remaining fast inputs. The final level of the trigger (Level 2, L2), which waits for a relatively long period ($\tau = 88$ μs), was designed to monitor and reject the event that contains more than one col-

lision, the "pile–up" event. The logic combination of trigger conditions were categorized into 50 classes, and distributed by the RD12 Trigger Timing and Control (TTC) system[80]. For example the Minimum–Bias (MB) trigger, which enforces least trigger conditions while still rejects empty event, requires a logic OR between SPD–MB trigger and the V0 trigger.

Apart from the sensor–level triggers, the Data–AcQuisition system (DAQ) and a software–level High–Level Trigger (HLT) were designed to utilize the limited total bandwidth of data–recording efficiently. The most common triggers such as MB, central, and semi–central will take a large fraction of the total DAQ bandwidth, while the rare triggers such as dimuon or dielectron, use less bandwidth and are limited by the detector livetime and the luminosity. The HLT, on the other hand, consists of a series of online calibration, event reconstruction, and data–processing, co–processes and compresses the raw data from detectors while keeps the data–record ongoing simultaneously.

2.4 Track and vertex reconstruction

The track finding and the determination of the primary collision vertex in the central barrel are performed started with clusterization, where the detector data are converted into clusters characterized by spatial positions, signal amplitudes, signal times, and the associated uncertainties. The clusterization is performed for each detector separately. The next step is the reconstruction of the interaction vertex using clusters recorded in SPD. Then the tracks of particle are reconstructed with track–finding and fitting with TPC and ITS with Kalman filter[86]. The final interaction vertex is determined using the reconstructed tracks.

The first step of tracking is performed with SPD, where the tracklets, the connecting lines between clusters in two layers of SPD, are extrapolated inwards. The point where the tracklets converge is extracted as the interaction vertex. Usually in pp collisions, where the pile–up event is expected, the algorithm is repeated multiple times discarding those cluster at each iteration

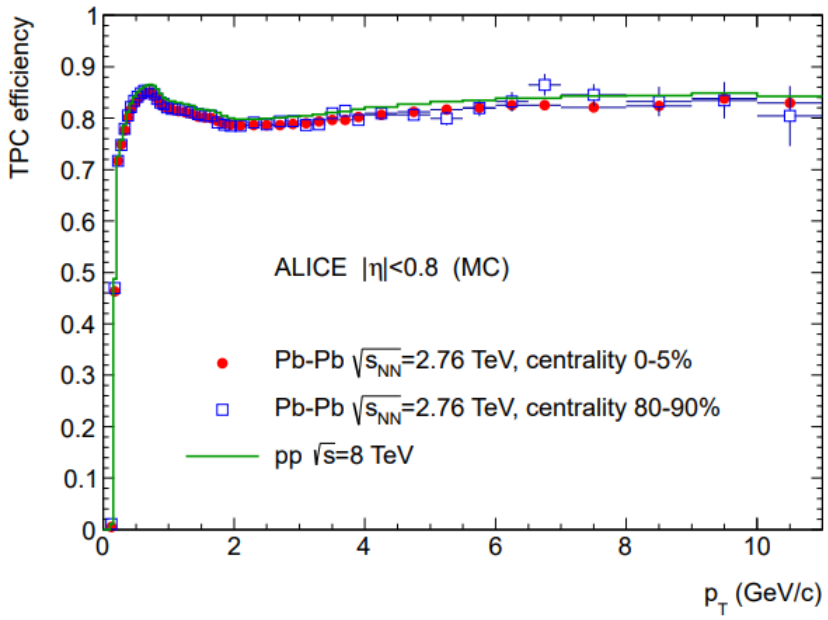

Figure 2.12: The efficiency for TPC tracking from Monte–Carlo simulations for different collisions[81].

which contributes to vertices found in previous iterations.

After primary vertex reconstruction, the tracks are found and fitted in three stages. From the out–most reading pad in TPC, the track search starts with TPC clusters and the vertex point, then propagated inwards and update the covariance matrix with the nearest clusters that fulfil a proximity cut. The track–finding ends until it reaches the inner TPC radius. After that, the track is propagated to primary vertex with clusters in ITS layers. The procedure is repeated but starts from the primary vertex and propagated outwards, followed by a final inwards propagation and refitting for the final track parameters and uncertainties. In Fig. 2.12, the tracking efficiency with TPC is obtained from Monte–Carlo simulations which is defined as the ratio of reconstructed tracks number over generated primary particles. The losses of tracks during reconstruction process are due to the multiple scattering in detector material and the dead–zone of readout in the detector.

The final interaction vertex is found using the tracks reconstructed in TPC

and ITS, by extrapolating the tracks inwards and searching for the closest approach to the nominal beam–line of the collisions. The precise vertex position is obtained by performing fit using track–weighting by their uncertainties to suppress the contribution of any outliers.

Chapter 3

Analysis Method

In this chapter, the analysis methods utilized for heavy flavor topics are introduced. Firstly, a machine–learning based method boosted decision trees are introduced as classifier for signal–background separations. And a method based yielding minimization of χ^2 for the disentangling two components in the signal, prompt and non–prompt part which will be introduced in the next chapters, is presented as well.

3.1 Boosted Decision Trees

The boosted decision trees (BDT) method utilize a series of decision trees which produced from data training, to categorize the input objects in binary–classification problems which are simply to categorize the objects into two classes (signal or background for instance). The methods to determine classification are mainly based on the inputs which could be either organized data e.g. some arrays of numbers, or any non–structed data like pictures and audio clips. In this analysis, only organized inputs will be discussed.

Although many methods are already developed to help solving binary classifications, BDT still has advantages with its simplicity and accuracy. The decision tree is a tree–form structure with nodes and branches as shown in Fig. 3.1. An input with an array of characteristic data needs to go through the decision tree from root node (top) to leaf node (bottom). At each node, the

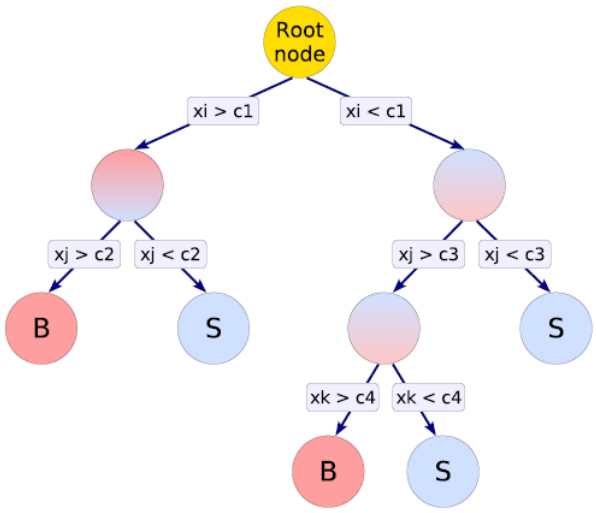

Figure 3.1: An example decision tree schematic view[87]. The decision is made following the condition criteria on the arrows from node to node.

input goes through either right branch (signal) or left branch (background) depending on the decision condition. Finally at the bottom nodes it gives signal/background predictions.

For large data samples, it is usually impossible to give perfect predictions for decision trees, and some of the predictions are false. These false predictions are considered by evaluating with a meta–data set which the natural classes of each input are already known (e.g. signals and backgrounds). The evaluation is then based on the composition of true and false signals/backgrounds, specifically the loss function. There are several popular options such as the Gini index, cross–entropy. In this case, the Gini index is defined as:

$$\text{Gini} = 1 - \sum_i p_i^2 = \frac{2 \cdot \text{S} \cdot \text{B}}{(\text{S} + \text{B})^2} \tag{3.1}$$

The Gini index itself describe the possibility of any incorrect classification when the discrete possibility for each class equals to p_i. In this topic, the possible classes are limited between signals and backgrounds. Therefore the formula is simplified to the r.h.s. of the equal sign. To improve the performance of decision tree, each node needs to be adjusted by minimizing the loss

function based on the meta-data mentioned above. The minimization in this analysis is accessed by a bisection search method within the range $[a_{min}, a_{max}]$, which represent the maximum and the minimum of the meta–data set. In particular for multi-variate analysis, the data set is usually consist of variable arrays denote as $(a_i, b_i, c_i, ...)$. The search of minimizing the loss function then also take which variable into consideration. And the decision condition found is attached to the tree node as $(x_i > c_i)$ as illustrated in Fig. 3.1.

3.1.1 Boosting

The major drawback of the decision tree method is their simple structures which fits the specific data–set for training. Therefore the performance of decision tree shows sensitivities towards imperfection and fluctuations within the training data–set, which leads to instability of their outputs. To overcome this problem, an combination of decision trees and machine–learning, the boosted decision trees (BDT) is applied for this analysis.

Boosting is an early idea of machine–learning methods which applies enhancement mechanism to the training processes of decision trees. Instead of requiring each decision tree to yield high signal–background separation, which usually lead to large depth of trees, it combines the classification result of several weak decision trees. For the BDT method, it utilized a series of decision trees generated with boosting which re–weight each entry in the training data. The first loop of training produce a normal decision tree by minimizing the loss function. Then the training input entries are reused for checking, where the misclassified entries are then assgined higher weight for the next loop of training. Specifically for the adaptive boosting method applied in this analysis, the boost weight for the event is:

$$\alpha = \frac{1-\epsilon}{\epsilon} \tag{3.2}$$

where ϵ is the misclassified rate of the previous tree. The final output $y_{boosting}$ is the voted result of all trees with weight $\ln(\alpha)$. As shown in Eq.

3.2, h_i are discrimination outputs of each individual trees with -1 for background and +1 as signal. Comparing to normal decision tree, the BDT are better performed with weak learners i.e. the tree with less maximum depth. The performance is often improved by suppressing the learning speed by an exponential parameter β to the boosting factor as α^{β}.

$$y_{\text{boosting}}(x) = \frac{1}{N}\sum_{i}^{N} \ln(\alpha) \cdot h_i(x) \tag{3.3}$$

3.1.2 Pruning decision trees

To make the best use of ordinary decision tree method, the conditions of each decision node needs dedicated calibration, which means the strategy of loss function required global minimization of the loss. It has been found that better performance can be achieved to first grow decision trees to large depth and size, then discard those nodes with less signal–background separations (pruning). By this approach, the obvious node splittings which could lead to a early stop of tree growing or worse statistical error are avoided, allowing for a more global optimization.

3.1.3 Performance

The evaluation is achieved with the Receiver Operating Characteristic (ROC) curve. As an example in Fig. 3.2, the "curve" describe the relation between signal efficiency (the ratio of true–signal over signals) and the background rejection rate (1-background efficiency). As the quote denotes, the ROC "curve" is consists of a series of testing points varying the signal acceptance, since the mathematical formations of ROC are usually hard to find. Each point represents a working performance benchmark for a specific method, and obviously the overall performance for methods with larger area under ROC curve are better than others.

The BDT in the high energy physics is considered as one of the best signal–background classifiers. Comparing to methods with mathematical optimiza-

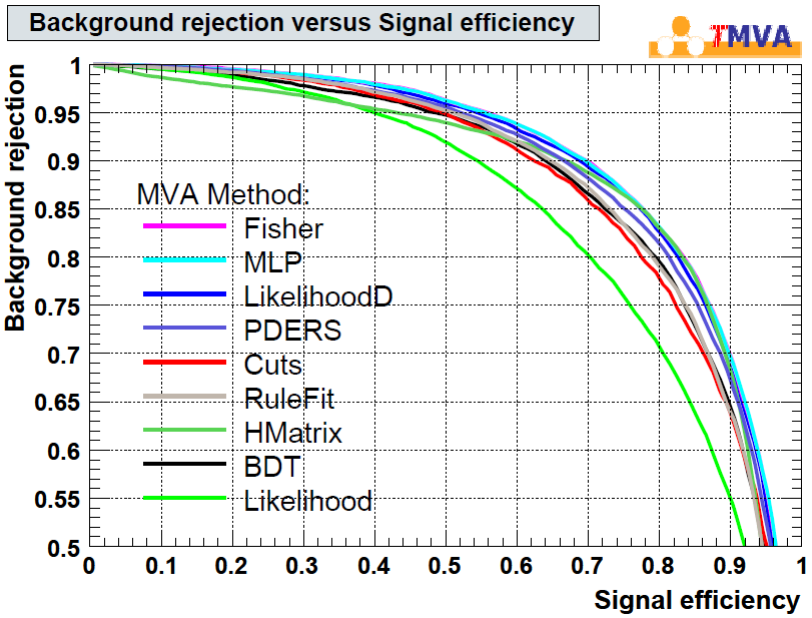

Figure 3.2: An example of ROC curves for different trained models. The integral of ROC curve represents overall performance in classification[87], which is strongly relating to the detail of training and testing data samples.

tion such as likelihood, the BDT only require little tuning to obtain reasonably good results, where each training step involves only one–dimensional cut optimization. Decision trees are also less sensitive to the input variables with poor discrimination or large fluctuations, while more complex models such as artificial neural networks and multi–layer percerptrons are typically more difficult to deal with such variables. The decision trees basically ignore non–discriminating variables as they only keep the best variable in the tree node splitting. This also lead the drawback of the BDT method, as their theoritical best performance on a given problem is generally worse than others such as neural networks.

3.2 Minimization of χ^2

The purpose for this section is to discuss a specific problem which will be encountered in the next chapter.

For two samples of data from A and B, their size are N_A and N_B separately. Now the same selection criteria ξ is applied to two samples simultaneously and the number of selected are n_A and n_B, while the expectation are $\hat{n}_A$ and $\hat{n}_B$. For this analysis, only the sum of n_A and n_B can be extracted elsewhere so that it denoted as $Y = n_A + n_B$ and its expectation $\hat{Y}$. Here the selection efficiencies for ξ are defined as:

$$\begin{aligned} \eta_A &\equiv \frac{\hat{n}_A}{N_A} \\ \eta_B &\equiv \frac{\hat{n}_B}{N_B} \end{aligned} \tag{3.4}$$

Though N_A and N_B are unknown, they are two constants as the size of two parts in the original data sample. Now the selection is repeated for different ξ referred in array form ξ_i, and Eq. 3.4 are summed and compared to its expectation in the form of vector products:

$$\boldsymbol{\eta} \times \boldsymbol{N} - \boldsymbol{Y} = \boldsymbol{\delta} \tag{3.5}$$

In Eq. 3.5, the efficiencies are formed in vectors as:

$$\begin{aligned} \boldsymbol{\eta} &= \begin{pmatrix} \eta_{1,A} & \eta_{2,A} & \cdots & \eta_{n,A} \\ \eta_{2,A} & \eta_{2,B} & \cdots & \eta_{n,B} \end{pmatrix}^{\mathrm{T}} \\ \boldsymbol{N} &= \begin{pmatrix} N_A & N_B \end{pmatrix}^{\mathrm{T}} \\ \boldsymbol{Y} &= \begin{pmatrix} Y_1 & Y_2 & \cdots & Y_n \end{pmatrix}^{\mathrm{T}} \\ \boldsymbol{\delta} &= \begin{pmatrix} \delta_1 & \delta_2 & \cdots & \delta_n \end{pmatrix}^{\mathrm{T}} \end{aligned} \tag{3.6}$$

An example of application is shown in Fig. 3.4. The array of selections are shown horizontally where the scalar products $\boldsymbol{\eta}_i \cdot \boldsymbol{N}$ is shown as the green histogram, and its components are shown in red and blue, separately. $\boldsymbol{\delta}$ are residuals of the sum $n_A + n_B$, which are also shown as the difference of black dots and the green histogram. To estimate N_A and N_B in the original data sample, a method by minimizing χ^2 is utilized. For Eq. 3.5, χ^2 is:

$$\chi^2 = \boldsymbol{\delta}^{\mathrm{T}} \boldsymbol{C}^{-1} \boldsymbol{\delta} \tag{3.7}$$

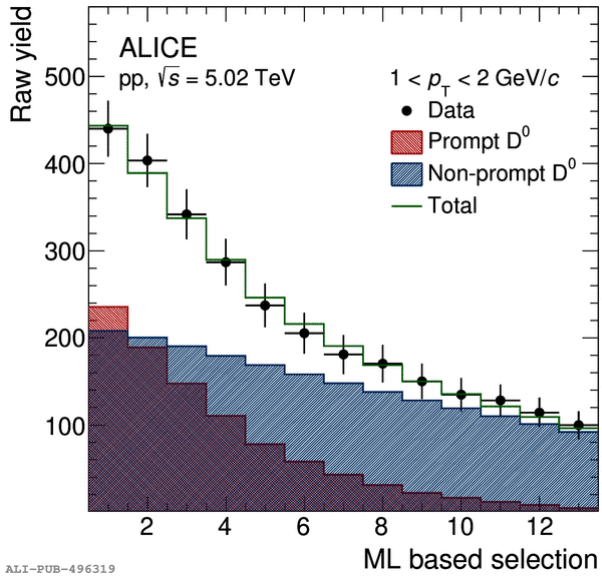

Figure 3.3: An example of min–χ^2 approach application in this work. The repeated selections are form in array and shown horizontally. The scalar products of efficiency times sample size are shown in green where two components are shown in red and blue. The difference of measurements (black solid dots) and expectations of the sum of sample size are also shown in this figure.

where $\boldsymbol{C}$ is the covariant matrix. Since the efficiencies are usually evaluated from Monte–Carlo simulations, the uncertainties for $\boldsymbol{\eta}$ are diminished and negligible. The covariant matrix of $\boldsymbol{\delta}$ then reduced to that of $\boldsymbol{Y}$, and $cov_{1,2}$ represents the covariance of Y_1 and Y_2.

$$\boldsymbol{C} = \begin{pmatrix} \sigma_1^2 & cov_{2,1} & \cdots & cov_{n,1} \\ cov_{1,2} & \sigma_2^2 & \cdots & cov_{n,2} \\ \vdots & \vdots & \ddots & \vdots \\ cov_{1,n} & \sigma_2^n & \cdots & \sigma_n^2 \end{pmatrix} \tag{3.8}$$

Practically, the minimization of χ^2 is found with numerical method and the relative checks are performed in the systematic uncertainties sections. For uncorrelated selections, the off–diagonal elements in the covariant matrix vanish. However in this work, the selections are based on BDT outputs in the form of $\text{Output}_{\text{BDT}} > x_i$. The cumulative form of the selections lead to non–trival correlation factors. The potential effects on the determination of N_A

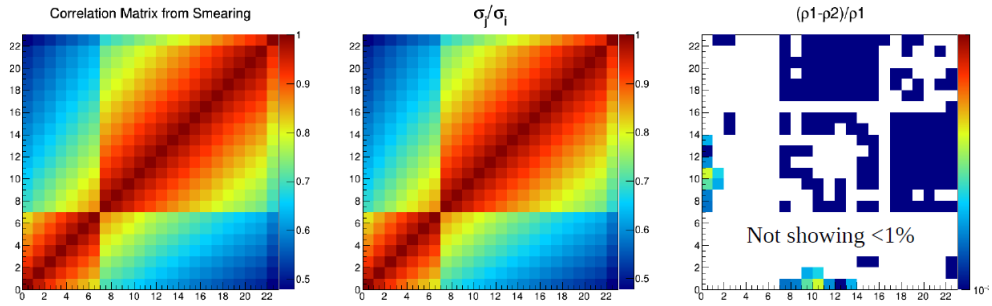

Figure 3.4: An example correlation coefficient analysis. Left: the correlation from a toy MC that utilizes Poisson smearing for the fluctuation in extracting Y. Middle: the correlation matrix from Eq. 3.9. Right: their relative difference.

and N_B are examined, where the uncertainties of them are evaluated with Pearson correlation coefficient:

$$\rho_{i,j} = \sigma_i/\sigma_j, i > j \tag{3.9}$$

In Eq. 3.9, we assume that the selections are sorted in decreasing Y_i, and thus for $i > j$, $Y_i < Y_j$. A Monte-Carlo study was performed in order to verify this correlation coefficient, which utilize Poisson smearing to the Y extraction, and the correlation from MC are calculated statistically. The correlation are compared to that of Eq. 3.9, and found consistent as shown in Fig. 3.4, for all possible combinations in the measurements mentioned in this work. Finally, Eq. 3.9 is applied to Eq. 3.8 for the calculations. For simplicity, the fraction of A in the data sample is used for calculation as:

$$Fraction = \frac{\eta_{x,A} \cdot N_A}{\eta_{x,A} \cdot N_A + \eta_{x,B} \cdot N_B} \tag{3.10}$$

.

Chapter 4

Non–prompt D^0 production in pp collisions

In this chapter, the recent measurement of D^0 production in pp collisions by ALICE was presented in details. To measure the production cross–section, hadronic decay products of D^0 are reconstructed as candidates, selected in order to enhance the signal–background ratio, and extracted with invariant–mass analysis. Then extracted signals are corrected with efficiencies obtained from Monte–Carlo simulations, and used for cross section calculations. Measured results are extrapolated to include larger transverse momentum region ($p_{\mathrm{T}} < 36$) for consistency with the measurement in Pb–Pb. Predictions with pQCD models (FONLL[41]–[43], GM–VFNS[38]–[40]) are compared to the measurement and used for analysis.

4.1 Data–sets and event selections

The result presented in this work was obtained from the data sample of pp collisions at $\sqrt{s} = 5.02$TeV collected by ALICE in 2017. The collision events used were recorded with a minimum–bias (MB) trigger which required coincident signals in the two scintillator arrays of the V0 detector. The events were further selected offline in order to remove background due to the interaction between one of the beams and the residual gas present in the beam tube and other backgrounds. This selection was based on the timing infor-

mation of the two V0 arrays and the correlation between the number of hits and track segments in the two innermost layers of the ITS, which consists of Silicon Pixel Detectors (SPD). In order to maintain a uniform acceptance in pseudorapidity, events were required to have a reconstructed collision vertex located within ±10 cm from the centre of the detector along the beam–line direction. Events with multiple primary vertices reconstructed from TPC and ITS tracks, due to the pileup of several collisions, were rejected. The rejected pileup events amount to about 1% of the triggered events and the remaining undetected pileup is negligible in the present analysis. After the event selection, the data sample used for the analysis consists of about 990 million MB events, corresponding to an integrated luminosity $\mathcal{L}_{\rm int} = (19.3 \pm 0.4)nb^{-1}$.

4.2 D^0 reconstruction

The measurement of D^0 in this analysis is performed via hadronic decay channel $D^0 \to K^-\pi^+$ along with their charge conjugates (BR = 3.947±0.030%[88]). Considering the complexity of decay topology, the target decay channel with 2 product–prongs is more accessible than other channels with 3 or more prongs such as $D^0 \to K^-\pi^+\pi^0$. Though the latter has much higher BR, the reconstruction of π^0 is involved with EMCal which introduces more uncertainties to the measurement. And the invariant mass spectra method which will be discussed later also require a simple decay channel in order to reduce the uncertainty of measurement. Thus only 2–prong decay channel $D^0 \to K^-\pi^+$ is considered in this analysis.

The reconstruction of D^0 in central rapidity region start from few hundreds micrometers ($c\tau \approx 123\mu m$) from the primary vertex where the decay begins. The start point usually located inside the ITS detector therefore the charged decay products can be recorded and reconstructed as bend tracks as shown in Fig.4.1. The 2 candidate tracks with opposite electrical charge are assumed to be K^- and π^+ for D^0. Then the secondary vertex, or the PCA (point of the closest approach) can be determined by minimizing the distance between

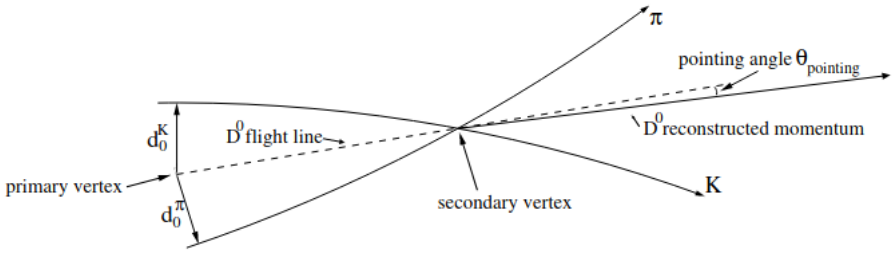

Figure 4.1: Schematic view of $D^0 \to K^-\pi^+$ decay with some of the decay topological parameters indicated. The flight line of D^0 is reconstructed by connecting the primary vertex and the reconstructed secondary vertex. And the pointing angle θ_{pointing} is between the reconstructed D^0 momentum and the flight line.

segments of 2 candidate tracks. Here the spatial precision of the track comes into the track covariant matrix, therefore PCA is closer to higher momentum tracks.

4.3 Invariant mass method

As mentioned before, the reconstructed candidates come from opposite charged tracks candidates, and therefore large proportion of combinations are 'fake' D^0. The real yield be extracted with the invariant mass of the candidates. The invariant mass spectrum of all D^0 candidates follows a Gaussian distribution plus a background function as:

$$f_(M) = \frac{P_0}{\sqrt{2\pi}P_1}\exp\left[-\frac{(M-P_2)^2}{2P_1^2}\right] + \text{bkg.func.} \tag{4.1}$$

in Eq. 4.1, P_0, P_1, P_2 are integral, central value and sigma of the Gaussian function. The background are fitted with exponential for relatively flat spectrum side-band, while for sloped background, low-order polynomial function are used for the fit. The detailed fit strategy will be mentioned in later sections. An example fit at this stage is shown in Fig. 4.2, where the yield of reconstructed D^0 candidates after selection that fulfil invariant mass condition (raw yield) can be extracted with fit parameter P_0, or:

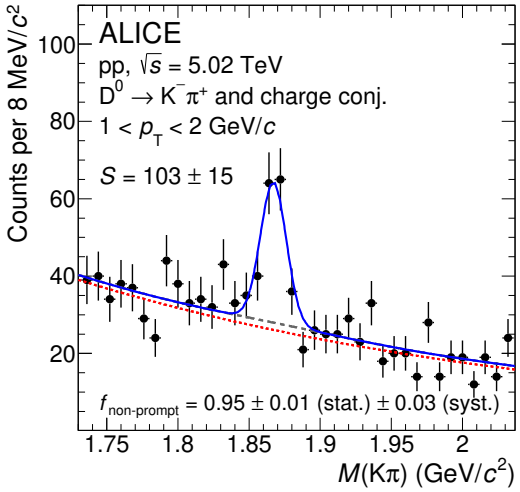

Figure 4.2: An example invariant mass fit, for non-prompt D^0 analysis at $1 < p_T < 2$ GeV/c, in pp collisions at $\sqrt{s} = 5.02$ TeV. The background function of fit consists of a 2nd–order polynomial (red) and a double-Gaussian template (grey). The extracted yield is equal to the area below blue curve and above grey dashed background.

$$\mathrm{Y} = \int f(M)dM - \int bkg(M)dM = \mathrm{N} - \mathrm{B} \tag{4.2}$$

In Eq.4.2, we denote the integral of total fit function as N and the integral of background function as B. the relative uncertainty of raw yield $\sigma_\mathrm{Y}/\mathrm{Y} = \sqrt{\frac{1}{\mathrm{N}\times\mathrm{Y}/\mathrm{B}}}$ as Y follows Poisson distribution. In order to reduce the uncertainty of measurement, the candidate selection has to be made to enhance the ratio Y/B (signal to background ratio), while keep as many candidates N as possible. For simplification, $\mathrm{Y}/\sigma_\mathrm{Y}$ is denoted as significance for the invariant mass fit, and higher significance means better precision.

4.4 Topological selections

To reduce the uncertainty of measurement, dedicated selections are needed. Additionally, the extracted raw yield contains both prompt and non–prompt components.. The latest research by ALICE group[89] suggests that the natural prompt fraction in D^0 anaylsis is $\sim 85\%$, and the uncertainty relative to

non–prompt D^0 will be amplified by one over non–prompt fraction. Therefore the selection strategy is also aim for enhance the non–prompt fraction.

The selections are based on topological parameters from D^0 decay schematic graph. For instance refering to Fig.4.1, several parameters are introduced below:

$|d_{0,\kappa}|$, $|d_{0,\pi}|$: Impact parameter, the distance of the closest approach from candidate tracks to the primary vertex. The opposite sign leads to negative products which rejects unphysical combinations, therefore $d_{0,\kappa} \times d_{0,\pi}$ is also considered.

Norm L_{XY} : The decay length L of D^0 projected to the cross section plane. This distance comes from the primary vertex to the secondary vertex, which normalized by the uncertainty.

$cos(\theta_{pointing})$: the angle $\theta_{pointing}$ is defined from D^0 flight line to reconstructed D^0 momentum. For the signals, they should centralized near $cos(\theta_{pointing}) = 1$.

$|d_0 - d_0^{exp}|(n\sigma)$: an improvised topological variable. The expected impact parameter is $d_0^{exp} \approx L_{XY} \cdot sin(\theta_{XY})$, and he difference to the measured impacted parameter is then normalized by their total uncertainty.

DCA (distance of the closest approach) : The closest distance between two tracks. This distance differs due to the spatial resolution of trajectory.

$cos(\theta^*)$: the angle θ^* is defined from D^0 flight line to the π candidate p_T.

These parameters are introduced to trained machine–learning model BDT as input. There are 2 types of models are trained for different purposes:

1. Trained with MC non–prompt D^0 as signal and prompt D^0 as background.

p_{T} bin (GeV/c)	BDT1 cut	BDT2 cut
$1.0 - 2.0$	0.17	0.10
$2.0 - 3.0$	0.15	0.07
$3.0 - 4.0$	0.13	0.07
$4.0 - 5.0$	0.11	0.07
$5.0 - 6.0$	0.10	0.07
$6.0 - 7.0$	0.10	0.09
$7.0 - 8.0$	0.09	0.09
$8.0 - 10.0$	0.08	0.09
$10.0 - 12.0$	0.05	0.10
$12.0 - 16.0$	0.04	0.10
$16.0 - 24.0$	0.03	0.10

Table 4.1: Selection criteria to the BDT response for this analysis. As the output from BDT is normalized to $[-1, 1]$, and larger output suggests signal–like event, the number of cut x represents for response $> x$.

These models are dedicated to enhancing the non–prompt fraction.

2. Trained with MC non–prompt D^0 as signal, and the candidates from the sideband of invariant mass spectrum as background. These models are dedicated to enhance the fit significance.

The 2 types of BDT are applied to reconstructed candidates simultaneously. As introduced in last chapter, the cumulative possibility for signal–like candidates increase as higher BDT output cut was applied. A balanced cut are choosed for each p_{T} bin in order to extract raw yield with high non–prompt fraction and the fit significance at same time. The detailed cut are listed in Tab.4.1.

4.5 Particle identification

The application combining both the TPC and TOF detectors provides additional background rejection especially for low–p_{T} region. The technique Particle Identification (PID) is applied for basic particle tracks such as $\pi^{\pm}$, $K^{\pm}$, p, by comparing the deposited energy in the TPC and flight–time in the TOF to the expectations. In this analysis, the conservative 3σ cuts are applied.

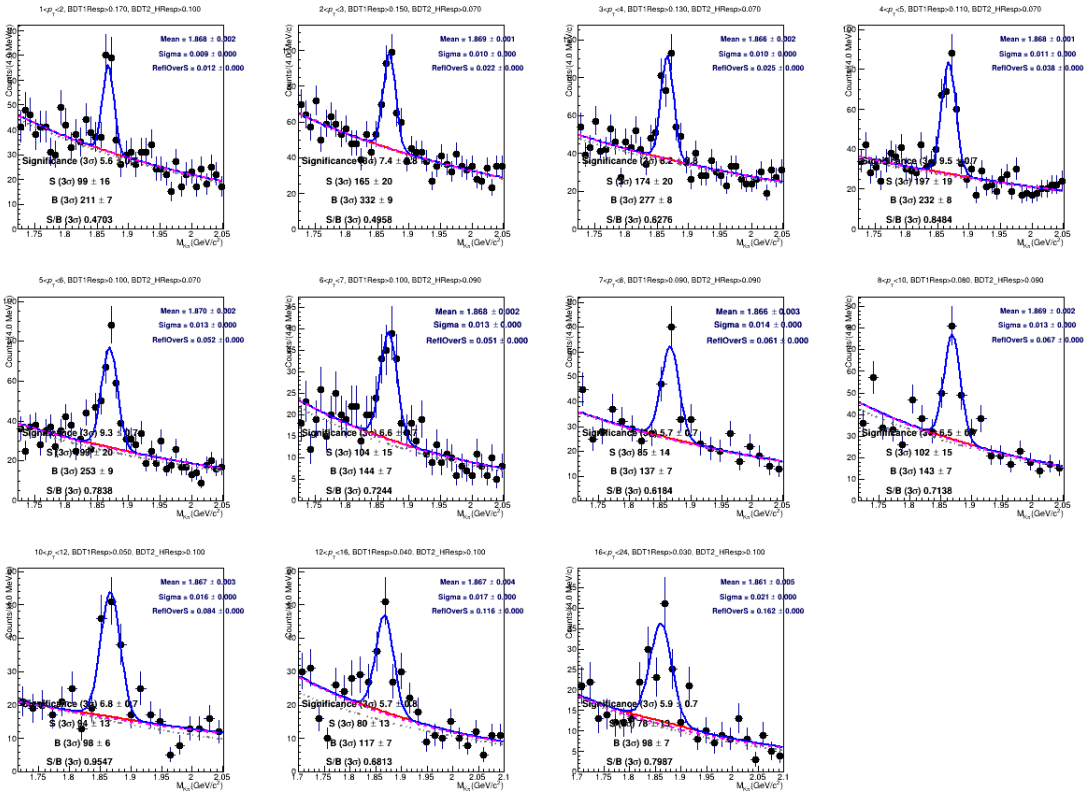

Figure 4.3: Invariant mass fit plots with background plus reflection in $1 < p_{\mathrm{T}} < 24$ GeV/c for pp collisions at $\sqrt{s} = 5.02$ TeV.

4.6 Corrections

After the selection mentioned above, the invariant mass fit for each p_{T} bin are shown in Fig. 4.3:

4.6.1 'Reflected' signal

As the reconstruction includes both $\mathrm{D}^0 \to \mathrm{K}^-\pi^+$ and $\overline{\mathrm{D}}{}^0 \to \mathrm{K}^+\pi^-$, the mass assumption applied to correlated track pairs leads to signals in invariant mass spectrum, but also to a proportion of distorted peak? which cannot be described by background function. For instance, a $K^+\pi^-$ pair from $\overline{\mathrm{D}}{}^0$ decay reconstructed with mass assumption of $\mathrm{D}^0 \to \mathrm{K}^-\pi^+$ (M(K^-) for negative tracks and M(π^+) for positive tracks) will not present the correct invariant

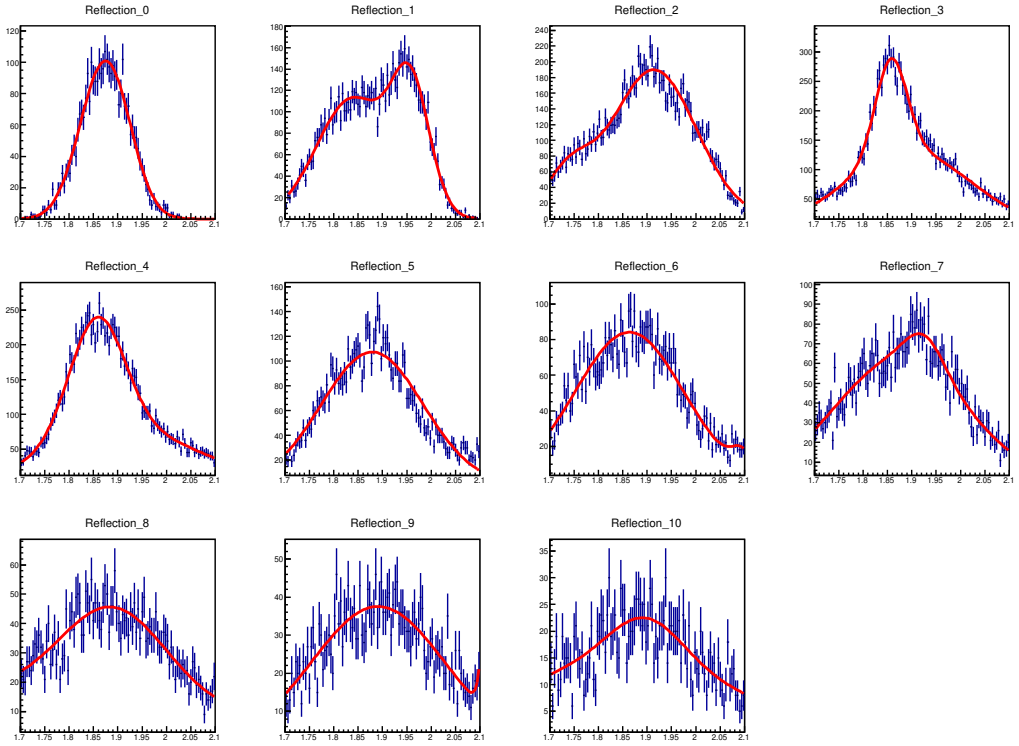

Figure 4.4: The distributions of 'reflected' D^0 for each p_T bin from the Monte Carlo simulation (blue), parameterized with the double Gaussian function (red) as templates. The templates are scaled by the relative ratios of real and 'reflected' D^0 predicted by Monte–Carlo simulation, and applied to the invariant mass fit.

mass of $\overline{D}{}^0$, but distorted to much larger width. The distribution profile and the proportion are estimated by MC shown in Fig.4.4. The template of the 'reflected' signal is fit with double–Gaussian function, and then added into the invariant mass fit background function with the relative ratio to signal fixed to the estimation from Monte–Carlo simulations.

4.6.2 Reconstruction and selection efficiency

The correction factors that cover both measurement acceptance and selection efficiency (Acc $\times \epsilon$) were evaluated with Monte Carlo simulations. The acceptance part, which corrects D^0 yield of measurement within fiducial acceptance

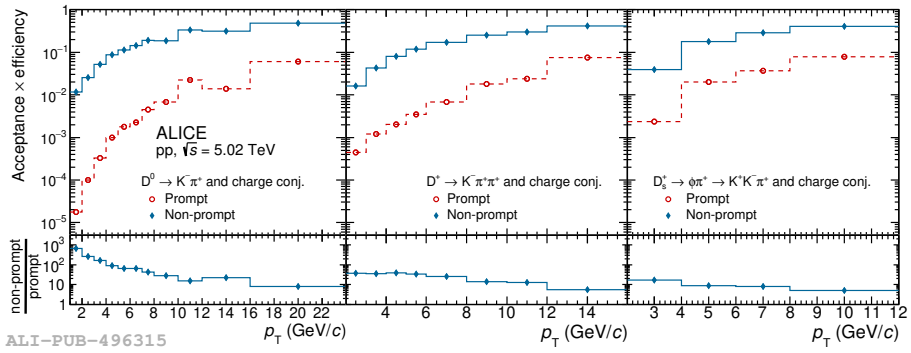

Figure 4.5: Acc × ϵ for non–prompt (blue) and prompt (red) D^0 (left), D^+ (middle), D_s^+ (right) as a function of p_T in this analysis. Ratios of non–prompt over prompt are illustrated in lower panels, which are up to 10^3 for D^0 and $10 \sim 10^2$ for D^+ and D_s^+.

coverage to mid–rapidity ($|y| < 0.5$), was determined with a toy generator based on PYTHIA[90], [91] for decay kinematics. The selection efficiency that correct raw yield after vertexing, PID, and topological selections, was studied with dedicated simulations.

$$\text{Acc} \times \epsilon \equiv \frac{N_{\text{selected}}}{N_{\text{produced},|y|<0.5}} = \frac{N_{\text{fiducial}}}{N_{\text{produced},|y|<0.5}} \times \frac{N_{\text{raw}}}{N_{\text{fiducial}}} \tag{4.3}$$

The toy MC for the acceptance part uses $D^0 \to K^-\pi^+$ decay kinematic to determine whether the tracks are inside the fiducial acceptance or not. Meanwhile for the efficiency part, PYTHIA8 generator are utilized for the MC simulation. The bias introduced with specific generator can be reduced by re–weighing MC events with proper p_T distribution, and the related uncertainties will be discussed. Also the simulations are set to enrich the heavy flavour production rate instead of the reality, in order to gain enough statistics especially for high–p_T regions. The (Acc × ϵ) over transverse momentum p_T for prompt and non–prompt D^0 are shown in Fig. 4.5.

As shown in Fig. 4.5, the (Acc × ϵ) were presented in upper panels for non–prompt and prompt D mesons, and the relative ratio of non–prompt over prompt were shown in the lower panels. The acceptance times efficiency increases with p_T, from $\sim 10^{-2}$ to ~ 0.7 for non–prompt D^0, while for prompt

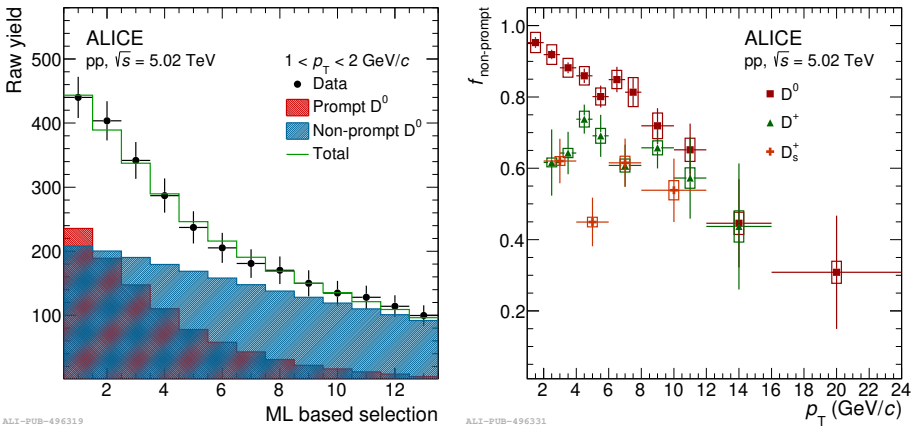

Figure 4.6: An example of raw yield distribution versus BDT selection cut (left), where the minimizing of χ^2 was applied. The determination of $f_{\text{non-prompt}}$ of D^0 is by calculating the area of blue bar (non–prompt) divided by the area below the green histogram (inclusive). And the extracted $f_{\text{non-prompt}}$ are presented in the panel (right) for D^0, D^+, and D_s^+.

D^0 the efficiencies are much lower. This effect of distinguishing was also presented in lower panels where the relative ratio of non–prompt/prompt varies from $\sim$ 10–10^3. With selections applied, the fraction of non–prompt D meson in the raw yield will be enhanced significantly, as the most of non–prompt candidates were kept.

4.6.3 Non–prompt fraction

As discussed in chapter 3, the fraction of non–prompt $f_{\text{non-prompt}}$ in raw yield can be determined with min $-\ \chi^2$ method with multiple sets of BDT cuts.

With all the mentioned correction above applied, the p_T–differential cross section of non–prompt D^0 was:

$$\frac{\mathrm{d}^2\sigma_{\text{non-prompt}}}{\mathrm{d}p_\mathrm{T}dy} = \frac{1}{c_{\Delta y}\Delta p_\mathrm{T}} \frac{1/2}{\Gamma_{\mathrm{D}^0\to\mathrm{K}^-\pi^+}} \frac{f_{\text{non-prompt}}(p_\mathrm{T})\cdot N_{raw}(p_\mathrm{T})}{(\mathrm{Acc}\times\epsilon)^{\text{non-prompt}}(p_\mathrm{T})} \frac{1}{L_{int}} \tag{4.4}$$

The raw yield sums both D^0 and $\overline{\mathrm{D}}{}^0$, then corrected with non–prompt fraction $f_{\text{non-prompt}}$ for only B–meson decay contributions, divided by $(\mathrm{Acc}\times\epsilon)^{\text{non-prompt}}$ the acceptance and efficiency for non–prompt D^0. The factor 1/2 comes

from taking average of D^0 and $\overline{D}^0$ yields. $\Gamma_{D^0\to K^-\pi^+}$ is the $D^0 \to K^-\pi^+$ branching ratio[92]. $c_{\Delta y}$ is the rapidity coverage which equals to unity since the measurement was performed in $|y| < 0.5$. The integrated luminosity $L_{int} = N_{events}/\sigma_{MB}$ is defined by normalizing numbers of collision events N_{events} to the min-bias triggered standard $\sigma_{MB} = (51.2 \pm 2.6)$ mb[93].

4.7 Systematic uncertainties

The systematic uncertainties were evaluated with following sources: (i).raw yield extraction from invariant mass spectra; (ii).track reconstruction efficiency; (iii).selection efficiency; (iv).PID efficiency; (v).D^0-meson p_T shape of MC simulations; (vi).determination of non–prompt fraction.

4.7.1 Raw yield extraction

As the raw yield extraction of D^0-mesons comes from fitting procedure on invariant mass spectra, the detail setting may introduce potential uncertainties to the measurement. The uncertainties are studied by repeating the mass–fitting with certain variations to the settings such as fit functions or fit parameters. The reflections are subtracted from the extracted yield.

The repeating procedure of invariant mass fit, or 'multi–trial' as named , works by applying a small variation to one single fit setting at a time. The variation includes: (i). upper and lower limits of the mass range. (ii). background functions. (iii). fit parameter σ. Apart from these variations, the condition of convergence are required that $\chi^2/ndf < 2$ which rejects diverse fits from systematic uncertainty evaluation. Additionally, a bin–counting method are also applied in comparison to the invariant mass fit, which utilize the original spectra histogram instead of fit function. An example of multi–trial check is shown in Fig. 4.7.

The uncertainties are assigned considering the following statistical parameters:

- convergence of the fit parameters such as mean and σ

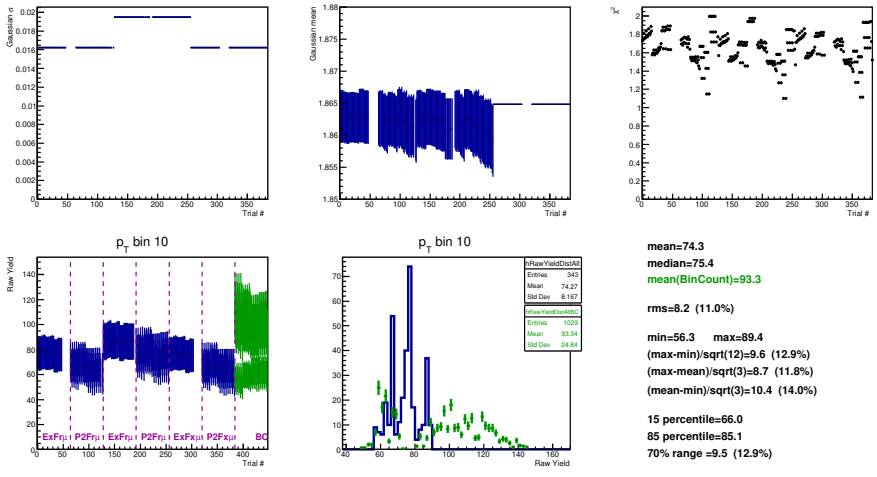

Figure 4.7: The evaluation of systematic uncertainties within the raw yield extraction process, by a multi–trial approach for $12 < p_{\mathrm{T}} < 16$ GeV/c.

- comparison between fit and bin–counting method
- r.m.s. of the raw yield distribution
- maximum - minimum divided by $\sqrt{12}$

4.7.2 Selection efficiency

Another source of systematic uncertainties originated from the signal selection procedure. The natural differences between MC and data could lead to divergence to the efficiency evaluation, and such potential bias need to be checked and covered within uncertainty ranges. Apart from BDT–based selection, the loose cuts are applied where potential bias introduced is considered negligible. As for the BDT selection efficiency, the analysis of systematic uncertainty is based on variation of selection cuts. About 50 variations of BDT selection cut combinations were tested where the efficiencies for prompt and non–prompt D^0 $\epsilon_{\mathrm{prompt}}$, $\epsilon_{\mathrm{non-prompt}}$ varies non–coherently. The variations are shown in Fig. 4.8.

To estimate the systematic uncertainty, the profile of the histograms were analyzed with a Gaussian–fit where the Gaussian σ, the RMS of the histogram,

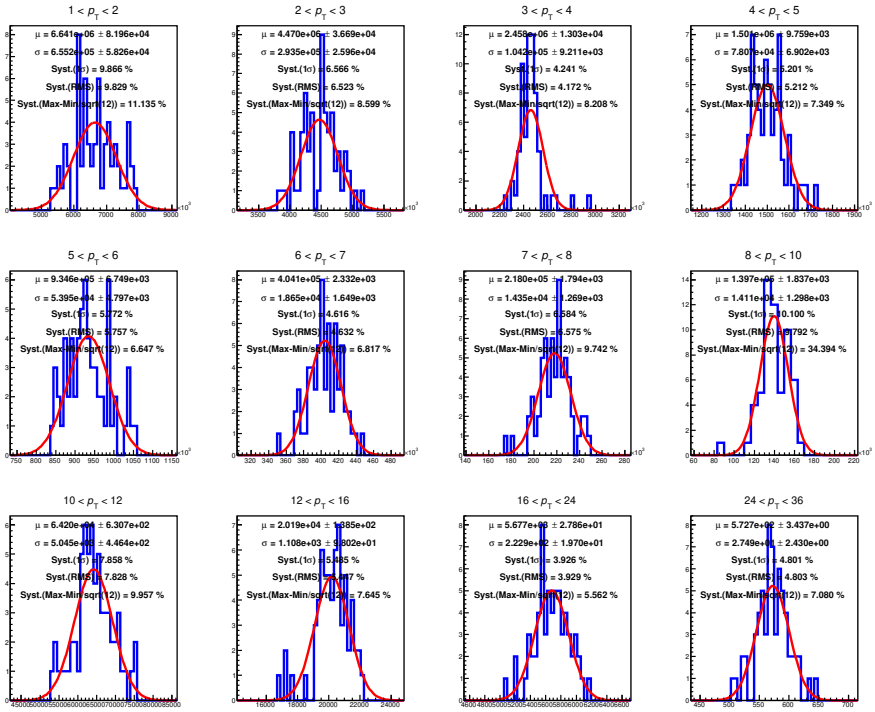

Figure 4.8: The evaluation of systematic uncertainties due to the selection efficiency. The selection cuts were varied for higher or lower efficiencies and the variations of corrected yield are summarized in the histograms.

and the $|\max - \min|/\sqrt{12}$ were evaluated.

4.7.3 p_{T} shape of the generated MC

The different p_{T} shape of generated MC sample could also be a source of systematic uncertainties. As mentioned, the dedicated settings of Monte–Carlo generator enriched production rate for heavy quarks, especially for high-p_{T} regions, to produce enough statistics and reduce fluctuations. As result, the generated p_{T} shapes are significantly harder than data. The potential bias could be reduced by re–weighing MC with the p_{T} shape ratio of FONLL[41]–[43] over MC. The uncertainty are evaluated with alternative re–weighing factors:

- the original PYTHIA8[90], [91] generated p_{T} shape over Monte–Carlo.

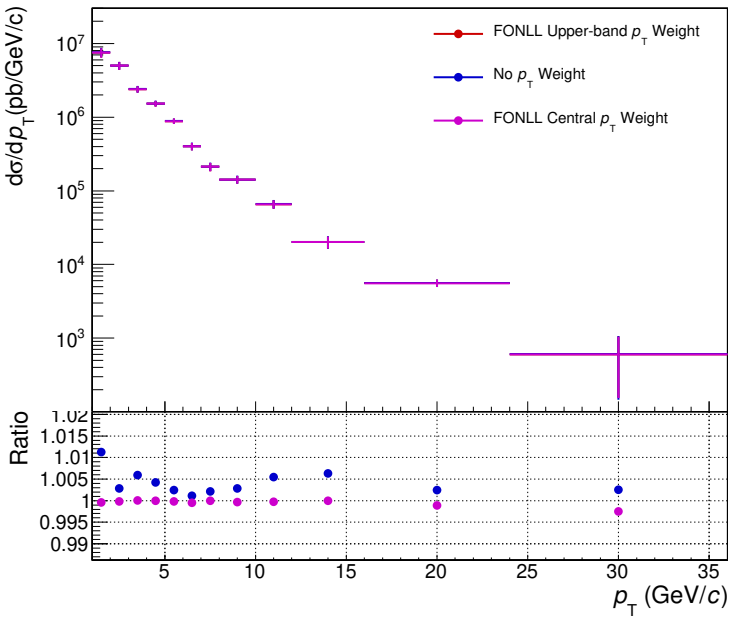

Figure 4.9: Evaluation on systematic uncertainties due to the p_{T} shape of generated MC. The calculated cross sections are shown for different p_{T} shape choices, and their respective ratio to the central value (upper prediction limit of FONLL) are shown in the lower panel.

- Instead of the upper prediction limit of the FONLL, the central prediction of FONLL over MC was applied

The comparison is shown in Fig. 4.9, where the ratio of variations over central value of the measurement is plotted in lower panel. And the uncertainties are assigned according to the ratio of different settings of re–weighing. Except for $p_{\mathrm{T}} < 2$ GeV/c, the observed deviations are consider negligible ($< 1\%$). Only for the first p_{T} bin $1 < p_{\mathrm{T}} < 2$ GeV/c, the potential variation may exist up to 1%. Therefore the systematic uncertainty due to the p_{T}–shape correction of MC was assigned only for $1 < p_{\mathrm{T}} < 2$ GeV/c at 1%.

4.7.4 Tracking efficiency

One possible source of systematic uncertainty originated from the decay products tracking propagated to D meson reconstruction arises from track–finding

in the TPC, the triggered tracking in ITS, and with different tracking quality selections. Several tests were tried in order to evaluate the uncertainty: i). use different track–selection cuts in tracking process, ii). compare the TPC–ITS track matching efficiencies[89], [93], [94] in data and MC simulations.

4.7.5 Non–prompt fraction

In order to estimate the systematic uncertainties from $f_{\text{non-prompt}}$ calculation, the cut sets for min–χ^2 approach are partially excluded. And also the density of cut sets are reduced by excluding 1 cut every 2 cuts(and 4 cuts) as shown in Fig.4.10. The comparisons are made checking the relative ratio of the extracted $f_{\text{non-prompt}}$, which are shown in Fig.4.11:

From the Fig.4.11, it shows good convergence especially at low p_{T} ($p_{\mathrm{T}} <$ 7GeV/c). Meanwhile at high p_{T} the differences increase to approximately 10%, which are mainly due to the statistical fluctuations. Finally the assigned systematic uncertainties are listed in Tab.4.2 as summary:

4.8 Results

The measured p_{T} differential cross section for non–prompt D^0 mesons in $|\mathrm{y}| < 0.5$ in pp collisions at $\sqrt{s} = 5.02$ TeV is shown in Fig.4.13 in blue, where the measured prompt D^0 in the previous publication[89] is presented simultaneously in comparison.

Within the measured transverse momentum range $1 < p_{\mathrm{T}} < 24$ GeV/c, the ratio of the p_{T}–differential cross section of non–prompt and prompt D^0 was shown in Fig. 4.12, and compared to other D mesons. The uncertainties assigned to each ratio were computed for statistical and systematical independently. For statistical uncertainty, the correlation between non–prompt and prompt measurements was considered as negligible, since the fraction of D–meson candidates reconstructed and shared in two measurements is small. And for systematic certainty, the parts concerning to the tracking efficiency and to the luminosity are propagated as correlated, while for other sources

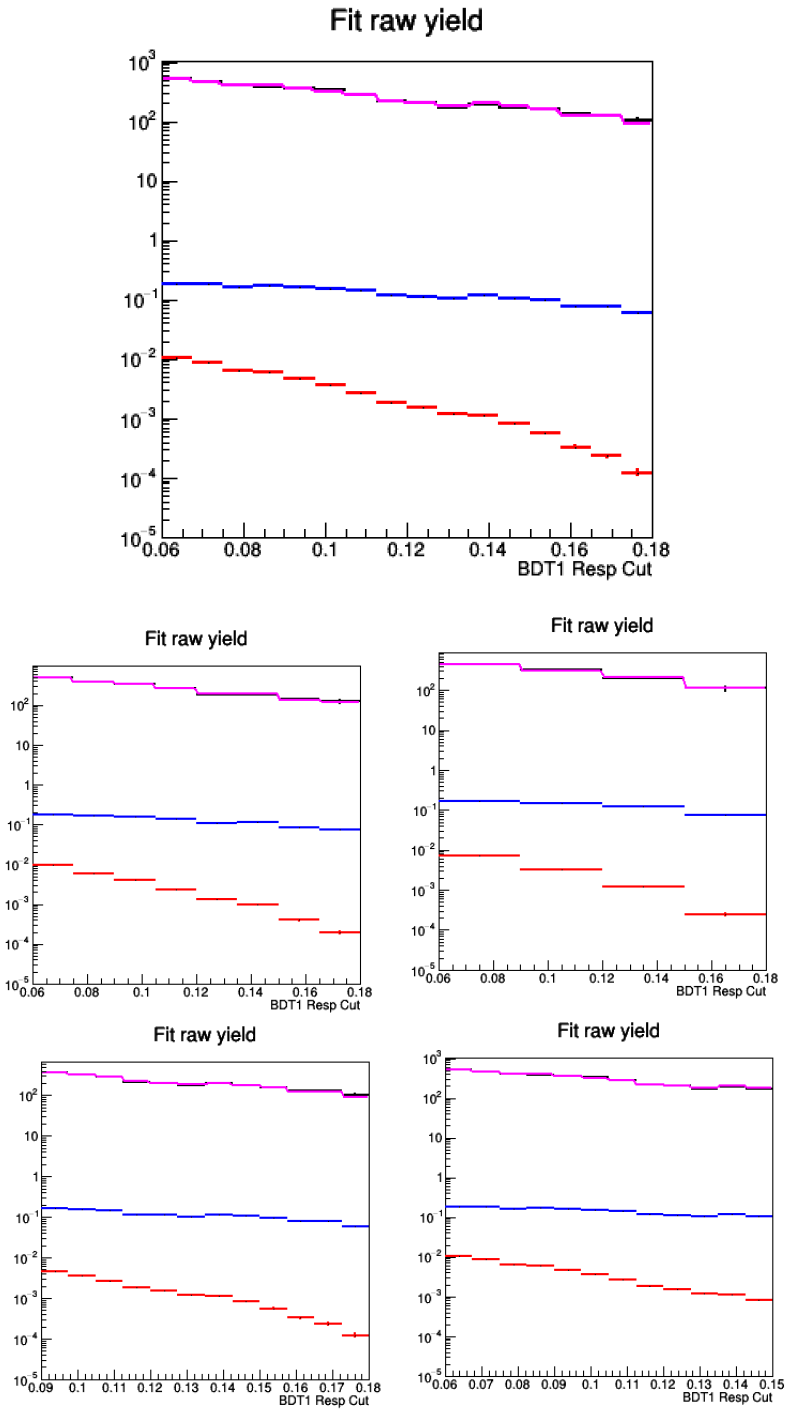

Figure 4.10: Evaluation of systematic uncertainties within the minimizing χ^2 approach to extract the non–prompt fraction. The variations of the approach are shown in the lower 2×2 panels where the re-binning for every 2 bins (top left) and 4 bins (top right), the excluding of the 2 most loose bins (lower left) and tight bins (lower right) are shown.

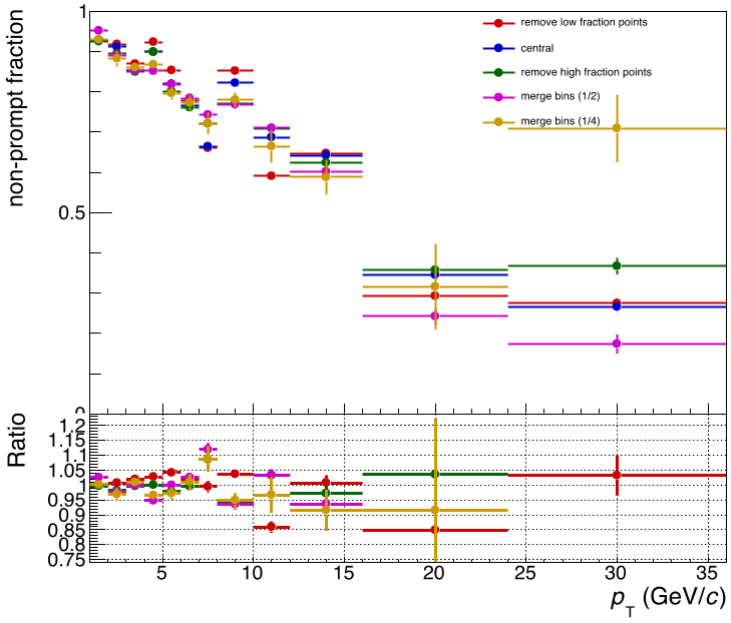

Figure 4.11: Evaluation of systematic uncertainties within the minimizing χ^2 approach to extract the non–prompt fraction. The extracted non–prompt fraction for different variations are shown in the upper panel and their respective ratio to the central value are shown in the lower panel.

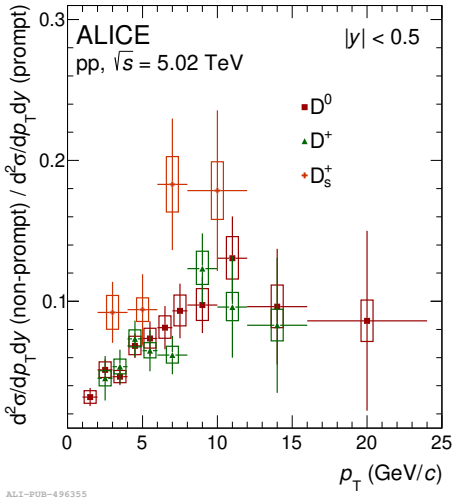

Figure 4.12: The ratio of p_{T}–differential production cross sections of non–prompt over prompt D mesons. The systematic uncertainties are shown as boxes, and the statistical uncertainties are shown as vertical bars.

p_{T} bin (GeV/c)	$1-2$	$2-3$	$3-4$	$4-5$	$5-6$	$6-7$
Yield extr. (%)	5%	5%	5%	5%	5%	5%
Selection eff.	10%	6%	5%	5%	5%	5%
p_{T} shape	1%	0%				
Tracking eff.	3%					
$f_{\text{non-prompt}}$	3%	3%	3%	3%	3%	3%
PID eff.	0%					
Branching ratio	1%					
$\mathcal{L}_{\text{int}}$	2.1%					
Total (w/o BR, $\mathcal{L}_{\text{int}}$)	12%	8.9%	8.2%	8.2%	8.2%	8.2%

p_{T} bin (GeV/c)	$7-8$	$8-10$	$10-12$	$12-16$	$16-24$
Yield extr. (%)	7%	7%	7%	11%	11%
Selection eff.	5%	5%	5%	5%	5%
p_{T} shape	0%				
Tracking eff.	3%				
$f_{\text{non-prompt}}$	5%	5%	5%	7%	10%
PID eff.	0%				
Branching ratio	1%				
$\mathcal{L}_{\text{int}}$	2.1%				
Total (w/o BR, $\mathcal{L}_{\text{int}}$)	10.4%	10.4%	10.4%	14.3%	16.0%

Table 4.2: summary table of systematic uncertainties for the measured production cross section of non–prompt D^0 in pp collisions at $\sqrt{s} = 5.02$ TeV.

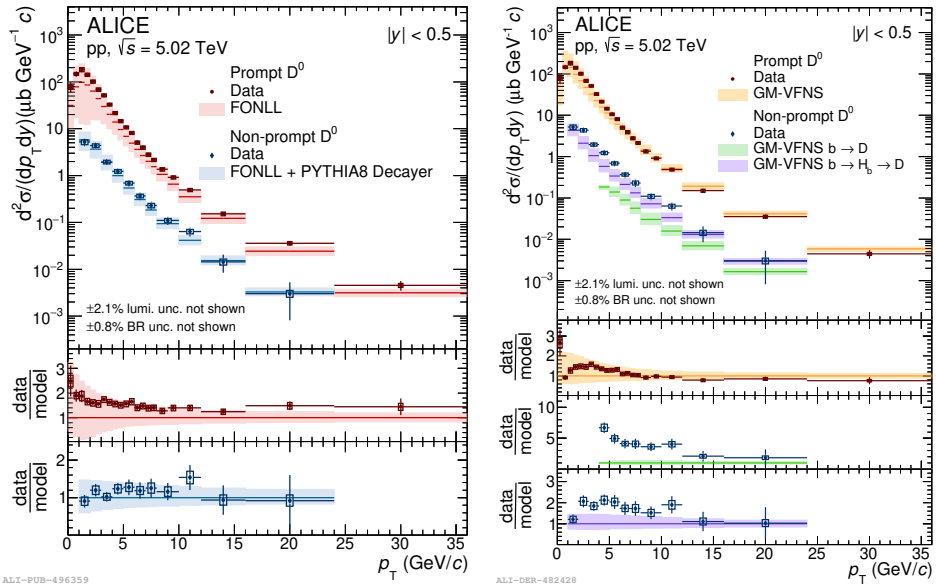

Figure 4.13: p_{T}–differential cross sections of prompt (red) and non–prompt (blue) D^0 meson compared to obtained prediction with FONLL calculations[41]–[43] combined with PYTHIA8[90], [91] for decay kinematics of non–prompt productions (left panel), and the prediction with GM-VFNS calculations[38]–[40] (right panel), where for non–prompt D^0 the one–step approach (green) and two–step approach (purple) are presented simultaneously. The measurement of prompt D^0 meson is reported in Ref.[89].

of systematic uncertainties were considered as uncorrelated between the measurements of non–prompt and prompt D–mesons. The ratios show increasing trends with $p_{\rm T}$ for $\rm D^0$, $\rm D^+$, and $\rm D_s^+$ up to $p_{\rm T} = 12$ GeV/c, as expected due to the harder $p_{\rm T}$ distribution of beauty hadrons ($\rm H_b$) compared to D mesons. The ratio for $\rm D^0$ and $\rm D^+$ mesons are compatible within uncertainties, while for the $\rm D_s^+$ mesons the central points are systematically higher compared to other two. This suggests a larger contribution of beauty–hadron decays to $\rm D_s^+$ compared to non–strange D mesons, but at given uncertainties the conclusion is not solid.

Meanwhile in Fig 4.13, the $p_{\rm T}$–differential cross sections of $\rm D^0$ meson is compared to predictions obtained with FONLL[41]–[43] and GM–VFNS[38]–[40] pQCD calculations. The FONLL uncertainty band includes the uncertainties due to the choice of the renomalization (μ_R) and factorization (μ_F) scales and of the charm and beauty quark masses, as well as the uncertainties on the CTEQ6.6 PDFs[95]. In GM–VFNS, the uncertainty related to the choice of the scales is estimated by varying only μ_R and the CTEQ14 PDFs[96] are employed. Within the FONLL framework, the fragmentation fractions $f(c \to D)$ from Ref.[97] were used to normalise the prompt $\rm D^0$ cross section. While for non–prompt $\rm D^0$, the FONLL calculations for beauty–hadron $\rm H_b$ cross section were used together with PYTHIA 8[90], [91] for the description of $\rm H_b \to D + X$ decay kinematics and branching ratios. The contributions from the different beauty–hadron species were weighted according to fragmentation fractions of b quarks into beauty–hadron species $f(b \to \rm H_b)$ measured in the $Z \to b\bar{b}$ reported in Tab. 4.3, which provide a good normalization for B–meson measurements performed by the ATLAS, LHCb, and CMS Collaborations[98]–[100]. Two different approaches are instead considered in the GM–VFNS framework. In the first one, the transition from the beauty quark to the charm hadron is described in a single step, exploiting a set of fragmentation functions for $\rm b \to D + X$ obtained from measurements in $\rm e^+e^-$ collisions as described in Ref.[101], [102]. In the second approach[40], the $\rm b \to D + X$ transition is treated in two separate steps, consisting of the $\rm b \to H_b$ fragmentation and

b–hadron	Fraction at Z (%)	Fraction at $p\bar{p}$%
B^0, B^+	40.8 ± 0.7	34.4 ± 2.1
B_s^0	10.0 ± 0.8	11.5 ± 1.3
Λ_b^0	8.4 ± 1.1	19.8 ± 4.6

Table 4.3: Fragmentation fractions of b–quarks into hadron species in $Z \to b\bar{b}$ decays, in $p\bar{p}$ collisions at $\sqrt{s} = 1.96$ TeV[88].

the $H_b \to D + X$ decay, similarly to what was performed in the FONLL + PYTHIA 8 calculation.

The measured p_T–differential cross section for D^0 meson is described within uncertainties by the FONLL and GM–VFNS predictions. In the case for FONLL, the data lie on the upper edge of the theory uncertainty band, while for the GM–VFNS calculation, the central values of the prediction tend to underestimate the data at low and intermediate p_T and is to overestimate them at high p_T. The measured non–prompt D^0 cross section is instead in better agreement with the central values of FONLL + PYTHIA 8 predictions, while it is underestimated by the GM–VFNS calculations. In the case of the one–step approach, the predictions are lower than the data by a factor about 2 to 7 depending on the transverse momentum. The two–step approach describes better the non–prompt D^0 cross section measurements, nevertheless it still underestimates the measured by a factor between 1.5 to 2. This confirms that all the different terms of the factorisation approach play a crucial role in the description of the heavy–flavour hadron cross sections, indicating the importance of setting stronger constraints on the fragmentation and decay kinematics.

In Tab.4.4, the 'visible' cross sections of non–prompt D^0 cross section, i.e. the integral of $d\sigma/dp_T$ over measured transverse momentum range $1 < p_T < 24$ GeV/c was presented together with other D–meson species. In the integrated cross sections, the systematic uncertainties were propagated as fully correlated among the measured p_T intervals, except for the part

Meson	$p_{\rm T}$ range (GeV/c)	Visible cross section (μb)
Non–prompt		
$\rm D^0$	$1 < p_{\rm T} < 24$	$14.5 \pm 1.2(\text{stat.}) \pm 1.3(\text{syst.}) \pm 0.3(\text{lumi.}) \pm 0.1(\text{BR})$
$\rm D^+$	$2 < p_{\rm T} < 16$	$4.1 \pm 0.7(\text{stat.}) \pm 0.4(\text{syst.}) \pm 0.1(\text{lumi.}) \pm 0.1(\text{BR})$
$\rm D_s^+$	$2 < p_{\rm T} < 12$	$3.4 \pm 0.6(\text{stat.}) \pm 0.3(\text{syst.}) \pm 0.1(\text{lumi.}) \pm 0.1(\text{BR})$
Prompt		
$\rm D^0$	$0 < p_{\rm T} < 36$	$440 \pm 19(\text{stat.}) \pm 29(\text{syst.}) \pm 9(\text{lumi.}) \pm 3(\text{BR})$
$\rm D^+$	$0 < p_{\rm T} < 36$	$194 \pm 23(\text{stat.}) \pm 16(\text{syst.}) \pm 4(\text{lumi.}) \pm 3(\text{BR})$
$\rm D_s^+$	$1 < p_{\rm T} < 24$	$64 \pm 9(\text{stat.})^{+6}_{-7}(\text{syst.}) \pm 1(\text{lumi.}) \pm 2(\text{BR})$

Table 4.4: Measured $p_{\rm T}$–integrated production cross sections for non–prompt and prompt D mesons at center rapidity $|\rm y| < 0.5$ in pp collisions at $\sqrt{s} =$ 5.02 TeV.

due to the raw yield extraction, which was treated as uncorrelated considering the variations of the signal–to–background ratio and the shape of the combinatorial–background distribution as a function of $p_{\rm T}$.

In order to bring the measurement towards the integrated cross section for $p_{\rm T} > 0$, the extrapolations were applied to the measured transverse momentum range. A factor of extrapolated cross section over visible was determined with the FONLL predictions for the beauty–hadron production and PYTHIA 8 to describe the $\rm H_b \to D + X$ decay kinematics. The uncertainties of the extrapolation were evaluated considering the uncertainty of FONLL, the uncertainty of beauty fragmentation fraction $f(\rm b \to H_b)$, and the uncertainty of branching ratio of the $\rm H_b \to D + X$ decays. For the beauty fragmentation fraction, an alternative set measured in p collisions[88] presented in Tab.4.3 was considered, while for the branching ratios an reweighing method was applied to the implemented BR in PYTHIA 8 in order to reproduce the measured value in Ref.[88]. In addition, it was verified that the extrapolation factors computed with the PYTHIA 8 decayer were compatible with those resulting from the usage of the EvtGen package[103] for the description of the beauty–hadron decays. Finally, the extrapolated production cross sections for non–prompt $\rm D^0$, along with other D meson species, were reported in Tab.4.5, and the ex-

Meson	Extr. factor	$d\sigma/dy|_{|y|<0.5}(\mu b)$
Non–prompt		
D^0	$1.28^{+0.01}_{-0.04}$	$18.4 \pm 1.5(stat.) \pm 1.6(syst.) \pm 0.4(lumi.) \pm 0.1(BR)^{+0.1}_{-0.6}(extr.)$
D^+	$2.22^{+0.05}_{-0.19}$	$9.0 \pm 1.5(stat.) \pm 0.9(syst.) \pm 0.2(lumi.) \pm 0.2(BR)^{+0.2}_{-0.8}(extr.)$
D_s^+	$2.03^{+0.04}_{-0.15}$	$6.9 \pm 1.2(stat.) \pm 0.7(syst.) \pm 0.1(lumi.) \pm 0.2(BR)^{+0.1}_{-0.5}(extr.)$
Prompt		
D^0	$1.0000^{+0.0003}_{-0.0000}$	$440 \pm 19(stat.) \pm 29(syst.) \pm 9(lumi.) \pm 3(BR)$
D^+	$1.0000^{+0.0003}_{-0.0000}$	$195 \pm 23(stat.) \pm 16(syst.) \pm 4(lumi.) \pm 3(BR)$
D_s^+	$1.28^{+0.35}_{-0.12}$	$82 \pm 12(stat.) \pm 8(syst.) \pm 2(lumi.) \pm 3(BR)^{+23}_{-8}(extr.)$

Table 4.5: Production cross section of non–prompt and prompt D mesons at center rapidity $|y| < 0.5$ in pp collisions at $\sqrt{s} = 5.02$ TeV, with extrapolations.

trapolation factors were presented as well.

4.8.1 Cross section ratios

The p_T–integrated cross section were used to compute the ratios of production yield among the different D–meson species in Tab. 4.5. In the computation of these ratios, the systematic uncertainties related to the tracking efficiency and luminosity were consider as correlated among the different species. The extrapolation uncertainties were also treated as correlated, except for the source of uncertainty due to the branching ratios of beauty–hadron decays used in the extrapolation of the p_T–integrated cross section of non–prompt D mesons. All other sources of systematic uncertainties were propagated as uncorrelated. In Tab.4.6, the ratios of the non–prompt D mesons cross section were presented, and compared to the ratios of prompt D mesons. The ratios of D^+/D^0 for prompt and non–prompt D–meson production are compatible, while for the D_s^+ over non–strange D meson ratio, the measured value are higher for non–prompt than for prompt D meson production with a significance about 2.5σ. This is qualitatively expected from the $b \to c\bar{c}s$ and $\bar{b} \to c\bar{c}\bar{s}$ weak decays, which enhance D_s^+ final states. Meanwhile, this measurement of ratio is compatible with previous measurements at LEP[97].

A possible p_T dependence was investigated by analyzing the ratio of the

Non–prompt	
$\mathrm{D^+/D^0}$	$0.487 \pm 0.090(\mathrm{stat.}) \pm 0.055(\mathrm{syst.}) \pm 0.009(\mathrm{BR})^{+0.007}_{-0.027}(\mathrm{extr})$
$\mathrm{D_s^+/D^0}$	$0.375 \pm 0.071(\mathrm{stat.}) \pm 0.041(\mathrm{syst.}) \pm 0.014(\mathrm{BR})^{+0.004}_{-0.016}(\mathrm{extr})$
$\mathrm{D_s^+/D^+}$	$0.769 \pm 0.183(\mathrm{stat.}) \pm 0.086(\mathrm{syst.}) \pm 0.030(\mathrm{BR})^{+0.003}_{-0.010}(\mathrm{extr})$
$\mathrm{D_s^+/(D^0+D^+)}$	$0.252 \pm 0.047(\mathrm{stat.}) \pm 0.023(\mathrm{syst.}) \pm 0.009(\mathrm{BR})^{+0.001}_{-0.006}(\mathrm{extr})$
Prompt	
$\mathrm{D^+/D^0}$	$0.442 \pm 0.055(\mathrm{stat.}) \pm 0.033(\mathrm{syst.}) \pm 0.008(\mathrm{BR})$
$\mathrm{D_s^+/D^0}$	$0.186 \pm 0.028(\mathrm{stat.}) \pm 0.015(\mathrm{syst.}) \pm 0.007(\mathrm{BR})^{+0.051}_{-0.018}(\mathrm{extr})$
$\mathrm{D_s^+/D^+}$	$0.419 \pm 0.078(\mathrm{stat.}) \pm 0.041(\mathrm{syst.}) \pm 0.017(\mathrm{BR})^{+0.116}_{-0.040}(\mathrm{extr})$
$\mathrm{D_s^+/(D^0+D^+)}$	$0.128 \pm 0.020(\mathrm{stat.}) \pm 0.010(\mathrm{syst.}) \pm 0.005(\mathrm{BR})^{+0.035}_{-0.012}(\mathrm{extr})$

Table 4.6: Ratios of the production cross sections of non–prompt and prompt D mesons in the range $|y| < 0.5$ in pp collisions at $\sqrt{s} = 5.02$ TeV.

p_{T}–differential cross sections of $\mathrm{D^+}$ and $\mathrm{D^0}$ and the ratio between one of the $\mathrm{D_s^+}$ mesons and the non–strange mesons, which was shown in Fig. 4.14. The measured ratios show no dependence of p_{T} in the measured transverse momentum range within the current experimental precision. Also, the measured ratios are compatible with the FONLL + PYTHIA 8 for non–prompt non–strange D mesons (compatible to FONLL for prompt). In the right panel of Fig. 4.14, the contribution of $\mathrm{D_s^+}$ from $\mathrm{B_s^0}$ and non–strange B meson decays in the FONLL + PYTHIA 8 calculation are depicted separately to highlight the substantial contribution of non–prompt $\mathrm{D_s^+}$ from the decay of non–strange B mesons.

The ratio of the the fragmentation fractions are also possible for measurement. The FF of beauty quarks to beauty–strange mesons divided by the one to non–strange beauty mesons is obtained from the corresponding cross section ratio $(\frac{\mathrm{D_s^+}}{\mathrm{D^0+D^+}})_{\mathrm{non-prompt}}$. This assumed that all $\mathrm{D^{*+}}$ and $\mathrm{D^{*0}}$ mesons decay to $\mathrm{D^0}$ and $\mathrm{D^+}$ mesons, and all $\mathrm{D_s^{*+}}$ mesons decay to $\mathrm{D_s^+}$ mesons. Additionally, a correction factor was added to account for the fraction of non–prompt $\mathrm{D_s^+}$ mesons not originating from $\mathrm{B_s^0}$ decays, and for the fraction of non–prompt $\mathrm{D^0}$ and $\mathrm{D^+}$ mesons not originating from non–strange B–meson decays. This

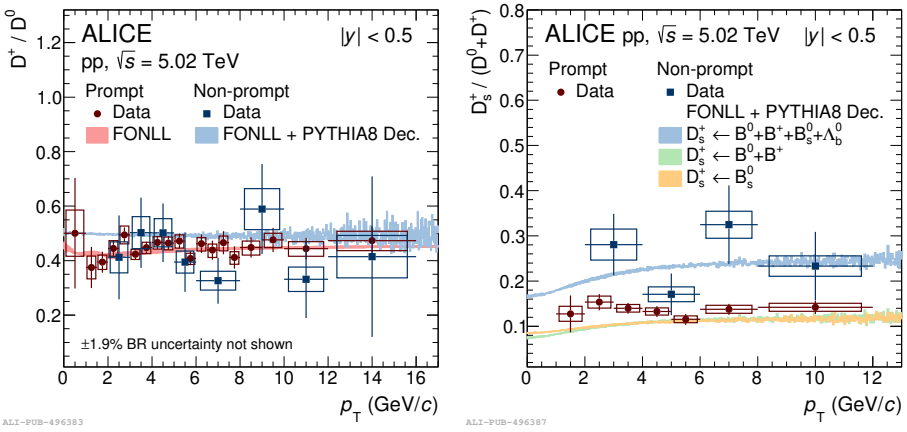

Figure 4.14: Left: the p_{T}–differential cross section of D^+ and D^0 in ratio, compared with predictions by FONLL[41]–[43] combined with PYTHIA8[90], [91] for the decay kinematics. Right: the same ratio for D_s^+ over the sum of D^0 and D^+, compared with the predictions, where the D_s^+ from B_s^0 and from non–strange B meson decays are shown simultaneously.

correction factor was computed from FONLL + PYTHIA 8 and a systematic uncertainty was assigned by varying the set of beauty fragmentation fractions and the beauty–hadron branching ratios, as described in the previous section. In the case of D_s^+ mesons, B_s^0 and non–strange B mesons are expected to contribute almost equally to the non–prompt D_s^+ cross section as shown in the right panel of Fig.4.14, while most of the non–prompt D^0 and D^+ mesons come from non–strange B–meson decays. Finally the ratio of the fragmentation fraction is calculated with:

$$\left(\frac{f_\mathrm{s}}{f_\mathrm{u}+f_\mathrm{d}}\right)_{\mathrm{beauty}} = \left[\frac{N(\mathrm{D}_\mathrm{s}^+ \leftarrow \mathrm{B}_\mathrm{s}^0)}{N(\mathrm{D}_\mathrm{s}^+ \leftarrow \mathrm{H_b})} \times \frac{N(\mathrm{D}^0, \mathrm{D}^+ \leftarrow \mathrm{H_b})}{N(\mathrm{D}^0, \mathrm{D}^+ \leftarrow \mathrm{B}^{0,+})}\right]^{\mathrm{FONLL+PYTHIA8}} \times \left(\frac{\mathrm{D}_\mathrm{s}^+}{\mathrm{D}^0+\mathrm{D}^+}\right)_{\mathrm{non-prompt}} \tag{4.5}$$

which was fitted to the measurement with a constant function, leading to the

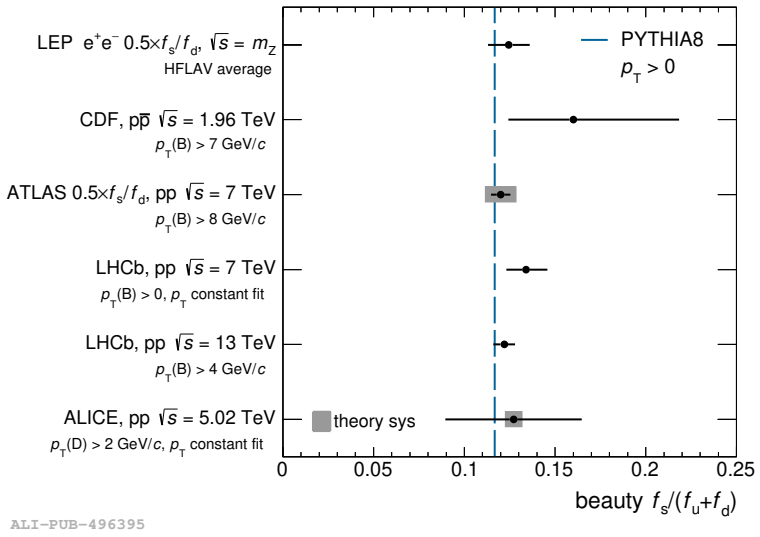

Figure 4.15: Fragmentation–ratio $f_s/(f_u + f_d)$ from non–prompt D meson measurements, compared with previous measurements performed by the CDF[104], LHCb[105], [106], ATLAS[107] Collaborations, and LEP[108] measurements. The total experimental uncertainties (horizontal bars) and the theoretical uncertainties (shaded boxes) are shown. All experimental measurements are compare to the PYTHIA8 simulations with Monash–13 tune[109].

result:

$$\left(\frac{f_{\mathrm{s}}}{f_{\mathrm{u}}+f_{\mathrm{d}}}\right)_{\mathrm{beauty}} = 0.127\pm0.036(\mathrm{stat.})\pm0.012(\mathrm{syst.})\pm0.005(\mathrm{BR})\pm0.005(\mathrm{theo.}) \tag{4.6}$$

where the theoretical uncertainty arises from the correction factor in Eq. 4.5 for the fractions of $\mathrm{D_s^+}$ ($\mathrm{D^0}$ and $\mathrm{D^+}$) mesons originating from the decay of $\mathrm{B_s^0}$ ($\mathrm{B^{0,+}}$) mesons.

The beauty–quark fragmentation fraction ratio $\frac{f_{\mathrm{s}}}{f_{\mathrm{u}}+f_{\mathrm{d}}}$ is compared with previous measurements from CDF[104], LHCb[105], [106], and ATLAS[107] Collaborations in Fig.4.15. For the measurement by ATLAS was divided by a factor of two assuming the symmetry of isospin for the u and d quarks, which implies $f_{\mathrm{u}} = f_{\mathrm{d}}$. All the FF ratios measured in pp and $\mathrm{p\overline{p}}$ collisions are compatible with the LEP average, computed by the HFLAV Collaboration[108], and the value obtained from PYTHIA 8 simulations with Monash–13

tune[109]. It is also found that the FF ratio $\frac{f_s}{f_u+f_d}$ are similar for charm and beauty sectors and are consistent with the relative ratio of light strange to non–strange particle productions in pp and e^+e^- collisions[110].

4.8.2 Beauty production cross section

The total $b\bar{b}$ production cross section at $|y| < 0.5$ was computed with a similar procedure to the one adopted to derive the p_T–integrated cross sections of non–prompt D mesons in the previous section. In this case, the factor for extrapolation is computed as:

$$\alpha_{\text{extr.}}^{b\bar{b}} = \frac{d\sigma_{b\bar{b}}/dy|_{|y|<0.5}^{\text{FONLL}}}{\sigma_{b\to D}^{\text{FONLL+PYTHIA8}}(p_T^{\text{min}} < p_T < p_T^{\text{max}}, |y| < 0.5)} \tag{4.7}$$

where $d\sigma_{b\bar{b}}/dy|_{|y|<0.5}^{\text{FONLL}}$ is the $b\bar{b}$ production cross section obtained with FONLL calculations with a correction for the different shape of the distributions of beauty hadrons and $b\bar{b}$ pairs, and $\sigma_{b\to D}^{\text{FONLL+PYTHIA8}}(p_T^{\text{min}} < p_T < p_T^{\text{max}}, |y| < 0.5)$ is the non–prompt D mesons cross section in the measured transverse momentum range from the the FONLL + PYTHIA 8 model. The correction for $b\bar{b}$ rapidity distribution is composed of two factors: i). The factor accounts for the different rapidity distributions of beauty mesons and single beauty quarks and it was evaluated to be unity in the relevant rapidity range based on FONLL calculations, where a $\sim 1\%$ uncertainty evaluated from the difference between values from FONLL and PYTHIA 8 was assigned. ii). The ratio of $\frac{d\sigma_{b\bar{b}}/dy}{d\sigma_b/dy}$ which was estimated from NLO pQCD calculations (POWHEG[111]) as $d\sigma_{b\bar{b}}^{|y|<0.5}/d\sigma_b^{|y|<0.5} = 1.06$. A 1% uncertainty on this factor was estimated from the difference among the values obtained varying the factorisation and renormalization scales in the POWHEG calculation and using different sets of PDFs (CT10NLO[112] and CT14NLO[113]). The other sources of systematic uncertainty on the extrapolation factor, i.e. FONLL, $BR(H_b \to D + X)$, and $f(b \to H_b)$, were already described in the last section for the extrapolation of the p_T–integrated production cross sections of non–prompt D mesons.

Non–prompt meson	$d\sigma_{b\bar{b}}/dy\|_{\|y\|<0.5}$
$D^0 \leftarrow b$	$33.1 \pm 2.7(\text{stat.}) \pm 2.9(\text{syst.}) \pm 0.7(\text{lumi.})$
	$\pm 0.3(\text{BR})^{+4.8}_{-0.6}(\text{extr}) \pm 0.5(\text{rapi. shape})$
$D^+ \leftarrow b$	$33.5 \pm 5.6(\text{stat.}) \pm 3.3(\text{syst.}) \pm 0.7(\text{lumi.})$
	$\pm 0.6(\text{BR})^{+13.1}_{-2.5}(\text{extr}) \pm 0.5(\text{rapi. shape})$
$D_s^+ \leftarrow b$	$40.5 \pm 6.9(\text{stat.}) \pm 3.8(\text{syst.}) \pm 0.8(\text{lumi.})$
	$\pm 1.4(\text{BR})^{+2.7}_{-3.3}(\text{extr}) \pm 0.6(\text{rapi. shape})$
$D^0, D^+, D_s^+ \leftarrow b$	$34.5 \pm 2.4(\text{stat.}) \pm 2.5(\text{syst.}) \pm 0.7(\text{lumi.})$
	$\pm 0.3(\text{BR})^{+3.8}_{-1.1}(\text{extr}) \pm 0.5(\text{rapi. shape})$

Table 4.7: $b\bar{b}$ cross section in $|y| < 0.5$ from non–prompt D^0, D^+, and D_s^+ measurements and the average. The different sources of uncertainties are listed including the extrapolations.

The $d\sigma_{b\bar{b}}/dy$ was computed separately for non–prompt D^0, D^+, and D_s^+. Then three values were averaged by weight which considers the statistical uncertainties and the uncorrelated systematic uncertainties. For the systematic uncertainties related to the tracking efficiency and the extrapolation uncertainties related to FONLL and the beauty fragmentation fractions were treated as fully correlated for three D–meson species. The resulted $b\bar{b}$ cross section is reported in Tab. 4.7.

The extrapolated $b\bar{b}$ cross sections from different non–prompt D meson species were compared to those obtained from dielectron[114] along with a comparison to FONLL and NNLO calculations in Fig. 4.16. The measurements from three D–mesons species and their average are compatible within uncertainties among each other and with those obtained from the other two ALICE measurements, as well as with the FONLL and NNLO predictions. As compared to FONLL calculations, the inclusion of NNLO corrections leads to a slightly larger central value, more in agreement with the experimental result based on non–prompt D mesons, and to reduced theoretical uncertainties.

In Fig.4.17, this measurement in pp collisions at $\sqrt{s} = 5.02$TeV is pre-

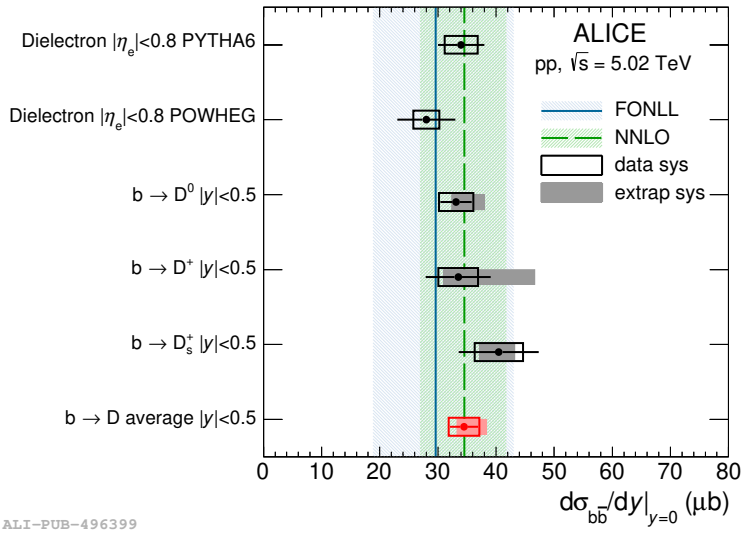

Figure 4.16: Estimates of $d\sigma_{b\bar{b}}/dy$ at midrapidity from dielectron[114] and non–prompt D^0, D^+, D_s^+ mesons, and their average, measured in pp collisions at $\sqrt{s} = 5.02$ TeV compared to FONLL[41]–[43] and NNLO[115] predictions.

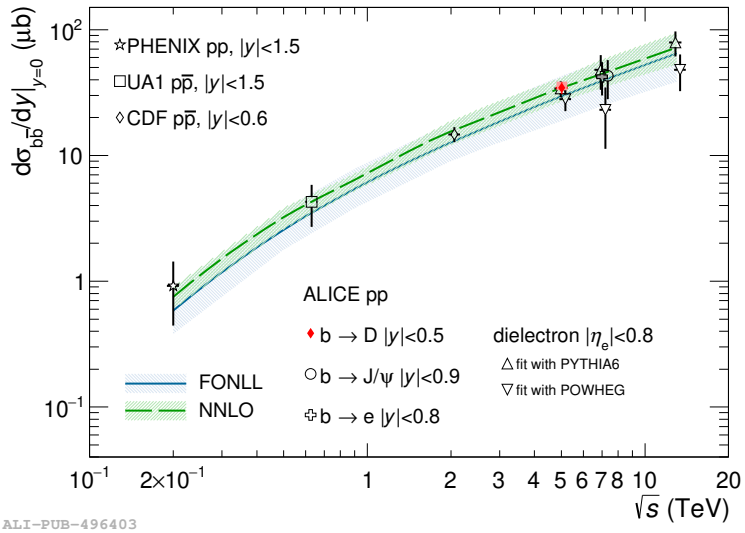

Figure 4.17: Beauty production cross section at midrapidity as a function of $\sqrt{s}$ in pp collisions measured by the ALICE[37], [116]–[118] and PHENIX[119] Collaborations and in $p\bar{p}$ collisions by the CDF[120] and UA1[121] Collaborations. The measurements are compared with the FONLL[41]–[43] (blue solid) and NNLO[115] (green dashed) calculations with their uncertainties.

sented with other measurements in pp collisions by the ALICE[37], [116]–[118] and PHENIX[119] Collaborations at same or different centre–of–mass energies. The measurement in $\mathrm{p\overline{p}}$ collisions by the CDF[120] and UAI[121] Collaborations are also presented in the same figure. The experimental results are found to be compatible with FONLL and NNLO calculations, with higher precision.

4.8.3 Summary

In this chapter, the measurement of the p_{T}–differential cross section of non–prompt D^0 mesons production is presented with other non–prompt D meson species and prompt D meson measurements, in pp collisions at = 5.02 TeV, at mid–rapidity ($|\mathrm{y}| < 0.5$). The measurement is performed using a machine–learning technique based on boosted decision trees. A data–driven method improved from minimization of χ^2 approach is employed for the fraction evaluation for non–prompt D mesons. The measurement of non–prompt D^0 is performed in p_{T} interval $1 < p_{\mathrm{T}} < 24$, where the central predictions of FONLL is in good agreement with the measured result, using the FONLL beauty–hadron cross section and the PYTHIA 8 decayer for $\mathrm{H_b} \rightarrow \mathrm{D} + \mathrm{X}$. The GM–VFNS calculations underestimate the measured cross sections, where the modeling of $\mathrm{b} \rightarrow \mathrm{D} + \mathrm{X}$ transition with a single step underestimates by a factor ranging between 2 and 10 depending on p_{T}. And the two–step modeling factorized with $\mathrm{b} \rightarrow \mathrm{H_b}$ in addition to $\mathrm{H_b} \rightarrow \mathrm{D} + \mathrm{X}$ kinematic gives larger cross sections, which confirms the importance of proper modeling in the fragmentation and the decay kinematics.

The $\mathrm{b\bar{b}}$ production cross section at midrapidity is estimated from the differential cross section within the measured p_{T} range, averaged from non–prompt D^0, D^+, and $\mathrm{D_s}^+$ mesons. The estimation is calculated using the predictions based on FONLL calculations for the beauty–hadron cross section and the PYTHIA 8 decayer for the $\mathrm{H_b} \rightarrow \mathrm{D} + \mathrm{X}$ decay kinematics. The measured total cross section is $\mathrm{d}\sigma_{\mathrm{b\bar{b}}}/\mathrm{dy}|_{|\mathrm{y}|<0.5} = 34.5 \pm 2.4(\mathrm{stat.})^{+4.7}_{-2.9}(\mathrm{tot.syst.})\mu\mathrm{b}$, which is compatible with previous ALICE measurements based on dielections, and

predictions from FONLL and NNLO calculations. This measurement provide important tests for pQCD calculations in heavy flavour sectors, and improved the precision of such measurements to provide reference in heavy–ion collisions studies.

Chapter 5

Non-prompt D^0 production in Pb-Pb collisions

In this chapter, a measurement of non-prompt D^0 production in Pb–Pb collisions by ALICE was presented. The method to reconstruct D^0 candidates is similar to the same analysis for pp collisions. With reference from the measured production cross section in pp collisions, the nuclear modification factor in Pb–Pb collision is measured, in two different centrality classes (0–10% and 30–50%). The measured results are presented and compared to prediction with different models.

5.1 Data–sets and event selections

For this work, Pb–Pb collision data collected by the ALICE experiment during LHC run2 in 2018 was analyzed. The collision events were selected by a minimum–bias trigger (kINT7) and two specific centrality triggers (kCentral and kSemiCentral) provided by V0 and ZDC detectors. The two scintillator arrays of V0 covers the full azimuth and pseudo–rapidity ranges $-3.7 < \eta < -1.7$ (V0C) and $2.8 < \eta < 5.1$ (V0A), provides information about event selection and centrality. For normalization, the number of events are summed to ∼100 M for central collisions (0-10%) and ∼85 M for semi–central collisions.

5.2 D^0 selections

The D^0 candidate selection strategy for Pb–Pb is similar to the one used in previous chapter for pp data. A pre–selection with loose criteria on decay topological variables is applied to reject rare non–physical candidates. Then dedicated BDT–based selections are applied with models trained with pseudo data from Monte-Carlo simulations and candidates from invariant mass sidebands. Lastly conservative PID selections is applied.

5.2.1 BDT selections

The variables of BDT inputs used to distinguish between signal and background candidates are based on the decay topological variables of the candidates. These selection criteria tend to enhance the reconstructed non–prompt D^0 fraction, while the combinatorial backgrounds were suppressed as well. The topological variables are same as it mentioned in 4.4, to form input arrays for BDT. The selection are based on the BDT outputs, where the cuts on BDT outputs are listed in the Tab. 5.1.

The 2 types of BDT are applied to reconstructed candidates simultaneously. As introduced in last chapter, the cumulative possibility for signal–like candidates increase as higher BDT output cut was applied. A balanced cut are choosed for each p_{T} bin in order to extract raw yield with high non–prompt fraction and the fit significance at same time. The detailed cut are listed below:

5.2.2 Particle identification

The application combining both the TPC and TOF detectors provides additional background rejection especially for low–p_{T} region. The technique Particle Identification (PID) is applied for basic particle tracks such as $\pi^{\pm}$, $K^{\pm}$, p, by comparing the deposited energy in the TPC and flight–time in the TOF to the expectations. In this analysis, the conservative 3σ cuts are applied.

Centrality Class (%)	0–10		30–50	
p_{T} bin (GeV/c)	BDT1 cut	BDT2 cut	BDT1 cut	BDT2 cut
$1.0 - 2.0$	0.06	0.15	0.06	0.15
$2.0 - 3.0$	0.09	0.12	0.08	0.16
$3.0 - 4.0$	0.10	0.15	0.09	0.20
$4.0 - 5.0$	0.08	0.17	0.07	0.19
$5.0 - 6.0$	0.07	0.18	0.07	0.18
$6.0 - 7.0$	0.06	0.22	0.07	0.19
$7.0 - 8.0$	0.05	0.20	0.05	0.15
$8.0 - 10.0$	0.06	0.19	0.05	0.16
$10.0 - 12.0$	0.04	0.17	0.03	0.13
$12.0 - 16.0$	0.03	0.16	0.03	0.12
$16.0 - 24.0$	0.03	0.15	0.01	0.07
$24.0 - 36.0$	0.03	0.04	0.00	0.02

Table 5.1: List of the selection criteria based on BDT outputs for the non–prompt D^0 analysis. The number listed in the table refer to the applied selection which require the output of BDT larger than the number.

5.3 Raw yields

In Fig.5.3 and 5.4, the raw yields of D^0 and their charge conjugates were obtained from fit to the invariant mass distribution for 0–10% and 30–50% centrality. The templates of reflection for each p_{T} bin are shown in Fig.5.1 and 5.2. The fit information including S are shown for each panel, and formed in Tab.5.2 in summary. The significance of fit ranges from 7.9 to 27.4 for central and 7.7 to 21.1 for semi–central and the quality of fit meet the expectations.

5.4 Corrections

As mentioned in last chapter, the signals after selection are of the original data. Similar corrections as performed in Sec. 4.6 are introduced below.

5.4.1 Reconstruction and selection efficiency

The correction factors that cover both measurement acceptance and selection efficiency (Acc $\times$ ϵ) were evaluated with Monte Carlo simulations. The acceptance part, which corrects D^0 yield of measurement within fiducial acceptance

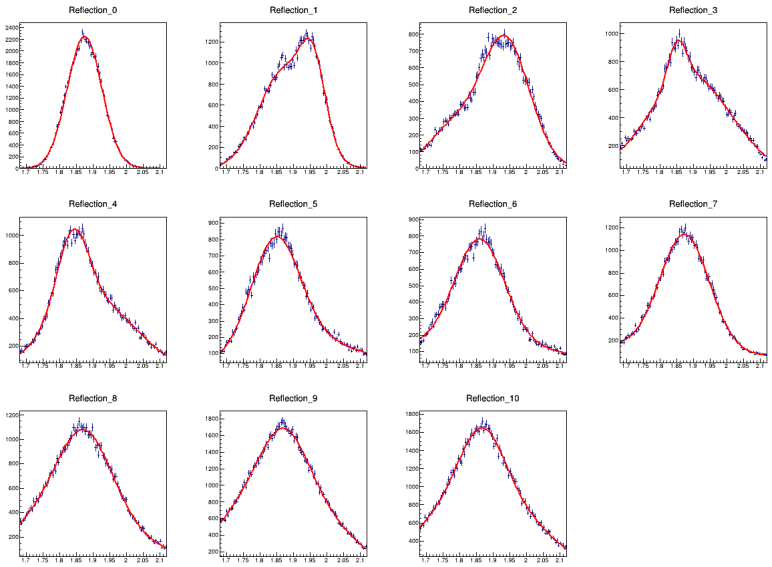

Figure 5.1: D^0 reflection distributions and the fit templates for $0-10\%$ centrality class, estimated from Monte Carlo simulations.

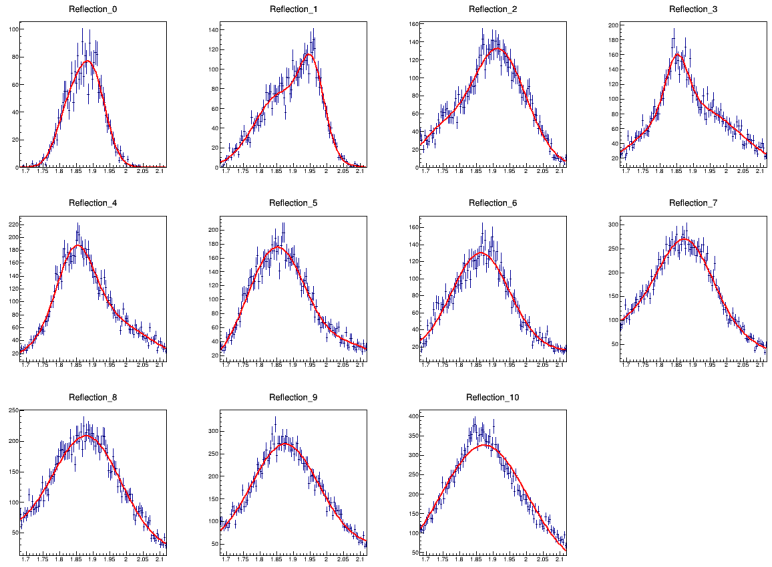

Figure 5.2: D^0 reflection distributions and the fit templates for $30-50\%$ centrality class, estimated from Monte Carlo simulations.

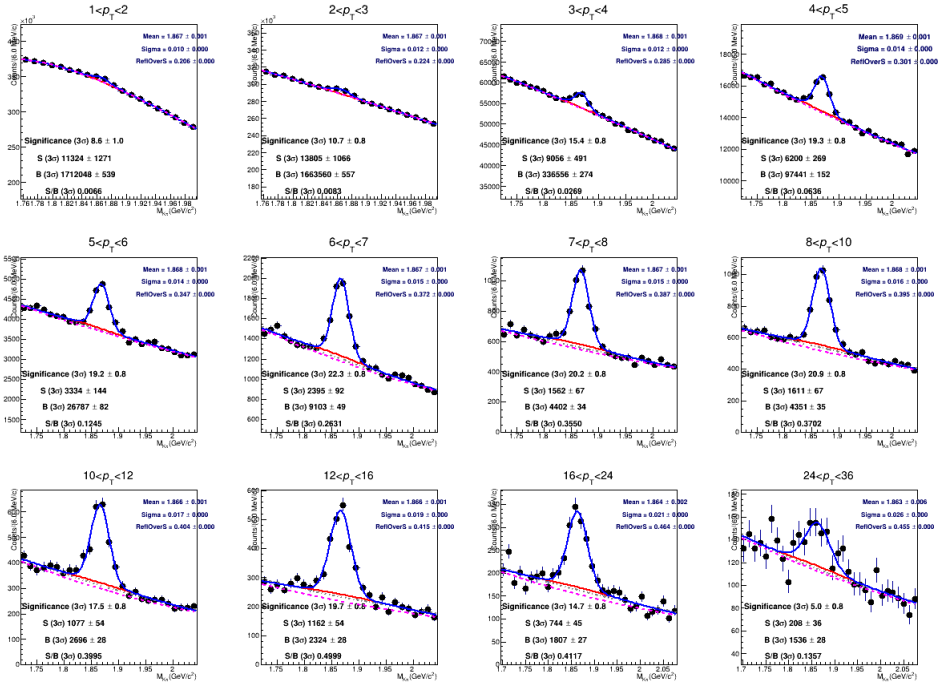

Figure 5.3: The fit to invariant mass distributions of D^0 with reflection templates included, in transverse momentum range $1 < p_T < 36$ GeV/c, for $0-10\%$ centrality class. The invariant mass distributions are divided into 12 p_T bins, where the extracted signals/backgrounds are shown explicitly in each panel.

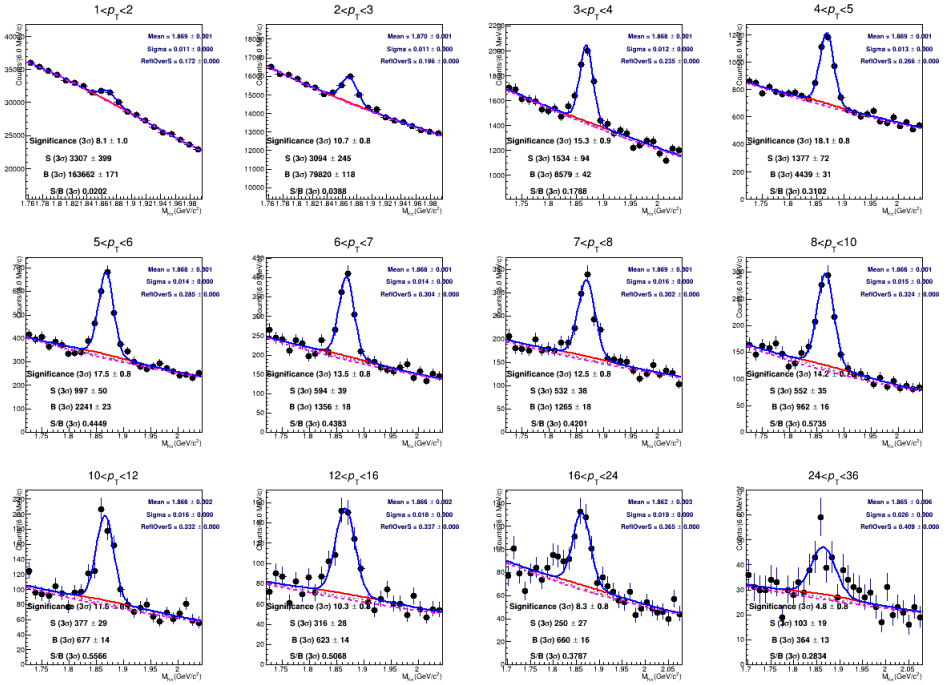

Figure 5.4: The fit to invariant mass distributions of D^0 with reflection templates included, in transverse momentum range $1 < p_T < 36$ GeV/c, for $30 - 50\%$ centrality class. The invariant mass distributions are divided into 12 p_T bins, where the extracted signals/backgrounds are shown explicitly in each panel.

Centrality Class (%)	0–10		30–50	
p_{T} bin (GeV/c)	raw yield	S/B	raw yield	S/B
$1.0 - 2.0$	11324 ± 1271	0.0066	3307 ± 399	0.0202
$2.0 - 3.0$	13805 ± 1066	0.0083	3094 ± 245	0.0388
$3.0 - 4.0$	9056 ± 491	0.0269	1534 ± 94	0.1788
$4.0 - 5.0$	6200 ± 269	0.0636	1377 ± 72	0.3102
$5.0 - 6.0$	3334 ± 144	0.1245	997 ± 50	0.4449
$6.0 - 7.0$	2395 ± 92	0.2631	594 ± 39	0.4383
$7.0 - 8.0$	1562 ± 67	0.3550	532 ± 38	0.4201
$8.0 - 10.0$	1611 ± 67	0.3702	552 ± 35	0.5735
$10.0 - 12.0$	1077 ± 54	0.3995	377 ± 29	0.5565
$12.0 - 16.0$	1162 ± 54	0.4999	316 ± 28	0.5068
$16.0 - 24.0$	744 ± 45	0.4117	250 ± 27	0.3787
$24.0 - 36.0$	208 ± 36	0.1357	103 ± 19	0.2834

Table 5.2: Extracted raw yields and the signal–to–background ratio for each p_{T} bin.

coverage to the mid–rapidity ($|y| < 0.5$) range, was determined with a toy MC generator. The selection efficiency that correct raw yield after vertexing, PID, and topological selections, was studied with dedicated simulations.

$$\mathrm{Acc} \times \epsilon \equiv \frac{\mathrm{N_{selected}}}{\mathrm{N_{produced,|y|<0.5}}} = \frac{\mathrm{N_{fiducial}}}{\mathrm{N_{produced,|y|<0.5}}} \times \frac{\mathrm{N_{raw}}}{\mathrm{N_{fiducial}}} \tag{5.1}$$

The toy MC for the acceptance part uses $\mathrm{D^0} \to \mathrm{K^-}\pi^+$ decay kinematic to determine whether the tracks are inside the fiducial acceptance or not. Meanwhile for the efficiency part, The charged–particle multiplicity and detector occupancy in the underlying events at Pb–Pb collisions are simulated with the HIJING[122] generator. The bias introduced with specific generator can be reduced by re–weighing MC events with proper p_{T} distribution, and the related uncertainties will be discussed. The simulations are also set to enrich the heavy flavour production rate instead of the reality, in order to gain enough statistics especially for high–p_{T} regions. PYTHIA8[91] generator are utilized for the such simulation for events that contains heavy quark pairs and embedded into the underlying Pb–Pb events. The transporting of generated particles through the apparatus is simulated with GEANT3[123]. Finally the overall efficiency denoted as ($\mathrm{Acc} \times \epsilon$) over transverse momentum p_{T} for prompt and non–prompt $\mathrm{D^0}$ are shown in Fig.5.5:

In Fig.5.5, the $Acc \times \epsilon$ in $0 - 10\%$ and $30 - 50\%$ centrality classes are presented as function of p_{T}. The efficiency rises from $\sim 10^{-3}$ to $\sim 10^{-1}$ with p_{T}, while $Acc \times \epsilon$ for non–prompt is ~ 100 higher than prompt. At such high ratio, the $f_{\text{non-prompt}}$ of raw yield was enhanced from $5 \sim 15\%$ to $70 \sim 90\%$, which will be explained in detail later.

5.4.2 Non–prompt fraction

As discussed in Section 3.2, the fraction of non–prompt $f_{\text{non-prompt}}$ in raw yield can be determined with $\min - \chi^2$ method with multiple sets of BDT cuts:

$$f_{\text{non-prompt}} = \frac{\mathrm{N_b} \cdot \epsilon_{\mathrm{b}}}{\mathrm{N_b} \cdot \epsilon_{\mathrm{b}} + \mathrm{N_c} \cdot \epsilon_{\mathrm{c}}} \tag{5.2}$$

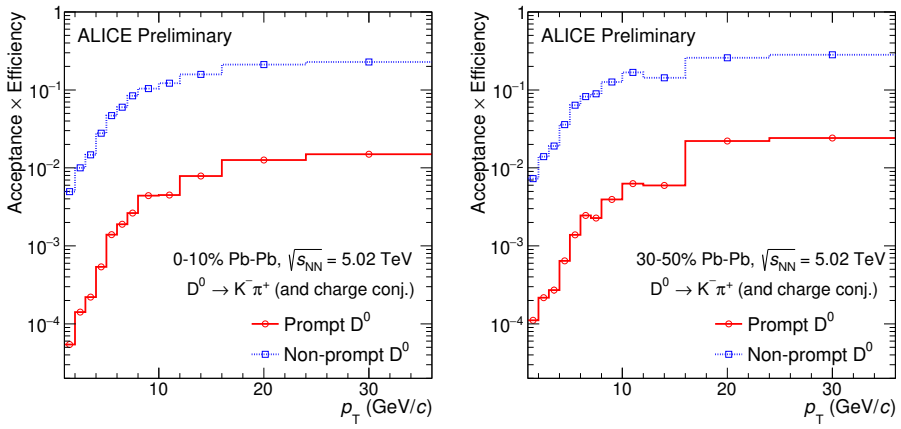

Figure 5.5: The Acc × ϵ for the non–prompt (blue) and prompt (red) D^0 mesons for $0-10\%$ (left panel) and $30-50\%$ (right panel) centrality classes respectively.

where N_b and N_c are parameter constants in Sec.3.2, and $\epsilon = N_{selected}/N$ are selection efficiencies of BDT. For instance in Fig.5.6, the parameters N_b and N_c are obtained with min–χ^2 approach, where $N_b \cdot \epsilon_{b,i}$ in blue represents the portion the non–prompt D^0 and $N_c \cdot \epsilon_{c,i}$ in red represents the prompt portion. The horizontal-axis stands for the selection cut on BDT1 response, where 0.06 means the selection cut Resp.$^{BDT1} > 0.06$, and the cuts are sorted monotonically in natural. Obviously, the portion of blue area increases with tighter selection cut, and $f_{\text{non-prompt}}$ as well.

By repeating the min–χ^2 method for each p_T bin, the non–prompt fraction $f_{\text{non-prompt}}$ are extracted, which are shown in Fig.5.7. In average, the $f_{\text{non-prompt}}$ in raw yields are $\sim 80\%$ which were enhanced significantly than ordinary fraction in previous measurements for prompt D mesons[52]. This improved the precision of non–prompt D^0 measurement.

5.5 Systematic uncertainties

The systematic uncertainties were evaluated with following sources: (i).raw yield extraction from invariant mass spectra; (ii).track reconstruction efficiency; (iii).selection efficiency; (iv).PID efficiency; (v).D^0-meson p_T shape

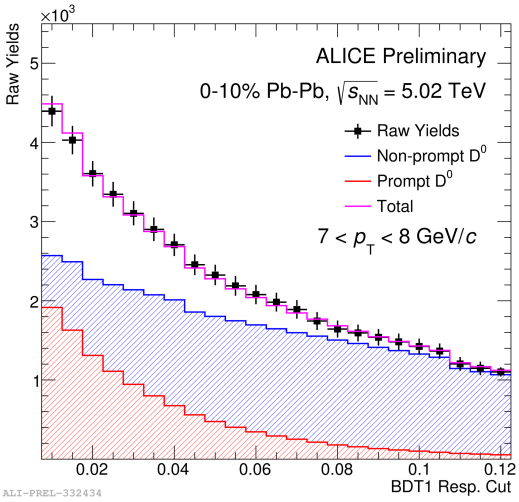

Figure 5.6: An example of applied min–χ^2 approach. The histogram in magenta is produced by minimizing the χ^2, and the corresponding non–prompt fraction is calculated by dividing the area of blue bar (non–prompt D^0) by the area below magenta histogram (inclusive) at the certain BDT output cut.

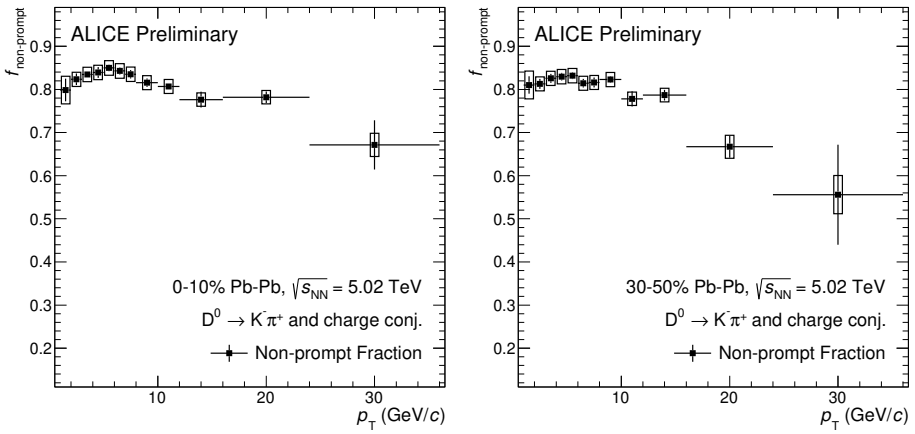

Figure 5.7: The non–prompt fraction of D^0 yield for $0-10\%$ (left) and $30-50\%$ (right), as a function of p_{T} based on minimizing χ^2 approach.

of MC simulations; (vi).determination of non–prompt fraction.

As discussed in the previous chapter, the systematic uncertainties for non–prompt D^0 measurement were evaluated considering the following sources:

- raw yield extraction from invariant mass distribution
- reconstruction efficiency of the decay tracks
- D^0 selection efficiency
- generated p_T shape of MC simulations
- determination of non–prompt fraction.

5.5.1 Raw yield extraction

As the raw yield extraction of D^0-mesons comes from fitting procedure on invariant mass spectra, the detail setting may introduce potential uncertainties to the measurement. The uncertainties are studied by repeating the mass–fitting with certain variations to the settings such as fit functions or fit parameters. The 'reflections' mentioned in 4.6.1 are subtracted from the extracted yield.

The repeating procedure of invariant mass fit was processed by a 'multi–trial' script, which works by applying a small variation to one single fit setting at a time. The variation includes: (i). upper and lower limits of the mass range. (ii). background functions. (iii). fit parameter σ. Apart from these variations, the condition of convergence are required that $\chi^2/ndf < 2$ which rejects diverse fits from systematic uncertainty evaluation. Additionally, a bin–counting method are also applied in comparison to the invariant mass fit, which utilize the original spectra histogram instead of fit function. The detailed variants of setting includes:

· 5 steps of mass fit range upper and lower limit

· background function profile, polynomial 2nd ordered, 3rd ordered

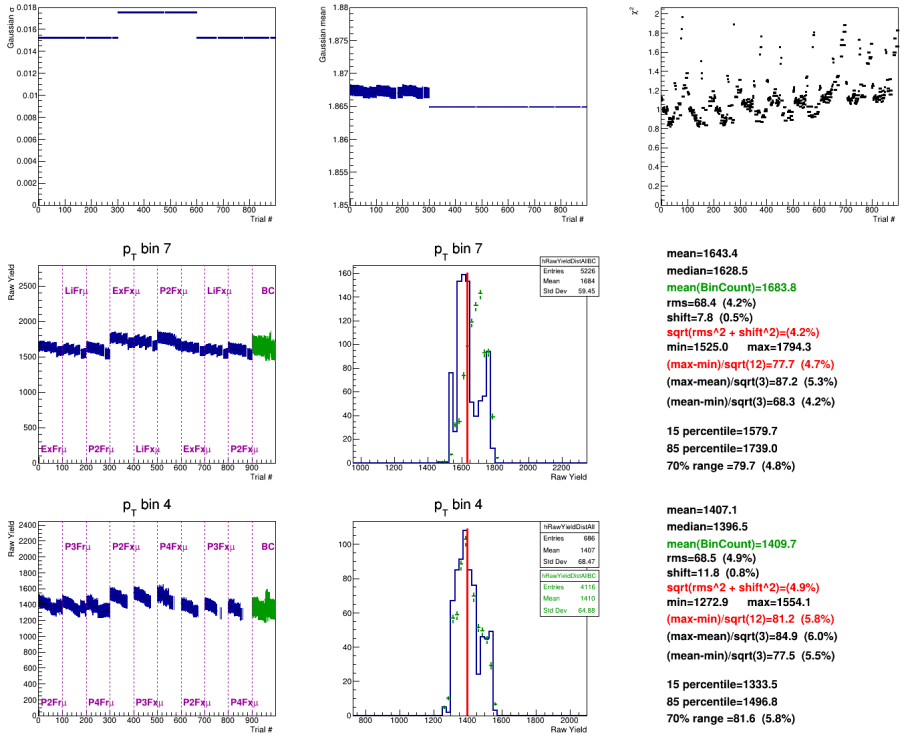

Figure 5.8: Evaluation on systematic uncertainties due to the extraction of raw yield, based on the multiple trial approach. Examples for $7 < p_{\mathrm{T}} < 8$ GeV/c at $0-10\%$ centrality class and $4 < p_{\mathrm{T}} < 5$ GeV/c at $30-50\%$ are presented.

· fixed fit parameter σ (+15%) and μ

· re–binning the original mass histogram (1–4 rebin)

· bin–counting width (3–6 σ)

An example of multi–trial check is shown in Fig. 5.8, where the uncertainties are assigned considering the following statistical parameters:

- convergence of the fit parameters such as mean and σ
- comparison between fit and bin–counting method
- r.m.s. of the raw yield distribution
- maximum - minimum divided by $\sqrt{12}$

5.5.2 Selection efficiency

Another source of systematic uncertainties originated from the signal selection procedure. The natural differences between MC and data could lead to divergence to the efficiency evaluation, and such potential bias need to be checked and covered within uncertainty ranges. Apart from BDT–based selection, the criteria are loose that potential bias is considered negligible. As for the BDT selection efficiency, the analysis of systematic uncertainty are based on variation of selection cuts.

5.5.3 p_{T} shape of the generated MC

The different p_{T} shape of generated MC sample could also be a source of systematic uncertainties. As mentioned before, the dedicated MC generator setting enriched production rate for heavy quarks, especially for high-p_{T} regions, to produce enough statistics and reduce fluctuations. As result, the generated p_{T} spectrum is significantly harder than that of data. The potential bias could be reduced by re–weighing MC with the p_{T} shape of the combination with TAMU[124] prediction and FONLL[41]–[43]. The uncertainty are evaluated with an alternative re–weighing factor that using prediction limits of TAMU. The comparison is shown in Fig. 5.13 and Fig. 5.14:

The uncertainties are assigned according to the relative difference between two re–weighings. The final uncertainties are listed in Tab. 5.3 and 5.4 for summary.

5.6 Results

With the correction to the raw yield, the measured yields is expressed as:

$$\frac{\mathrm{d}N_{\mathrm{non-prompt}}}{\mathrm{d}p_{\mathrm{T}}}|_{|y|<0.5} = \frac{1}{\Delta y \Delta p_{\mathrm{T}}} \frac{1/2}{\Gamma_{\mathrm{D}^0\to\mathrm{K}^-\pi^+}} \frac{f_{\text{non-prompt}}(p_{\mathrm{T}}) \cdot N_{raw}(p_{\mathrm{T}})}{(\mathrm{Acc}\times\epsilon)^{\text{non-prompt}}(p_{\mathrm{T}})} \frac{1}{\mathrm{N}_{\mathrm{event}}} \tag{5.3}$$

p_{T} bin (GeV/c)	1–2	2–3	3–4	4–5	5–6	6–7
Yield extr. (%)	14%	10%	5%	5%	4%	4%
Selection eff.	8%	8%	8%	5%	5%	5%
p_{T} shape	4%	4%	6%	6%	6%	3%
Tracking eff.	9%	10%	10.5%	10.5%	10%	9.5%
$f_{\text{non-prompt}}$	4%	2%				
PID eff.	0%					
Branching ratio	1%					
Total (w/o BR)	19%	17%	15%	14%	13%	12%

p_{T} bin (GeV/c)	7–8	8–10	10–12	12–16	16–24	24–36
Yield extr. (%)	4%					
Selection eff.	5%					
p_{T} shape	3%	1%				
Tracking eff.	9%	8.5%	8%	7%	6%	6%
$f_{\text{non-prompt}}$	2%					4%
PID eff.	0%					
Branching ratio	1%					
Total (w/o BR)	12%	11%	10%	10%	9.0%	10.0%

Table 5.3: summary table of systematic uncertainties non–prompt D^0 measurement in Pb–Pb collisions for 0–10% centrality at = 5.02 TeV.

p_{T} bin (GeV/c)	1–2	2–3	3–4	4–5	5–6	6–7
Yield extr. (%)	9%	6%	6%	4%	4%	4%
Selection eff.	8%	8%	8%	5%	5%	5%
p_{T} shape	8%	8%	3%	3%	2%	2%
Tracking eff.	7.5%	8%	8%	8%	8%	7%
$f_{\text{non-prompt}}$	4%	2%				
PID eff.	0%					
Branching ratio	1%					
Total (w/o BR)	17%	15%	13%	11%	11%	10%

p_{T} bin (GeV/c)	7–8	8–10	10–12	12–16	16–24	24–36
Yield extr. (%)	4%					
Selection eff.	5%					
p_{T} shape	2%	1%				
Tracking eff.	6.5%	5.5%	5%	4.5%	4%	3.5%
$f_{\text{non-prompt}}$	2%				4%	8%
PID eff.	0%					
Branching ratio	1%					
Total (w/o BR)	10%	9%	8%	8%	9.0%	11.0%

Table 5.4: summary table of systematic uncertainties non–prompt D^0 measurement in Pb–Pb collisions for 30–50% centrality at = 5.02 TeV.

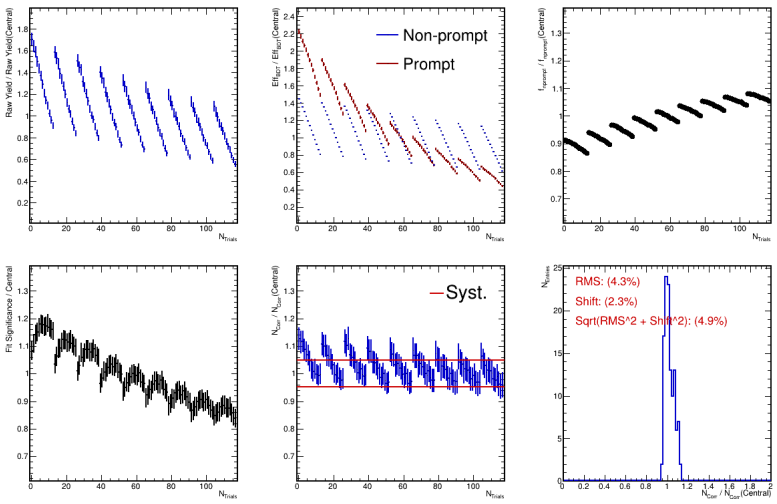

Figure 5.9: Evaluation on systematic uncertainties due to the candidate selection. The variation of selections are summarised for the evaluation, for $6 < p_{\mathrm{T}} < 7$ GeV/c in $0 - 10\%$ centrality class.

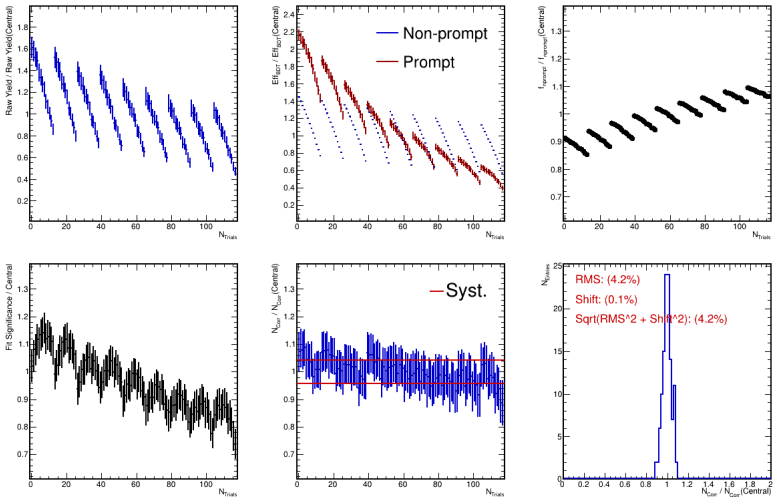

Figure 5.10: Evaluation on systematic uncertainties due to the candidate selection. The variation of selections are summarised for the evaluation, for $6 < p_{\mathrm{T}} < 7$ GeV/c in $30 - 50\%$ centrality class.

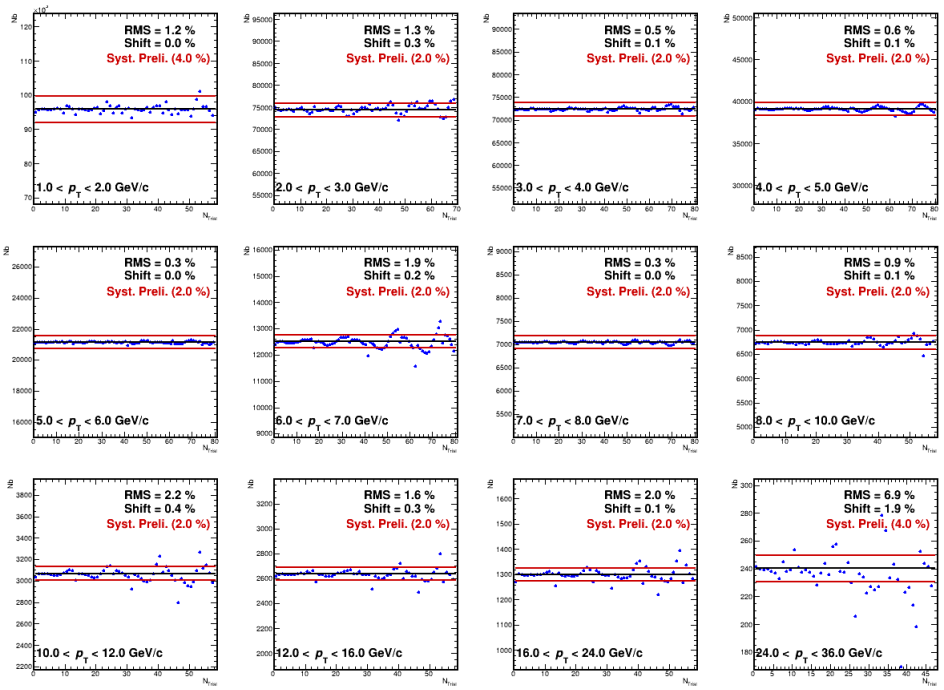

Figure 5.11: Evaluation on systematic uncertainties in minimization on χ^2 approach, where the extracted parameter N_b for variations are presented for $0-10\%$ centrality class.

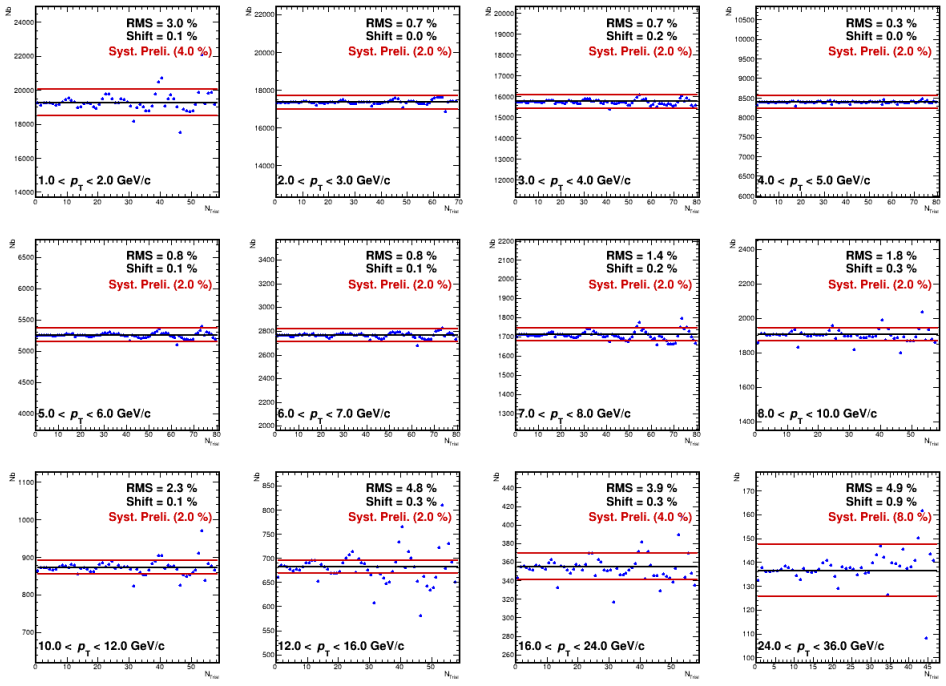

Figure 5.12: Evaluation on systematic uncertainties in minimization on χ^2 approach, where the extracted parameter N_b for variations are presented for $30-50\%$ centrality class.

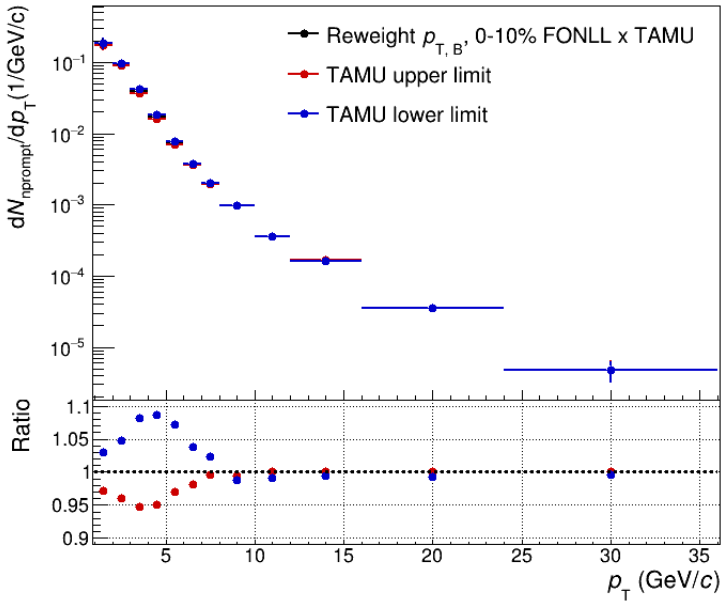

Figure 5.13: The extracted corrected yield of p_{T}–reweighing variations, for $0-10\%$ centrality, with the ratio to central value presented in the lower panel.

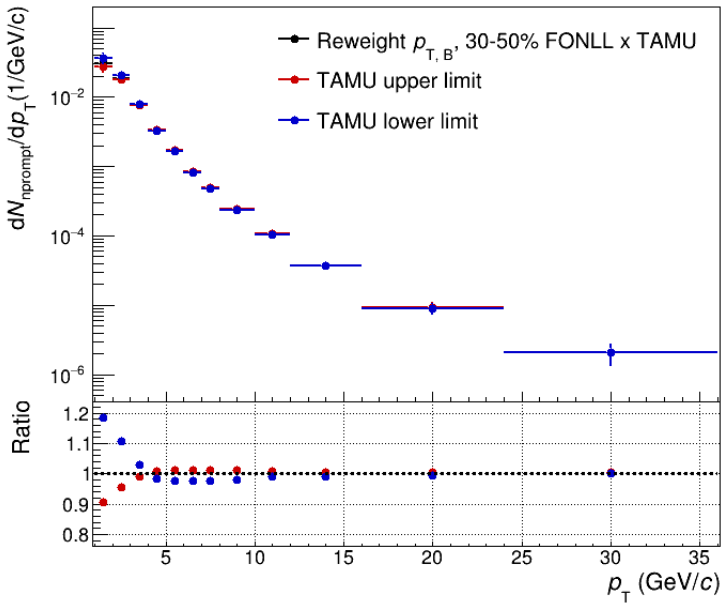

Figure 5.14: The extracted corrected yield of p_{T}–reweighing variations, for $30-50\%$ centrality, with the ratio to central value presented in the lower panel.

The raw yield sums both D^0 and $\overline{\mathrm{D}}^0$, then corrected with non–prompt fraction $f_{\text{non-prompt}}$ for only B meson decay contributions, divided by $(\text{Acc} \times \epsilon)^{\text{non-prompt}}$ the acceptance and efficiency for non–prompt D^0. The factor 1/2 comes from taking average of D^0 and $\overline{\mathrm{D}}^0$ yields. $\Gamma_{\mathrm{D}^0\to\mathrm{K}^-\pi^+}$ is the $\mathrm{D}^0 \to \mathrm{K}^-\pi^+$ branching ratio[88]. Δy is the rapidity coverage which equals to unity since the measurement was performed in $|\mathrm{y}| < 0.5$. $\mathrm{N}_{\text{event}}$ is the analyzed events number for normalization.

The measured p_{T}–differential yield for non–prompt D^0 mesons in $|\mathrm{y}| < 0.5$ in Pb–Pb collisions at $\sqrt{s_{NN}} = 5.02$ TeV is shown in upper panel of Fig. 5.16. As the measurement are mainly at center rapidity range, the yield distribution are approximately uniform versus rapidity within the fiducial detector acceptance range. The acceptance times efficiency $(\text{Acc} \times \epsilon)^{\text{non-prompt}}$ are discussed in section 5.4.1. The pp reference is also shown scaled by corresponding $\langle T_{\mathrm{AA}} \rangle$ for each centrality class in comparison to the corrected yield.

Combining with the pp as reference, the nuclear modification factor R_{AA} is shown in lower 2 panels of Fig. 5.16 for 0–10% and 30–50% centrality classes. The uncertainty on the normalization of R_{AA} results from the quadratic sum of the pp normalization uncertainty, the uncertainty on $\langle T_{\mathrm{AA}} \rangle$ and the centrality interval definition uncertainty[30]. the branching ratio uncertainty is cancelled in the ratio, while all other source are propagated uncorrelated. For $p_{\mathrm{T}} > 5$ GeV/c the R_{AA} does not change with p_{T} significantly and it shows a suppression of the yield by a factor ~ 3 for 0–10% or ~ 2 for 30–50% centrality classes to the pp reference scaled by $\langle T_{\mathrm{AA}} \rangle$. At low p_{T} around $1 < p_{\mathrm{T}} < 3$ GeV/c, the R_{AA} increases to unity with decreasing p_{T}. The measured R_{AA} is compared to with predictions from various models, namely MC@sHQ+EPOS2[58], LGR[64], [125], TAMU[124], and CUJET3.1[126]. In the TAMU model, the heavy–quark interactions with the medium are described by elastic collisions only. The LGR, MC@sHQ+EPOS2 and the CUJET models include both radiative and collisional processes. The contribution of hadronization via quark recombination, in addition to independent fragmentaion is considered in the TAMU, MC@sHQ+EPOS2 and LGR models. All

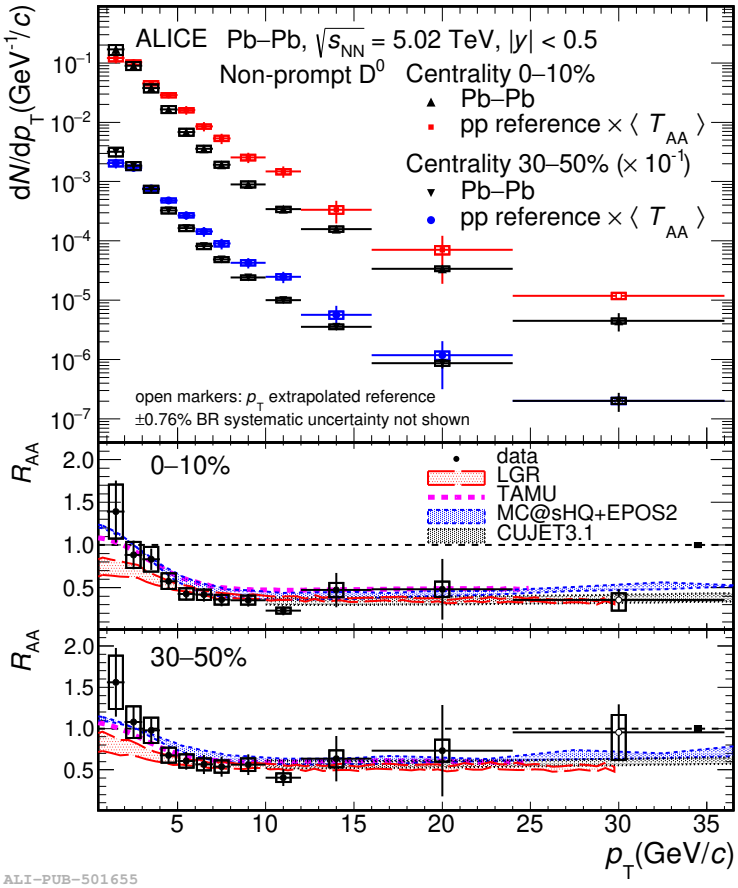

Figure 5.15: The measured corrected yield of non–prompt D^0 in Pb–Pb collisions at = 5.02 TeV for $0-10\%$ and $30-50\%$ centrality classes, together with the pp reference scaled by $\langle T_{\rm AA}\rangle$. And the corresponding nuclear modification factor $R_{\rm AA}$ are presented in the middle and lower panels, respectively. The measured $R_{\rm AA}$ are compared to the models LGR[64], [125], TAMU[124], MC@sHQ+EPOS2[58], and CUJET 3.1[126].

prediction describe the data within uncertainties in both centrality classes, except for TAMU, which tends to underestimate the suppression in the interval $5 < p_{\rm T} < 12$ GeV/c in central collisions. This comparison suggests that both radiative and collisional processes are important for beauty quark in–medium energy loss at LHC energies.

Shadowing and a modification of hadronization can also modify the $p_{\rm T}$–integrated yield of the final state beauty hadrons, which is not influenced by the energy loss, and cause $p_{\rm T}$–integrated $R_{\rm AA}$ ($p_{\rm T} > 0$) to deviate from unity. In order to test this, an extrapolation of the measured spectrum to the interval ($0 < p_{\rm T} < 1$ GeV/c), which comprise about 23% of the total yield in the 0–10% centrality class and 18% for the 30–50% centrality, was performed.

The corrected yield of $0 < p_{\rm T} < 1$GeV/c was estimated with prompt $\rm D^0$ measurement in the same $p_{\rm T}$ range. The formula of extrapolation is in Eq. 5.4:

$$\frac{{\rm d}N}{{\rm d}p_{\rm T}}|^{\rm non-prompt}_{\rm Pb-Pb,extrap.}(0 < p_{\rm T} < 1\ {\rm GeV}/c) = R^{\rm prompt}_{\rm AA,measured} \cdot \frac{R^{\rm non-prompt}_{\rm AA}}{R^{\rm prompt}_{\rm AA}}|_{\rm model} \cdot \langle T_{\rm AA} \rangle \cdot \frac{{\rm d}\sigma}{{\rm d}p_{\rm T}}|^{\rm non-prompt}_{\rm pp,extrap.} \tag{5.4}$$

where $\frac{{\rm d}\sigma}{{\rm d}p_{\rm T}}|^{\rm non-prompt}_{\rm pp,extrap.}$ is the extrapolated non–prompt cross section in pp collisions to $0 < p_{\rm T} < 1$GeV/c. The factor of extrapolating $\alpha - 1 = 0.28^{+0.01}_{-0.04}$ denotes the ratio of extrapolated part to the visible $p_{\rm T}$ region, which are discussed in Tab. 4.5. Then the r.h.s. is scaled by the $T_{\rm AA}$ for the centrality class. Finally the extrapolation is performed via multiplying the measured $R_{\rm AA}$ of prompt $\rm D^0$ by the product of two terms mentioned above times another double–ratio which consists of two $R_{\rm AA}$ predictions from model. In this work, the predicted $p_{\rm T}$ shape of the LGR model, which describes the measured double ratio $\frac{R_{\rm AA}}{R_{\rm AA}}$ for $p_{\rm T} > 1$ GeV/c within uncertainties, is exploited. The model prediction is parameterized with a 5th–order polynomial function, which is then used for fit the data in the interval $1 < p_{\rm T} < 12$ GeV/c, leaving an overall scaling factor as the only free parameter of the fit. The value of the

function at $p_{\rm T} = 0.5$ GeV/c is assumed as the estimate of the double ratio in $0 < p_{\rm T} < 1$ GeV/c. The re-scaling of the LGR prediction is performed mainly to avoid a potential unphysical discontinuity in the double ratio between the measured and extrapolated ranges. It was verified that the original value of the LGR at $p_{\rm T} = 0.5$ GeV/c gives a value of the $p_{\rm T}$–integrated yield that is compatible with that obtained with the default procedure within 1σ of the extrapolation uncertainty. The latter is obtained by summing in quadrature i). the statistical and systematic uncertainties of $R^{\rm prompt}_{\rm AA,measured}$, ii). the statistical and systematic uncertainties of $\frac{{\rm d}\sigma}{{\rm d}p_{\rm T}}$ which include the uncertainty of the extrapolation factor α, and iii). the uncertainties on the double ratio. The third term is determined by the quadratic sum of the statistical uncertainty of the scaling factor of the LGR–based parametrization and the modeling uncertainty, which is obtained from the envelope of the values by reparametrization the double ratio using the lower and upper prediction of LGR, as well as TAMU model. Moreover, the evaluated point was set at $p_{\rm T} = 0.63$ GeV/c rather than $p_{\rm T} = 0.5$ GeV/c, since the former value represents the average $p_{\rm T}$ of non–prompt $\rm D^0$ with $0 < p_{\rm T} < 1$ GeV/c according to a simulation performed by testing generated B meson decay with PYTHIA 8.243[91] to the expected $p_{\rm T}$ spectrum of FONLL. The envelope spreads around the value of the double ratio obtained with the LGR prediction covering a relative variation at $^{+19\%}_{-23\%}$ for 0–10% and $^{+62\%}_{-37\%}$ for 30–50% centrality classes, respectively. The uncertainties of the measured $p_{\rm T}$–differential pp cross section, which provides the reference for the non–prompt $R_{\rm AA}$ induce a correlation between the uncertainty of $\frac{{\rm d}\sigma}{{\rm d}p_{\rm T}}$ and the parametrization of the double ratio, which was considered negligible.

In summary, the uncertainties of the measured yield and the extrapolated part at $0 < p_{\rm T} < 1$ GeV/c obtained with the procedure described above, are considered uncorrelated in the sum performed to calculated integrated yield in $p_{\rm T} > 0$. The partial correlation induced by constraining the parametrization of the double ratio to the data is assumed negligible. As result, the uncertainties from extrapolation only contribute to $\sim 10\%$ of the total uncertainty. The

Centrality	Integrated yield
0–10%	$0.428 \pm 0.033(\text{stat.}) \pm 0.050(\text{syst.})^{+0.037}_{-0.042}(\text{extr.}) \pm 0.004(\text{BR})$
30–50%	$0.079 \pm 0.007(\text{stat.}) \pm 0.009(\text{syst.})^{+0.010}_{-0.007}(\text{extr.}) \pm 0.001(\text{BR})$
	R_{AA}
0–10%	$1.00 \pm 0.10(\text{stat.}) \pm 0.13(\text{syst.})^{+0.08}_{-0.09}(\text{extr.}) \pm 0.02(\text{norm.})$
30–50%	$1.10 \pm 0.12(\text{stat.}) \pm 0.15(\text{syst.})^{+0.14}_{-0.09}(\text{extr.}) \pm 0.03(\text{norm.})$

Table 5.5: Integrated yield and R_{AA}

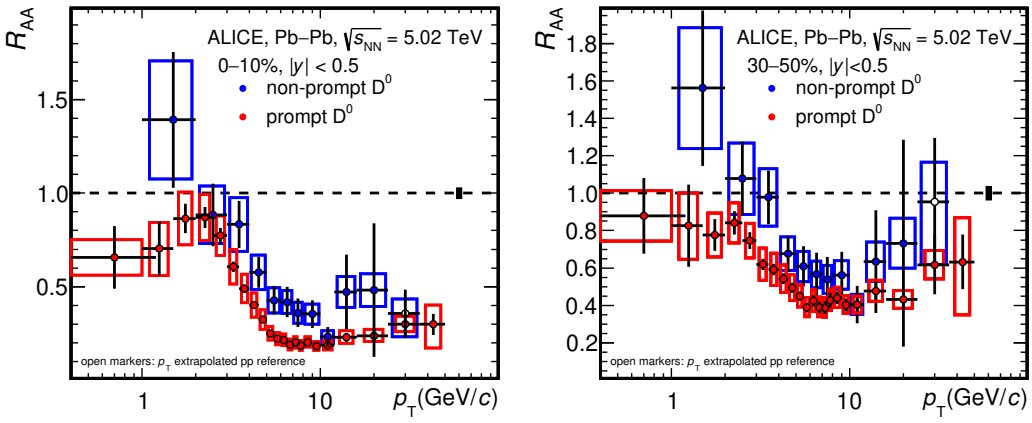

Figure 5.16: Measured nuclear modification factors R_{AA} for non–prompt and prompt D^0 as a function of p_{T}. The horizontal axis of p_{T} are draw in logarithm scale.

resulting integrated yield are listed in Tab. 5.5.

Considering the systematic and statistical uncertainties, in both centrality classes, the R_{AA} is compatible with unity within less than 1σ. Meanwhile for prompt D^0[52], the p_{T}–integrated R_{AA} is compatible with unity within 1.5σ.

In Fig. 5.16, the comparison of the non–prompt and prompt[52] R_{AA} are shown for 0–10% and 30–50% centrality classes. The R_{AA} of non–prompt D^0 in blue is systematically higher than prompt one for $p_{\text{T}} > 5\text{GeV}/c$ for both centrality classes, indicating that non–prompt D^0 are less suppressed than prompt D^0, and supporting that expectation that energy loss for beauty quarks is less than charm quarks because of their large mass. A more comprehensive re-

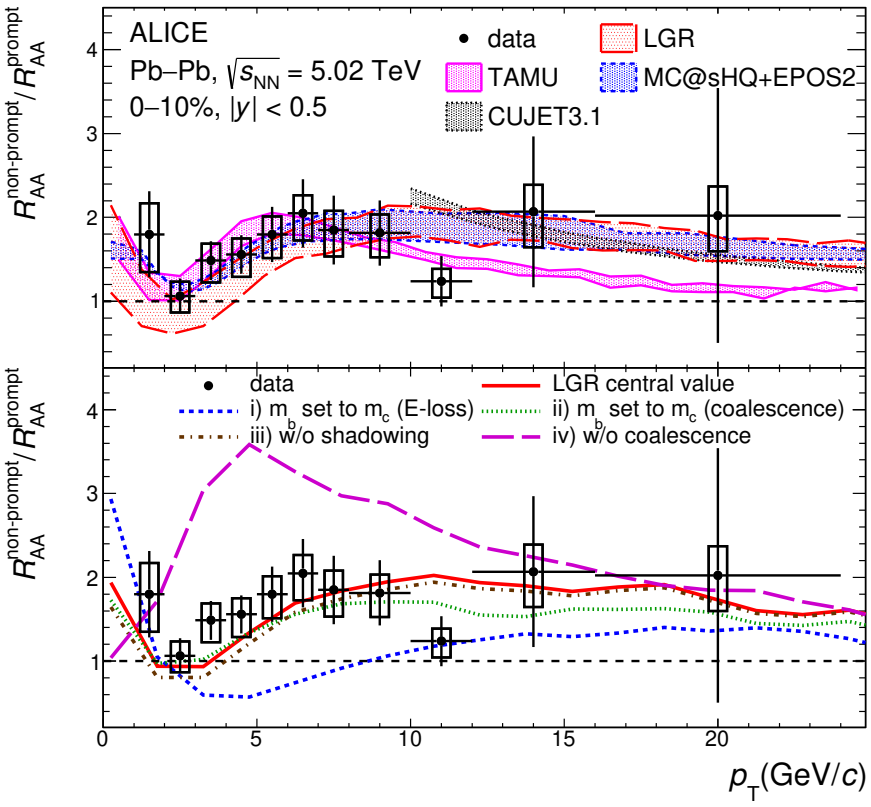

ALI-PUB-501659

Figure 5.17: Non–prompt to prompt $R_{\rm AA}$ ratio of $\rm D^0$–meson as a function of $p_{\rm T}$ in the 0–10% central Pb–Pb collisions at = 5.02 TeV, compared to model predictions[58], [64], [124]–[126] (top), and to different modifications of LGR calculations (bottom).

search was performed by yielding the double $R_{\rm AA}$ ratio $R_{\rm AA}^{\rm non-prompt}/R_{\rm AA}^{\rm prompt}$ as a function of $p_{\rm T}$, which is presented in Fig. 5.17 for the 0–10% central Pb–Pb collisions. Within the calculation, the tracking efficiency and normalization uncertainties get cancelled, while all other sources of of systematic uncertainties were propagated as uncorrelated.

As shown in the top panel of Fig. 5.17, the ratio of $R_{\rm AA}$ was compared to the predictions by the LGR[64], [125], MC@sHQ+EPOS2[58], and TAMU[124] models. At low $p_{\rm T}$, all predictions are similar, and they have a minimum close to unity in $2 < p_{\rm T} < 3{\rm GeV}/c$ and increase towards lower and higher $p_{\rm T}$. Also

they show a trend matching the data, which however cannot be assessed in a conclusive way given the uncertainties. For $p_{\rm T} > 5{\rm GeV}/c$, the measured value do not vary significantly with $p_{\rm T}$: their average is 1.70 ± 0.18 thus about 3.9σ above unity. All considered models, including CUJET3.1[126], predict a mild decrease of the ratio for $p_{\rm T} > 10{\rm GeV}/c$, which is steeper for CUJET3.1 and TAMU, with the latter predicting a maximum at $p_{\rm T} \sim 5{\rm GeV}/c$. All models describe the data within uncertainties.

In the bottom panel of Fig. 5.17, the ratio of the non–prompt to prompt $\rm D^0$–meson $R_{\rm AA}$ is compared with predictions from the default LGR calculations as well as four different modifications of the LGR models:

i). using the charm–quark mass in the calculation of the beauty–quark energy loss

ii). using the charm–quark mass in the beauty–quark coalescence

iii). excluding shadowing effects for both charm and beauty quarks

iv). excluding quark coalescence in both charm and beauty–quark hadronization

The configurations (ii) and (iii) give results similar to the default LGR calculation and can describe the data within uncertainties. The effects of shadowing are relevant mainly at low $p_{\rm T}$ and they were cancelled in the $R_{\rm AA}$ ratio[125]. The usage of the charm–quark mass in beauty coalescence reduces the $R_{\rm AA}$ ratio at high $p_{\rm T}$, as expected from the reduced coalescence probability, while it has a marginal effect for $p_{\rm T} <\sim 7{\rm GeV}/c$. By removing the quark recombination in hadronization of both charm and beauty quarks as (iv) intended, the $R_{\rm AA}$ ratio is instead significantly enhanced for $p_{\rm T} > 1$ GeV/c and reduced at lower $p_{\rm T}$. This suggests that the minimum of the $R_{\rm AA}$ ratio at $p_{\rm T} \sim 2.5$ GeV/c in the default LGR calculations is mainly due to the formation of prompt D mesons via charm–quark coalescence. In this process, D mesons acquire a momentum larger than that of the parent charm quarks,

causing a hardening of the prompt D meson p_{T} spectrum. By replacing the beauty–quark mass with that of the charm quark in the beauty–quark energy loss as (i) designed, the R_{AA} ratio reduces significantly for $p_{\mathrm{T}} > 2.5$ GeV/c and becomes lower than unity in $2 < p_{\mathrm{T}} < 8$ GeV/c, which is inconsistent with data. This supports the interpretation that the mass–dependence of quark in–medium energy–loss causes the R_{AA} ratio to the significantly larger than unity at intermediate p_{T}.

5.7 Summary

In this chapter, the non–prompt D^0 production was measured in Pb–Pb collisions for $1 < p_{\mathrm{T}} < 36$ at $\sqrt{s_{\mathrm{NN}}} = 5.02$ TeV, midrapidity, in the 0–10% and 30–50% centrality classes. The p_{T}–integrated R_{AA}, which is not directly sensitive to partonic energy loss, is compatible with unity by this measurement. A significant suppression in R_{AA} up to a factor about 3 is observed for $5 < p_{\mathrm{T}} < 8$ GeV/c in the 0–10% central Pb–Pb collisions. The measurements are compared to models that include both collisional and radiative processes in the calculation of beauty quark in–medium energy loss and quark recombination in hadronization process. The non–prompt D^0 R_{AA} is compared to that of prompt D^0, and the R_{AA} ratio of non–prompt to prompt is significantly larger than unity. The models that describe their ratio as a function of transverse momentum encode a quark–mass dependence of energy loss, both at high p_{T}, where beauty quarks lose less energy than charm quarks via radiative processes, and at low p_{T}, in which collisional processes are more relevant and the interaction of heavy quarks with the medium can be described as a diffusion process.

Chapter 6

Conclusions and Outlooks

In this thesis, the non–prompt D^0 production cross section in pp collisions has been measured at $\sqrt{s} = 5.02$ TeV using a machine–learning based model boosted decision trees. And a data–driven method utilizing the minimization of χ^2 was applied for the estimation of the non–prompt fraction for D^0 meson. The measurement was performed in the transverse momentum interval $1 < p_{\mathrm{T}} < 24$ GeV/c, and compared with predictions based on pQCD calculations. The measured cross section is in agreement with the central value of the predictions obtained with beauty–hadron cross section from FONLL calculations and the $\mathrm{H_b} \to \mathrm{D} + \mathrm{X}$ decay kinematics from the PYTHIA 8 decayer. The GM-VFNS calculations with single step transition on $\mathrm{H_b}\mathrm{D} + \mathrm{X}$ underestimate the measured cross section by a factor of about $2 \sim 8$ depending on p_{T}, while an alternative option where the fragmentation and decay kinematics of $\mathrm{b} \to \mathrm{H_b} \to \mathrm{D} + \mathrm{X}$ are factorized with two steps process, gives better agreement with data. This validates the perturbative QCD calculation to the next–leading–logarithm level, and confirms the importance of properly modelling the fragmentation process and the kinematics. The beauty fragmentation function $\frac{f_s}{f_u+f_d}_{\mathrm{beauty}}$, calculated with the p_{T}–integrated cross sections, is compatible with the previous measurements by other experiments for different centre–of–mass energies and colliding systems. The $\mathrm{b\bar{b}}$ production cross section at midrapidity was also estimated from the average of non–prompt D^0, D^+, and $\mathrm{D_s^+}$, and compatible with previous ALICE measurements based on

dielectrons, and with FONLL and NNLO calculations.

For the heavy ion collisions, a measurement on non–prompt D^0 production in Pb–Pb collisions at $\sqrt{s_{NN}} = 5.02$ TeV was performed in $0-10\%$, $30-50\%$ centrality classes, within transverse momentum interval $1 < p_T < 36$ GeV/c. The nuclear modification factor R_{AA} has been measured and found significantly suppressed to below unity by a factor of about three, for $p_T > 5$ GeV/c in $0-10\%$ centrality. The data are described by models that include both collisional and radiative processes for the in–medium energy loss calculation of beauty quarks, and quark recombination in hadronization. The R_{AA} of non–prompt D^0 is significantly higher than prompt one, where the models describe the R_{AA} ratio as a function of p_T indicate a quark–mass dependence of energy loss. At high p_T, the beauty quarks lose less energy than charm quarks via radiative processes, while at low p_T, the collisional processes are more relevant and the interaction of heavy quarks with the medium can be described as a diffusion process.

Bibliography

[1] T. van Ritbergen, J. Vermaseren, and S. Larin, "The four-loop -function in quantum chromodynamics," *Physics Letters B*, vol. 400, no. 3, pp. 379–384, 1997, ISSN: 0370-2693. DOI: https://doi.org/10.1016/S0370-2693(97)00370-5.

[2] Gross, David J. and Wilczek, Frank, "Ultraviolet behavior of non-abelian gauge theories," *Phys. Rev. Lett.*, vol. 30, pp. 1343–1346, 26 Jun. 1973. DOI: 10.1103/PhysRevLett.30.1343.

[3] Gross, David J. and Wilczek, Frank, "Asymptotically free gauge theories. i," *Phys. Rev. D*, vol. 8, pp. 3633–3652, 10 Nov. 1973. DOI: 10.1103/PhysRevD.8.3633.

[4] D. J. Gross and Wilczek, Frank, "Asymptotically free gauge theories. ii," *Phys. Rev. D*, vol. 9, pp. 980–993, 4 Feb. 1974. DOI: 10.1103/PhysRevD.9.980.

[5] H. D. Politzer, "Reliable perturbative results for strong interactions?" *Phys. Rev. Lett.*, vol. 30, pp. 1346–1349, 26 Jun. 1973. DOI: 10.1103/PhysRevLett.30.1346.

[6] H. David Politzer, "Asymptotic freedom: An approach to strong interactions," *Physics Reports*, vol. 14, no. 4, pp. 129–180, 1974, ISSN: 0370-1573. DOI: https://doi.org/10.1016/0370-1573(74)90014-3.

[7] K. Olive, "Review of particle physics," *Chinese Physics C*, vol. 38, no. 9, p. 090 001, Aug. 2014. DOI: 10.1088/1674-1137/38/9/090001.

[8] M. C. Abreu *et al.*, "Evidence for deconfinement of quarks and gluons from the J/ψ suppression pattern measured in Pb–Pb collisions at the CERN–SPS," *Physics Letters B*, vol. 477, no. 1, pp. 28–36, 2000, ISSN: 0370-2693. DOI: https://doi.org/10.1016/S0370-2693(00)00237-9.

[9] E. Andersen *et al.*, "Strangeness enhancement at mid–rapidity in Pb–Pb collisions at 158 A GeV/c," *Physics Letters B*, vol. 449, no. 3, pp. 401–406, 1999, ISSN: 0370-2693. DOI: https://doi.org/10.1016/S0370-2693(99)00140-9.

[10] I. Arsene *et al.*, "Quark–gluon plasma and color glass condensate at RHIC? the perspective from the BRAHMS experiment," *Nuclear Physics A*, vol. 757, no. 1-2, pp. 1–27, Aug. 2005. DOI: 10.1016/j.nuclphysa.2005.02.130.

[11] K. Adcox *et al.*, "Formation of dense partonic matter in relativistic nucleus–nucleus collisions at RHIC: Experimental evaluation by the PHENIX collaboration," *Nuclear Physics A*, vol. 757, no. 1-2, pp. 184–283, Aug. 2005. DOI: 10.1016/j.nuclphysa.2005.03.086.

[12] B. Back *et al.*, "The PHOBOS perspective on discoveries at RHIC," *Nuclear Physics A*, vol. 757, no. 1-2, pp. 28–101, Aug. 2005. DOI: 10.1016/j.nuclphysa.2005.03.084.

[13] J. Adams *et al.*, "Experimental and theoretical challenges in the search for the quark–gluon plasma: The STAR collaboration's critical assessment of the evidence from RHIC collisions," *Nuclear Physics A*, vol. 757, no. 1-2, pp. 102–183, Aug. 2005. DOI: 10.1016/j.nuclphysa.2005.03.085.

[14] Y. Schutz and U. A. Wiedemann, "Quark matter 2011 (QM11)," *Journal of Physics G: Nuclear and Particle Physics*, vol. 38, no. 12, p. 120 301, Dec. 2011. DOI: 10.1088/0954-3899/38/12/120301.

[15] G. Roland, K. Šafařík, and P. Steinberg, "Heavy–ion collisions at the LHC," *Progress in Particle and Nuclear Physics*, vol. 77, pp. 70–127, 2014, ISSN: 0146-6410. DOI: https://doi.org/10.1016/j.ppnp.2014.05.001.

[16] P. Braun-Munzinger, V. Koch, T. Schäfer, and J. Stachel, "Properties of hot and dense matter from relativistic heavy ion collisions," *Physics Reports*, vol. 621, pp. 76–126, Mar. 2016. DOI: 10.1016/j.physrep.2015.12.003.

[17] N. Cabibbo and G. Parisi, "Exponential hadronic spectrum and quark liberation," *Physics Letters B*, vol. 59, no. 1, pp. 67–69, 1975, ISSN: 0370-2693. DOI: https://doi.org/10.1016/0370-2693(75)90158-6.

[18] B. C. Barrois, "Superconducting quark matter," *Nuclear Physics B*, vol. 129, no. 3, pp. 390–396, 1977, ISSN: 0550-3213. DOI: https://doi.org/10.1016/0550-3213(77)90123-7.

[19] F. Karsch, "Lattice QCD at high temperature and density," 2001. arXiv: hep-lat/0106019 [hep-lat].

[20] F. Karsch and E. Laermann, "Thermodynamics and in-medium hadron properties from lattice QCD," 2003. arXiv: hep-lat/0305025 [hep-lat].

[21] E. V. Shuryak, "Quantum Chromodynamics and the theory of superdense matter," *Physics Reports*, vol. 61, no. 2, pp. 71–158, 1980, ISSN: 0370-1573. DOI: https://doi.org/10.1016/0370-1573(80)90105-2.

[22] M. L. Miller, K. Reygers, S. J. Sanders, and P. Steinberg, "Glauber modeling in high-energy nuclear collisions," *Annual Review of Nuclear and Particle Science*, vol. 57, no. 1, pp. 205–243, 2007. DOI: 10.1146/annurev.nucl.57.090506.123020.

[23] J. D. Bjorken, "Highly relativistic nucleus-nucleus collisions: The central rapidity region," *Phys. Rev. D*, vol. 27, pp. 140–151, 1 Jan. 1983. DOI: 10.1103/PhysRevD.27.140.

[24] J. Adam *et al.*, "Centrality Dependence of the Charged–Particle Multiplicity Density at Midrapidity in Pb–Pb Collisions at $\sqrt{s_{\mathrm{NN}}} = 5.02$ TeV," *Phys. Rev. Lett.*, vol. 116, p. 222 302, 22 Jun. 2016. DOI: 10.1103/PhysRevLett.116.222302.

[25] U. Heinz and R. Snellings, "Collective flow and viscosity in relativistic heavy-ion collisions," *Annual Review of Nuclear and Particle Science*, vol. 63, no. 1, pp. 123–151, 2013. DOI: 10.1146/annurev-nucl-102212-170540.

[26] S. Acharya *et al.*, "Measurements of low–p_{T} electrons from semileptonic heavy–flavour hadron decays at mid–rapidity in pp and Pb–Pb collisions at $\sqrt{s_{\mathrm{NN}}}$= 2.76 TeV," *Journal of High Energy Physics*, vol. 2018, no. 10, Oct. 2018. DOI: 10.1007/jhep10(2018)061.

[27] S. Acharya *et al.*, "Measurement of D^0, D^+, D^{*+}, and $\mathrm{D}_{\mathrm{s}}^+$ production in pb-pb collisions at $\sqrt{s_{\mathrm{NN}}}$= 5.02 TeV," *Journal of High Energy Physics*, vol. 2018, no. 10, Oct. 2018. DOI: 10.1007/jhep10(2018)174.

[28] B. Abelev *et al.*, "Production of muons from heavy flavour decays at forward rapidity in pp and Pb–Pb collisions at $\sqrt{s_{\mathrm{NN}}}$= 2.76 TeV," *Physical Review Letters*, vol. 109, no. 11, Sep. 2012. DOI: 10.1103/physrevlett.109.112301.

[29] A. M. Sirunyan *et al.*, "Nuclear modification factor of D^0 mesons in Pb–Pb collisions at $\sqrt{s_{\mathrm{NN}}}$= 5.02 TeV," *Physics Letters B*, vol. 782, pp. 474–496, Jul. 2018. DOI: 10.1016/j.physletb.2018.05.074.

[30] J. Adam *et al.*, "Transverse momentum dependence of D–meson production in Pb–Pb collisions at $\sqrt{s_{\mathrm{NN}}}$= 2.76 TeV," *Journal of High Energy Physics*, vol. 2016, no. 3, Mar. 2016. DOI: 10.1007/jhep03(2016)081.

[31] L. Adamczyk *et al.*, "Observation of D^0 meson nuclear modifications in Au+Au collisions at $\sqrt{s_{\mathrm{NN}}}$= 200 GeV," *Physical Review Letters*, vol. 113, no. 14, Sep. 2014. DOI: 10.1103/physrevlett.113.142301.

[32] V. Khachatryan *et al.*, "Suppression and azimuthal anisotropy of prompt and nonprompt J/ψ production in PbPb collisions at $\sqrt{s_{\mathrm{NN}}}$= 2.76 TeV," *The European Physical Journal C*, vol. 77, no. 4, Apr. 2017. DOI: 10.1140/epjc/s10052-017-4781-1.

[33] M. Aaboud *et al.*, "Measurement of the suppression and azimuthal anisotropy of muons from heavy–flavor decays in Pb+Pb collisions at $\sqrt{s_{\mathrm{NN}}}$= 2.76 TeV with the ATLAS detector," *Physical Review C*, vol. 98, no. 4, Oct. 2018. DOI: 10.1103/physrevc.98.044905.

[34] J. Adam *et al.*, "Inclusive, prompt and non-prompt J/ψ production at mid–rapidity in Pb–Pb collisions at $\sqrt{s_{\mathrm{NN}}}$= 2.76 TeV," *Journal of High Energy Physics*, vol. 2015, no. 7, Jul. 2015. DOI: 10.1007/jhep07(2015)051.

[35] D. Molnár and S. A. Voloshin, "Elliptic flow at large transverse momenta from quark coalescence," *Phys. Rev. Lett.*, vol. 91, p. 092 301, 9 Aug. 2003. DOI: 10.1103/PhysRevLett.91.092301.

[36] D. A. Teaney, "Viscous hydrodynamics and the Quark–Gluon Plasma," pp. 207–266, Feb. 2010. DOI: 10.1142/9789814293297_0004.

[37] S. Acharya *et al.*, "Anisotropic flow of identified particles in Pb–Pb collisions at $\sqrt{s_{\mathrm{NN}}}$= 5.02 TeV," *Journal of High Energy Physics*, vol. 2018, no. 9, Sep. 2018. DOI: 10.1007/jhep09(2018)006.

[38] M. Benzke, M. V. Garzelli, B. A. Kniehl, G. Kramer, S. Moch, and G. Sigl, "Prompt neutrinos from atmospheric charm in the general-mass variable-flavor-number scheme," *Journal of High Energy Physics*, vol. 2017, no. 12, Dec. 2017. DOI: 10.1007/jhep12(2017)021.

[39] G. Kramer and H. Spiesberger, "Study of heavy meson production in p–Pb collisions at $\sqrt{s}$= 5.02 TeV in the general–mass variable–flavour–number scheme," *Nuclear Physics B*, vol. 925, pp. 415–430, 2017, ISSN: 0550-3213. DOI: https://doi.org/10.1016/j.nuclphysb.2017.10.016.

[40] P. Bolzoni and G. Kramer, "Inclusive charmed–meson production from bottom hadron decays at the LHC," *Journal of Physics G: Nuclear and Particle Physics*, vol. 41, no. 7, p. 075 006, May 2014. DOI: 10.1088/0954-3899/41/7/075006.

[41] M. Cacciari, M. Greco, and P. Nason, "The pT spectrum in heavy–flavour hadroproduction," *Journal of High Energy Physics*, vol. 1998, no. 05, p. 007, Jun. 1998. DOI: 10.1088/1126-6708/1998/05/007.

[42] M. Cacciari, S. Frixione, and P. Nason, "The pT spectrum in heavy–flavour photoproduction," *Journal of High Energy Physics*, vol. 2001, no. 03, p. 006, Mar. 2001. DOI: 10.1088/1126-6708/2001/03/006.

[43] M. Cacciari, S. Frixione, N. Houdeau, M. L. Mangano, P. Nason, and G. Ridolfi, "Theoretical predictions for charm and bottom production at the LHC," *Journal of High Energy Physics*, vol. 2012, no. 10, Oct. 2012. DOI: 10.1007/jhep10(2012)137.

[44] S. Acharya and etc., "Measurement of D–meson production at mid–rapidity in pp collisions at $\sqrt{s}$= 7 TeV," *The European Physical Journal C*, vol. 77, no. 8, Aug. 2017. DOI: 10.1140/epjc/s10052-017-5090-4.

[45] R. Baier, Y. Dokshitzer, A. Mueller, S. Peigné, and D. Schiff, "Radiative energy loss of high energy quarks and gluons in a finite–volume quark–gluon plasma," *Nuclear Physics B*, vol. 483, no. 1, pp. 291–320, 1997, ISSN: 0550-3213. DOI: https://doi.org/10.1016/S0550-3213(96)00553-6.

[46] R. Baier, Y. Dokshitzer, A. Mueller, S. Peigné, and D. Schiff, "Radiative energy loss and p_{T}–broadening of high energy partons in nuclei," *Nuclear Physics B*, vol. 484, no. 1, pp. 265–282, 1997, ISSN: 0550-3213. DOI: https://doi.org/10.1016/S0550-3213(96)00581-0.

[47] Y. Dokshitzer and D. Kharzeev, "Heavy–quark colorimetry of QCD matter," *Physics Letters B*, vol. 519, no. 3, pp. 199–206, 2001, ISSN: 0370-2693. DOI: https://doi.org/10.1016/S0370-2693(01)01130-3.

[48] S. Peigné and A. Peshier, "Collisional energy loss of a fast heavy quark in a quark–gluon plasma," *Phys. Rev. D*, vol. 77, p. 114 017, 11 Jun. 2008. DOI: 10.1103/PhysRevD.77.114017.

[49] S. Cao, G.-Y. Qin, and S. A. Bass, "Model and parameter dependence of heavy quark energy loss in a hot and dense medium," *Journal of Physics G: Nuclear and Particle Physics*, vol. 40, no. 8, p. 085 103, Jun. 2013. DOI: 10.1088/0954-3899/40/8/085103.

[50] R. Rapp and H. V. Hees, "Heavy quarks in the quark-gluon plasma," pp. 111–206, Feb. 2010. DOI: 10.1142/9789814293297_0003.

[51] M. Djordjevic, "Heavy flavor puzzle at LHC: A serendipitous interplay of jet suppression and fragmentation," *Physical Review Letters*, vol. 112, no. 4, Jan. 2014. DOI: 10.1103/physrevlett.112.042302.

[52] The ALICE Collaboration *et al.*, "Prompt D^0, D^+, and D^{*+} production in Pb–Pb collisions at $\sqrt{s_{\mathrm{NN}}}$= 5.02 TeV," *Journal of High Energy Physics*, vol. 2022, no. 1, p. 174, 2022, ISSN: 1029-8479. DOI: https://doi.org/10.1007/JHEP01(2022)174.

[53] S. Acharya *et al.*, "Production of charged pions, kaons, and (anti-)protons in Pb–Pb and inelastic pp collisions at $\sqrt{s_{\mathrm{NN}}}$= 5.02 TeV," *Physical Review C*, vol. 101, no. 4, Apr. 2020. DOI: 10.1103/physrevc.101.044907.

[54] S. Acharya *et al.*, "Transverse momentum spectra and nuclear modification factors of charged particles in pp, p–Pb and Pb–Pb collisions at the LHC," *Journal of High Energy Physics*, vol. 2018, no. 11, Nov. 2018. DOI: 10.1007/jhep11(2018)013.

[55] S. Acharya *et al.*, "Centrality and transverse momentum dependence of inclusive J/ψ production at midrapidity in Pb–Pb collisions at $\sqrt{s_{\mathrm{NN}}}$= 5.02 TeV," *Physics Letters B*, vol. 805, p. 135 434, Jun. 2020. DOI: 10.1016/j.physletb.2020.135434.

[56] A. M. Sirunyan *et al.*, "Measurement of prompt and nonprompt charmonium suppression in PbPb collisions at 5.02 TeV," *The European Physical Journal C*, vol. 78, no. 6, Jun. 2018. DOI: 10.1140/epjc/s10052-018-5950-6.

[57] S. Acharya *et al.*, "Transverse-momentum and event–shape dependence of D–meson flow harmonics in Pb–Pb collisions at $\sqrt{s_{\mathrm{NN}}}$= 5.02 TeV," *Physics Letters B*, vol. 813, p. 136 054, Feb. 2021. DOI: 10.1016/j.physletb.2020.136054.

[58] M. Nahrgang, J. Aichelin, P. B. Gossiaux, and K. Werner, "Influence of hadronic bound states above tc on heavy-quark observables in pb+pb collisions at at the cern large hadron collider," *Physical Review C*, vol. 89, no. 1, Jan. 2014. DOI: 10.1103/physrevc.89.014905.

[59] R. Katz, C. A. G. Prado, J. Noronha-Hostler, J. Noronha, and A. A. P. Suaide, "Sensitivity study with a D and B mesons modular simulation code of heavy flavor R_{AA} and azimuthal anisotropies based on beam energy, initial conditions, hadronization, and suppression mechanisms," *Physical Review C*, vol. 102, no. 2, Aug. 2020. DOI: 10.1103/physrevc.102.024906.

[60] A. Beraudo, A. D. Pace, M. Monteno, M. Nardi, and F. Prino, "Heavy flavors in heavy–ion collisions: Quenching, flow and correlations," *The European Physical Journal C*, vol. 75, no. 3, Mar. 2015. DOI: 10.1140/epjc/s10052-015-3336-6.

[61] A. Beraudo, A. D. Pace, M. Monteno, M. Nardi, and F. Prino, "Development of heavy–flavour flow–harmonics in high–energy nuclear collisions," *Journal of High Energy Physics*, vol. 2018, no. 2, Feb. 2018. DOI: 10.1007/jhep02(2018)043.

[62] S. Cao, T. Luo, G.-Y. Qin, and X.-N. Wang, "Linearized boltzmann transport model for jet propagation in the quark–gluon plasma: Heavy quark evolution," *Physical Review C*, vol. 94, no. 1, Jul. 2016. DOI: 10.1103/physrevc.94.014909.

[63] S. Cao, T. Luo, G.-Y. Qin, and X.-N. Wang, "Heavy and light flavor jet quenching at RHIC and LHC energies," *Physics Letters B*, vol. 777, pp. 255–259, Feb. 2018. DOI: 10.1016/j.physletb.2017.12.023.

[64] S. Li and J. Liao, "Data-driven extraction of heavy quark diffusion in quark-gluon plasma," *The European Physical Journal C*, vol. 80, no. 7, Jul. 2020. DOI: 10.1140/epjc/s10052-020-8243-9.

[65] F. Scardina, S. K. Das, V. Minissale, S. Plumari, and V. Greco, "Estimating the Charm Quark Diffusion Coefficient and thermalization time from D meson spectra at RHIC and LHC," *Phys. Rev. C*, vol. 96, p. 044 905, 4 Oct. 2017. DOI: 10.1103/PhysRevC.96.044905.

[66] S. Plumari, G. Coci, V. Minissale, S. K. Das, Y. Sun, and V. Greco, "Heavy–light flavor correlations of anisotropic flows at LHC energies within event–by–event transport approach," *Physics Letters B*, vol. 805, p. 135 460, Jun. 2020. DOI: 10.1016/j.physletb.2020.135460.

[67] W. Ke, Y. Xu, and S. A. Bass, "Modified boltzmann approach for modeling the splitting vertices induced by the hot QCD medium in the deep landau-pomeranchuk–migdal region," *Physical Review C*, vol. 100, no. 6, Dec. 2019. DOI: 10.1103/physrevc.100.064911.

[68] T. Song, H. Berrehrah, D. Cabrera, J. M. Torres-Rincon, L. Tolos, W. Cassing, and E. Bratkovskaya, "Tomography of the quark–gluon plasma by charm quarks," *Physical Review C*, vol. 92, no. 1, Jul. 2015. DOI: 10.1103/physrevc.92.014910.

[69] A. M. Sirunyan *et al.*, "Studies of beauty suppression via nonprompt D^0 mesons in Pb–Pb Collisions at $\sqrt{s_{NN}}$= 5.02 TeV," *Physical Review Letters*, vol. 123, no. 2, Jul. 2019. DOI: 10.1103/physrevlett.123.022001.

[70] M. Aaboud *et al.*, "Prompt and non-prompt J/ψ and ψ(2S) suppression at high transverse momentum in 5.02 TeV Pb+Pb collisions with the ATLAS experiment," *The European Physical Journal C*, vol. 78, no. 9, Sep. 2018. DOI: 10.1140/epjc/s10052-018-6219-9.

[71] A. M. Sirunyan *et al.*, "Measurement of prompt and nonprompt charmonium suppression in Pb–Pb collisions at 5.02 TeV," *The European Physical Journal C*, vol. 78, no. 6, Jun. 2018. DOI: 10.1140/epjc/s10052-018-5950-6.

[72] J. Adam *et al.*, "Centrality dependence of high–p_T D meson suppression in Pb–Pb collisions at $\sqrt{s_{NN}}$ = 2.76 TeV," *Journal of High Energy Physics*, vol. 2015, no. 11, Nov. 2015. DOI: 10.1007/jhep11(2015)205.

[73] The STAR Collaboration, "Evidence of mass ordering of charm and bottom quark energy loss in Au+Au collisions at RHIC," 2023. arXiv: 2111.14615 [nucl-ex].

[74] A. Adare *et al.*, "Single electron yields from semileptonic charm and bottom hadron decays in Au+Au collisions at $\sqrt{s_{NN}}$= 200 GeV/c," *Physical Review C*, vol. 93, no. 3, Mar. 2016. DOI: 10.1103/physrevc.93.034904.

[75] G. Aad *et al.*, "Measurement of the nuclear modification factor for muons from charm and bottom hadrons in Pb+Pb collisions at 5.02 TeV with the ATLAS detector," *Physics Letters B*, vol. 829, p. 137 077, Jun. 2022. DOI: 10.1016/j.physletb.2022.137077.

[76] J. Adam *et al.*, "Measurement of electrons from beauty–hadron decays in p–Pb collisions at $\sqrt{s_{\mathrm{NN}}}$= 5.02 TeV and Pb–Pb collisions at $\sqrt{s_{\mathrm{NN}}}$= 2.76 TeV," *Journal of High Energy Physics*, vol. 2017, no. 7, Jul. 2017. DOI: 10.1007/jhep07(2017)052.

[77] L. Evans and P. Bryant, "LHC machine," *Journal of Instrumentation*, vol. 3, no. 08, S08001, Aug. 2008. DOI: 10.1088/1748-0221/3/08/S08001.

[78] G. Aad *et al.*, "Observation of a new particle in the search for the pstandard model Higgs boson with the ATLAS detector at the LHC," *Physics Letters B*, vol. 716, no. 1, pp. 1–29, 2012, ISSN: 0370-2693. DOI: https://doi.org/10.1016/j.physletb.2012.08.020.

[79] S. Chatrchyan *et al.*, "Observation of a new boson at a mass of 125 GeV with the CMS experiment at the LHC," *Physics Letters B*, vol. 716, no. 1, pp. 30–61, 2012, ISSN: 0370-2693. DOI: https://doi.org/10.1016/j.physletb.2012.08.021.

[80] The ALICE Collaboration, "The ALICE experiment at the CERN LHC," *Journal of Instrumentation*, vol. 3, no. 08, S08002, Aug. 2008. DOI: 10.1088/1748-0221/3/08/S08002.

[81] The ALICE Collaboration, "Performance of the ALICE experiment at the CERN LHC," *International Journal of Modern Physics A*, vol. 29, no. 24, p. 1 430 044, Sep. 2014. DOI: 10.1142/s0217751x14300440.

[82] The ALICE Collaboration, "Alignment of the ALICE inner tracking system with cosmic-ray tracks," *Journal of Instrumentation*, vol. 5, no. 03, P03003–P03003, Mar. 2010. DOI: 10.1088/1748-0221/5/03/p03003.

[83] J. Alme *et al.*, "The ALICE TPC, a large 3-dimensional tracking device with fast readout for ultra-high multiplicity events," *Nuclear Instruments and Methods in Physics Research Section A: Accelerators, Spectrometers, Detectors and Associated Equipment*, vol. 622, no. 1, pp. 316–367, Oct. 2010. DOI: 10.1016/j.nima.2010.04.042.

[84] A. Akindinov *et al.*, "Performance of the ALICE Time-Of-Flight detector at the LHC," *The European Physical Journal Plus*, vol. 128, no. 44, 2013. DOI: https://doi.org/10.1140/epjp/i2013-13044-x.

[85] B. Abelev *et al.*, "Centrality determination of Pb-Pb collisions at $\sqrt{s_{\mathrm{NN}}}$ = 2.76 TeV with ALICE," *Phys. Rev. C*, vol. 88, p. 044 909, 4 Oct. 2013. DOI: 10.1103/PhysRevC.88.044909.

[86] R. FrÃhwirth, "Application of kalman filtering to track and vertex fitting," *Nuclear Instruments and Methods in Physics Research Section A: Accelerators, Spectrometers, Detectors and Associated Equipment*, vol. 262, no. 2, pp. 444–450, 1987, ISSN: 0168-9002. DOI: https://doi.org/10.1016/0168-9002(87)90887-4.

[87] A. Hoecker *et al.*, "TMVA - Toolkit for Multivariate Data Analysis," 2009. arXiv: physics/0703039 [physics.data-an].

[88] Particle Data Group *et al.*, "Review of Particle Physics," *Progress of Theoretical and Experimental Physics*, vol. 2020, no. 8, Aug. 2020, ISSN: 2050-3911. DOI: 10.1093/ptep/ptaa104.

[89] S. Acharya *et al.*, "Measurement of D^0, D^+, D^{*+} and D_s^+ production in pp collisions at $\sqrt{s} = 5.02$ TeV with ALICE," *The European Physical Journal C*, vol. 79, no. 5, May 2019. DOI: 10.1140/epjc/s10052-019-6873-6.

[90] T. Sjöstrand, S. Mrenna, and P. Skands, "PYTHIA 6.4 physics and manual," *Journal of High Energy Physics*, vol. 2006, no. 05, p. 026, May 2006. DOI: 10.1088/1126-6708/2006/05/026.

[91] T. Sjöstrand *et al.*, "An introduction to PYTHIA 8.2," *Computer Physics Communications*, vol. 191, pp. 159–177, 2015, ISSN: 0010-4655. DOI: https://doi.org/10.1016/j.cpc.2015.01.024.

[92] M. Tanabashi *et al.*, "Review of Particle Physics," *Phys. Rev. D*, vol. 98, p. 030 001, 3 Aug. 2018. DOI: 10.1103/PhysRevD.98.030001.

[93] The ALICE Collaboration, "ALICE 2017 luminosity determination for pp collisions at $\sqrt{s} = 5$ TeV," 2018. [Online]. Available: https://cds.cern.ch/record/2648933.

[94] S. Acharya *et al.*, "Measurement of D-meson production at mid-rapidity in pp collisions at $\sqrt{s} = 7$ TeV," *The European Physical Journal C*, vol. 77, no. 8, Aug. 2017. DOI: 10.1140/epjc/s10052-017-5090-4.

[95] J. Pumplin, D. R. Stump, J. Huston, H.-L. Lai, P. Nadolsky, and W.-K. Tung, "New generation of parton distributions with uncertainties from global QCD analysis," *Journal of High Energy Physics*, vol. 2002, no. 07, pp. 012–012, Jul. 2002. DOI: 10.1088/1126-6708/2002/07/012.

[96] S. Dulat, T.-J. Hou, J. Gao, M. Guzzi, J. Huston, P. Nadolsky, J. Pumplin, C. Schmidt, D. Stump, and C.-P. Yuan, "New parton distribution functions from a global analysis of quantum chromodynamics," *Physical Review D*, vol. 93, no. 3, Feb. 2016. DOI: 10.1103/physrevd.93.033006.

[97] L. Gladilin, "Fragmentation fractions of c and b quarks into charmed hadrons at LEP," *The European Physical Journal C*, vol. 75, no. 1, Jan. 2015. DOI: 10.1140/epjc/s10052-014-3250-3.

[98] The ATLAS Collaboration, G. Aad, *et al.*, "Measurement of the differential cross–section of B^+ meson production in pp collisions at $\sqrt{s}$= 7 TeV at ATLAS," *Journal of High Energy Physics*, vol. 2013, no. 10, Oct. 2013. DOI: 10.1007/jhep10(2013)042.

[99] The LHCb Collaboration, R. Aaij, *et al.*, "Measurement of the $B^{\pm}$ production cross-section in pp collisions at $\sqrt{s}$= 7 TeV," *Journal of High Energy Physics*, vol. 2012, no. 4, Apr. 2012. DOI: 10.1007/jhep04(2012)093.

[100] The CMS Collaboration, M. Sirunyan, *et al.*, "Measurement of the $B^{\pm}$ Meson Nuclear Modification Factor in Pb-Pb Collisions at $\sqrt{s_{NN}}$ = 5.02 TeV," *Physical Review Letters*, vol. 119, no. 15, Oct. 2017. DOI: 10.1103/physrevlett.119.152301.

[101] T. Kneesch, B. Kniehl, G. Kramer, and I. Schienbein, "Charmed–meson fragmentation functions with finite–mass corrections," *Nuclear Physics B*, vol. 799, no. 1-2, pp. 34–59, Aug. 2008. DOI: 10.1016/j.nuclphysb.2008.02.015.

[102] B. A. Kniehl and G. Kramer, "Charmed–hadron fragmentation functions from CERN LEP1 revisited," *Physical Review D*, vol. 74, no. 3, Aug. 2006. DOI: 10.1103/physrevd.74.037502.

[103] D. J. Lange, "The EvtGen particle decay simulation package," *Nuclear Instruments and Methods in Physics Research Section A: Accelerators, Spectrometers, Detectors and Associated Equipment*, vol. 462, no. 1, pp. 152–155, 2001, BEAUTY2000, Proceedings of the 7th Int. Conf. on B-Physics at Hadron Machines, ISSN: 0168-9002. DOI: https://doi.org/10.1016/S0168-9002(01)00089-4.

[104] T. Aaltonen *et al.*, "Measurement of Ratios of Fragmentation Fractions for Bottom Hadrons in $p\bar{p}$ Collisions at $\sqrt{s}$ = 1.96 TeV," *Physical Review D*, vol. 77, no. 7, Apr. 2008. DOI: 10.1103/physrevd.77.072003.

[105] The LHCb Collaboration, R. Aaij, *et al.*, "Measurement of b-hadron fractions in 13 TeV pp collisions," *Physical Review D*, vol. 100, no. 3, Aug. 2019. DOI: 10.1103/physrevd.100.031102.

[106] The LHCb Collaboration, R. Aaji, *et al.*, "Measurement of b hadron production fractions in 7 TeV pp collisions," *Physical Review D*, vol. 85, no. 3, Feb. 2012. DOI: 10.1103/physrevd.85.032008.

[107] The ATLAS Collaboration, G. Aad, *et al.*, "Determination of the ratio of b-quark fragmentation fractions f_s/f_d in pp collisions at $\sqrt{s} = 7$ TeV with the ATLAS detector," *Physical Review Letters*, vol. 115, no. 26, Dec. 2015. DOI: 10.1103/physrevlett.115.262001.

[108] Heavy Flavor Averaging Group, Y. Amhis, *et al.*, "Averages of b-hadron, c-hadron, and τ-lepton properties as of 2018," *The European Physical Journal C*, vol. 81, no. 3, Mar. 2021. DOI: 10.1140/epjc/s10052-020-8156-7.

[109] P. Skands, S. Carrazza, and J. Rojo, "Tuning PYTHIA 8.1: the Monash 2013 tune," *The European Physical Journal C*, vol. 74, no. 8, Aug. 2014. DOI: 10.1140/epjc/s10052-014-3024-y.

[110] P. Braun-Munzinger, J. Cleymans, H. Oeschler, and K. Redlich, "Maximum relative strangeness content in heavy-ion collisions around 30 GeV," *Nuclear Physics A*, vol. 697, no. 3-4, pp. 902–912, Jan. 2002. DOI: 10.1016/s0375-9474(01)01257-x.

[111] S. Frixione, G. Ridolfi, and P. Nason, "A positive-weight next-to-leading-order monte carlo for heavy flavour hadroproduction," *Journal of High Energy Physics*, vol. 2007, no. 09, pp. 126–126, Sep. 2007. DOI: 10.1088/1126-6708/2007/09/126.

[112] H.-L. Lai, M. Guzzi, J. Huston, Z. Li, P. M. Nadolsky, J. Pumplin, and C.-P. Yuan, "New parton distributions for collider physics," *Physical Review D*, vol. 82, no. 7, Oct. 2010. DOI: 10.1103/physrevd.82.074024.

[113] S. Dulat, T.-J. Hou, J. Gao, M. Guzzi, J. Huston, P. Nadolsky, J. Pumplin, C. Schmidt, D. Stump, and C.-P. Yuan, "New parton distribution functions from a global analysis of quantum chromodynamics," *Physical Review D*, vol. 93, no. 3, Feb. 2016. DOI: 10.1103/physrevd.93.033006.

[114] The ALICE Collaboration, S. Acharya, *et al.*, "Dielectron production in proton–proton and proton–lead collisions at $\sqrt{s_{\mathrm{NN}}} = 5.02$ TeV," *Phys. Rev. C*, vol. 102, p. 055 204, 5 Nov. 2020. DOI: 10.1103/PhysRevC.102.055204.

[115] S. Catani, S. Devoto, M. Grazzini, S. Kallweit, and J. Mazzitelli, "Bottom-quark production at hadron colliders: Fully differential predictions in NNLO QCD," *Journal of High Energy Physics*, vol. 2021, no. 3, Mar. 2021. DOI: 10.1007/jhep03(2021)029.

[116] The ALICE Collaboration, B. Abelev, *et al.*, "Measurement of prompt J/ψ and beauty hadron production cross sections at mid–rapidity in pp collisions at $\sqrt{s} = 7$ TeV," *Journal of High Energy Physics*, vol. 2012, no. 11, Nov. 2012. DOI: 10.1007/jhep11(2012)065.

[117] The ALICE Collaboration, B. Abelev, *et al.*, "Measurement of electrons from beauty hadron decays in pp collisions at $\sqrt{s} = 7$ TeV," *Physics Letters B*, vol. 721, no. 1-3, pp. 13–23, Apr. 2013. DOI: 10.1016/j.physletb.2013.01.069.

[118] The ALICE Collaboration, S. Acharya, *et al.*, "Dielectron and heavy–quark production in inelastic and high–multiplicity proton–proton collisions at $\sqrt{s} = 13$ TeV," *Physics Letters B*, vol. 788, pp. 505–518, Jan. 2019. DOI: 10.1016/j.physletb.2018.11.009.

[119] The PHENIX Collaboration, A. Adare, *et al.*, "Measurement of Bottom versus Charm as a Function of Transverse Momentum with Electron-Hadron Correlations in p+p Collisions at $\sqrt{s} = 200$ GeV," *Physical Review Letters*, vol. 103, no. 8, Aug. 2009. DOI: 10.1103/physrevlett.103.082002.

[120] The CDF Collaboration, D. Acosta, *et al.*, "Measurement of the J/ψ Meson and b–Hadron Production Cross Sections in $p\bar{p}$ Collisions at $\sqrt{s} = 1960$ GeV," *Physical Review D*, vol. 71, no. 3, Feb. 2005. DOI: 10.1103/physrevd.71.032001.

[121] C. Albajar *et al.*, "Beauty production at the CERN $p\bar{p}$ collider," *Physics Letters B*, vol. 256, no. 1, pp. 121–128, 1991, ISSN: 0370-2693. DOI: https://doi.org/10.1016/0370-2693(91)90228-I.

[122] X.-N. Wang and M. Gyulassy, "hijing: A Monte Carlo model for multiple jet production in pp, pA, and AA collisions," *Phys. Rev. D*, vol. 44, pp. 3501–3516, 11 Dec. 1991. DOI: 10.1103/PhysRevD.44.3501.

[123] R. Brun *et al.*, "GEANT: Detector Description and Simulation Tool; Oct 1994," CERN Program Library, 1993, Long Writeup W5013. DOI: 10.17181/CERN.MUHF.DMJ1.

[124] M. He, R. J. Fries, and R. Rapp, "Heavy flavor at the large hadron collider in a strong coupling approach," *Physics Letters B*, vol. 735, pp. 445–450, Jul. 2014. DOI: 10.1016/j.physletb.2014.05.050.

[125] S. Li, W. Xiong, and R. Wan, "Relativistic langevin dynamics: Charm versus beauty," *The European Physical Journal C*, vol. 80, no. 12, Dec. 2020. DOI: 10.1140/epjc/s10052-020-08708-y.

[126] S. Shi, J. Liao, and M. Gyulassy, "Global constraints from RHIC and LHC on transport properties of QCD fluids in CUJET/CIBJET framework," *Chinese Physics C*, vol. 43, no. 4, p. 044 101, Apr. 2019. DOI: 10.1088/1674-1137/43/4/044101.

Publication List

---

1. ALICE Collaboration, **Measurement of beauty production via non-prompt D0 mesons in Pb-Pb collisions at** $\sqrt{s_{\rm NN}} = 5.02$ TeV, *JHEP 12 (2022) 126*.

2. ALICE Collaboration, **Measurement of beauty and charm production in pp collisions at** $\sqrt{s} = 5.02$ TeV **via non–prompt and prompt D mesons**, *JHEP 05 (2021) 220*.

For the publications mentioned above, I contributed as core analyzer and core author.